Boscaino, Annalisa (2014) *New directions in time-resolved neutron diffraction: probing high power microwave materials synthesis in situ.* PhD thesis.

http://theses.gla.ac.uk/5699/

NEW DIRECTIONS IN TIME-RESOLVED NEUTRON DIFFRACTION. PROBING HIGH POWER MICROWAVE MATERIALS SYNTHESIS *IN SITU*

By

Annalisa Boscaino

Submitted in the fulfilment of the requirements for the Degree of Doctor of Philosophy

School of Chemistry

University of Glasgow

October 2014

Abstract

This thesis aims to describe the design, implementation and use of a novel instrumental set-up which, by providing *in situ* ultra-rapid synthesis of transition metal carbides, is capable of investigating their reaction mechanisms, thus developing new procedures to reduce energy demanding industrial processes.

Ultra-rapid synthesis of titanium carbide, TiC - the main binary system studied - has been achieved through the development of a reproducible experimental technique and an investigation into crucial reaction variables, microwave applicators and applied power. Specifically in the case of the single mode cavity, this resulted in the completion of the majority of reactions within 60 s.

TiC formation started from its elemental precursors (titanium and graphite). An attempt to produce TiC by using a domestic microwave oven successfully lead to the synthesis of the product after *ca.* 15 minutes.

A further achievement was made by exploiting the linear relationship between the expansion of graphite (increase of *c* parameter) with temperature, which allowed for *in situ* bulk temperature measurements crystallographically. This method of measurement represents a more reliable alternative to traditional techniques (*i.e.*, pyrometery or use of thermocouples).

The majority of this work was performed on the D20 beam line at the ILL neutron source facility, in Grenoble. The choice of this beam line, capable

of collecting diffractograms at high speed rate was crucial for revealing the reaction pathways of TiC MW-promoted synthesis, for the first time.

Raman spectroscopy and scanning electron microscopy techniques were used in an effort to establish the presence of any amorphous phases in the system.

The same methodology was applied in preliminary experiments to other ternary transition metal-carbon systems. In particular, tungsten (W) and tantalum (Ta) compounds were investigated, starting from both the elements and respective oxides, WO_2 and Ta_2O_5.

Acknowledgments

First of all, I would like to thank my two supervisors, Professor Duncan H. Gregory and Dr. Thomas C. Hansen for their assistance and help during my PhD. A warm thank to Alain Daramsy, D20 technician, who helped this thesis to evolve from the experimental point of view, with his expertise and patience. I also would like to thank Jennifer Kennedy and Helen Kitchen for their help. In particular, Jen thanks for all the helpful discussion and support, which I really appreciate.

Dr. Timothy D. Drysdale and Dr. A. Gavin Whittaker were very helpful and present.

A special thank to Marco, Rei and Morgan, with their joy and love they are my precious supporting team.

List of Contents

List of Acronyms

MW	Microwaves
UHF	Ultra High Frequency
SHF	Super High Frequency
EHF	Extremely High Frequency
DMO	Domestic MW Oven
E	Electric field
FP	Forward Power
RP	Reflected Power
TWT(s)	High-power Travelling WaveTube(s)
TE	Transverse Electric
TM	Transverse Magnetic
TEM	Transverse Electromagnetic
MMC	Multi Mode Cavity
SMC	Single Mode Cavity
PND	Powder Neutron Diffraction
XRD	X-Ray Diffraction
SEM	Scanning Electron Microscope
PXD	Powder X-Ray Diffraction

*Other abbreviations not shown here will be explained in the relevant chapters

List of Figures and Tables

significantly to the diffraction pattern and it does not burn at the temperature reached in the experiments.

Figure 3.7. (a) The microcontroller table moves the MW set-up vertically (*y*-axis – maximum run 30 cm), horizontally (*x*-axis – maximum run 30 cm) and on the detector plane (ω angle – 180° degrees), in order to allow the best centering position of the sample in the neutron beam, after the best coupling position MW/sample has been found; (b) Example of microcontroller table shifted on the ω plane by 45° in respect to the position in figure 3.7(a).

Figure 4.1 (a) *Gaerling* set-up, as used in GU for Ti-C system synthesis experiments. (b) Cylindrical TE10n SMC in the *Gaerling* set-up. The reaction tube is placed vertically in this cavity, from the (open) top. The choke (indicated by a black arrow) is used for temperature readings (*via* pyrometer). (c) Schematic of *Gaerling* set-up.

Table 4.1 Summary of the experimental conditions for samples 1-4.

Figure 4.2 *Sample 1*. Single phase TiC after 10 min of MW irradiation in an MMC, in air. The graphite (002) peak is also indicated (○).

Figure 4.3 *Sample 2*. Single phase TiC after 10 min of MW irradiation in Gaerling SMC reactor, in air. The graphite (002) peak is also indicated (○).

Figure 4.4 Full reaction diffraction profile for *sample 3*. The shift of the carbon peaks to lower 2θ angles (at *ca.* 50 s) is a good indicator of a rapid temperature increase. The formation of TiC (around 100 s) is revealed by new peaks appearing at *ca.* 31° and 63° 2θ. In this reaction, TiC is not formed as a pure phase, as β-Ti is always detectable and present until the end of reaction.

Figure 4.5 *Sample 3*. For clarity, the diffractograms have been normalized at 0, 10, 60, 100, and 120 s by shifting their intensity and adding a constant of, respectively, 0, 500, 1000, 1500, 2000.

Figure 4.6. Full reaction diffraction profile for *sample 4*. The formation of TiC (~ 50 s) is indicated by new peaks appearing at *ca.* 36 ° and 72 ° 2θ.

Figure 4.7 *Sample 4*. As in Fig. 4.7, for clarity, diffractograms have been normalised at 0, 10, 20, 50, and 90 s by shifting their intensity and adding a constant of, respectively, 0, 500, 1000, 1500, 2000. Reflections from α-Ti (□), C (○), β-Ti (*), and TiC (♦) are indicated.

Chapter 1

Introduction

1.1 Microwave Radiation

Microwave (MW) energy is a non-ionizing electromagnetic radiation with frequencies between 0.3 and 300 GHz, with wavelengths ranging from 1 m to 1 mm. This broad frequency region includes three bands: the ultra high frequency, UHF, (300 MHz – 3 GHz); the super high frequency, SHF, (3 – 30 GHz) and the extremely high frequency, EHF, (30 – 300 GHz) [1] (Fig 1.1).
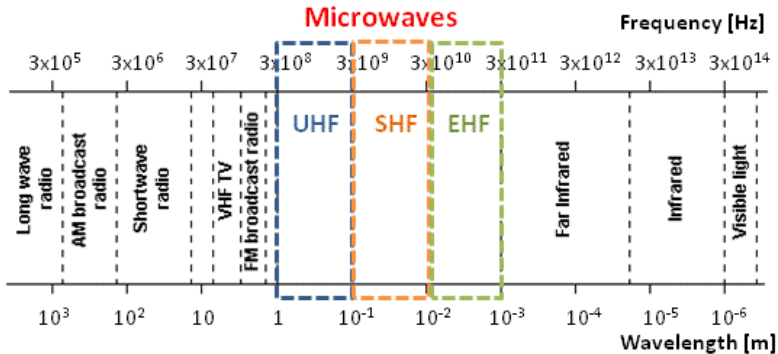
Figure 1.1. Location of the MW frequency band in the electromagnetic spectrum and band designation. It is generally between 1 – 60 GHz that MWs find their application in a variety of areas, while for the MW processing of materials the S-band (between 2 – 4 GHz) is the most exploited[1].

It has been proved that frequencies such as 6, 28, 35, and 94 GHz give very uniform electric fields, allowing efficient MW/material coupling, thus being preferred for MW processing [2, 3]. However, the US Federal

---

[1] Picture adapted from: http://www.moatel.com/board/faq.html#top

Communication Commission (FCC) allocated 915 MHz (896 MHz in the UK [4]), 2.45, 5.85, and 20.2-21.2 GHz for Industrial, Scientific, Medical and Instrumentation applications (ISMI) [5-7], making other frequencies unsuitable.

Moreover, despite the development in 2003 of a compact-size 5.8 GHz magnetron by Kuwahara *et al.* [8], this frequency is not popular because of high costs of devices [5], thus leading to 915 MHz and 2.45 GHz as the two most used frequencies at laboratory scale [1, 9, 10].

1.2 History of Microwave Processing.

The history of MW processing starts in 1921, when Albert Hull developed the first magnetron. At that time, he was studying diodes and the motion of electrons in uniform electric and magnetic fields. He devoted particular attention to understanding the special case of a system combining a uniform and static magnetic field with a radial (i.e. perpendicular to magnetic field lines) electric field [11]. Electrons moving in such a system and the associated MW production are in fact the working principle of a magnetron. Independently, other researchers worked to develop similar devices. However, these first prototypes had relatively low efficiency and, although this generated academic interest, they did not gain commercial success [12]. It was only later, in 1940, that John Randall and Henry Boot, at the University of Birmingham, succeeded in developing a more powerful - and exploitable – magnetron, called a resonant-cavity

magnetron, in which an evacuated multi-cavity was designed, capable of generating MWs by exploiting the complex phenomenon of electron behavior within a strong magnetic field (Fig 1.2). This device consists of a heated cathode, a voltage biased anode, a magnetic field and an antenna: electrons are emitted from the cathode and move along a spiral path, induced by a magnetic field, to the anode. As the electrons spiral outward, they form space charge groups, and the anode shape forms the equivalent of a series of high-Q resonant inductive-capacitive circuits. The MW frequency generated in the anode is picked up by the antenna and is transmitted into the MW cavity [13].
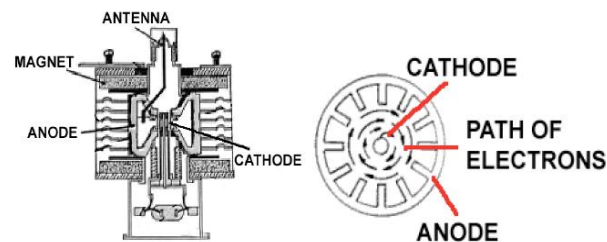
Figure 1.2 Resonant-cavity magnetron. In vacuum tubes, the anode is at a higher potential than the cathode: this leads to a strong electric field and the cathode is heated to remove the valence electrons. Once removed, electrons are accelerated toward the anode by the electric field. An external magnet is used to generate a magnetic field orthogonal to the electric one and the magnetic field creates a circumferential force in the electron as it is accelerated to the anode. This force causes the electron to travel in a spiral direction, creating a swirling cloud of electrons. As electrons pass the resonant cavities, the cavities set up oscillations in the electron cloud, and the frequency of the oscillation depends on the size of the cavity [5].

In 1946, interest in MWs was rekindled by the engineer Dr. Otto Spencer, who was working on radars at the Raytheon Corporation. He was the first person to investigate the possibility of cooking food with MWs. After experimenting, he realized that MWs would cook food faster than

conventional ovens. *Radarange* was then the first commercial MW oven, built in 1954 by Raytheon: it was large, expensive, and had a power of 1600 watts. The first more affordable domestic MW oven was produced only thirteen years later, in 1967 by Amana, a division of Raytheon, with a working frequency of 2.45 GHz. At the end of the 60s, MW ovens started to be supplied by Tappan [14] and were well-distributed worldwide. At present, the annual sale of home MW ovens in the USA, for example, is $1.5 to $2.0 billion [1, 15].

Today, the use of MWs is common in several fields, for example: communication and information; manufacturing; diagnostics and analysis; medical treatment and weapons [16, 17].

The possibility of ceramic processing via MW heating was first discussed in 1954 by Von Hippel in "*Dielectric Materials and Applications*" [18], followed by experimental studies in the 60s by Tinga *et al*. [19], Levinson [20], and Bennett *et al* [21].

However, it is only when choke systems (which prevent MW leakage)[2] were developed in 1962, that MWs started to be widely employed in both research and industry [9].

---

[2] In DMO, the choke is an integral part of the door structure, going around the full extent of the edge of the door. The entrance to the choke is covered by a piece of plastic, called the 'choke cover', which prevents steam or food particles entering the choke and changing its characteristics. The choke system works because energy entering through the choke cover will travel the length of the choke and then is reflected back by the end surface. This reflected energy would be half a wavelength (180 degrees) out of phase with the incoming energy. This means that power cancellation will occur. In the same way, in a single mode system, a choke is a plate (usually metallic) which will reflect back a radiation not absorbed by the load, thus avoiding MW leakage.

In the early '70s, mainly due to the fact that many laboratories began to be equipped with domestic MW ovens (DMSO) [9], due to their affordable prices, MW-assisted organic reactions started to be performed [22]. Reagents could be dissolved in a polar solvent with good MW absorbing properties, thus providing a means for the necessary heat for the reaction. The application of MWs in organic synthesis received a further impetus following the publications of Gedye *et al*. and Giguere *et al.* [23, 24], in 1986, in which it was reported how the use of MWs increased the speed of organic reactions by several orders of magnitude and, further, that carrying out organic reactions in the presence of a MW field would not significantly alter the product composition but only the temperature at which the reaction occurred - i.e., at higher temperature than conventional methods. In the specific case of comparison of esterification of benzoic acid with different polar solvents under MW and classical condition (i.e., reflux), in fact, MW irradiation reduced the reaction time by between 1.3 and 96 times and temperatures were increased up to 69 °C in the case of methanol (Fig 1.3) [25] - see also Gedye *et al.*[26]. More generally, Baghurst and Mingos established that organic solvents in a MW cavity superheat by 13-26 °C above their conventional boiling points at room pressure [27].

Today the application of MWs in organic synthesis has become a very large and active field of research. Just to cite few examples, MW irradiation can successfully promote the ring-closure in azetidinones

(which are important building blocks in the construction of antibiotics) without using solvents [28] or the reactions of primary and secondary amines with aldehydes and ketones can accelerate in presence of a MW field, leading to a high yield synthesis [29]. Progresses have been reported in many reviews [30-33].

Alcohol	Approximate reaction temperature (°C)	Reaction time	Average^b yield (%)	$\left[\dfrac{k_{microwave}}{k_{classical}}\right]$
Methanol	65	8 h (reflux)	74	
	134	5 min (M-wave)	76	96
1-Propanol	97	4 h (reflux)	78	
	135	6 min (M-wave)	79	40
1-Butanol	117	1 h (reflux)	82	
	135	7.5 min (M-wave)	79	8
1-Pentanol	137	10 min (reflux)	83	
	137	7.5 min (M-wave)	79	1.3
1-Pentanol at 630 watts	162	1.5 min (M-wave)	77	6.1

Figure 1.3 A table which shows good MW absorbers solvents (as from ref. [25]): MW irradiation can drastically reduce reaction times in organic reactions, by superheating the solvents up to 18 – 69 °C. All these reactions were performed at 560W - with the exception of the 1-pentanol case, at 630W - in a DMO [25].

MWs reappeared in ceramic processing in the mid '70s – and during the following decade - 1980 to 1990 - a steadily growing interest in researchers, from all over the world, was observed. A pivotal moment was in 1975 when while investigating MW drying of alumina castables, Sutton observed that MWs were also heating the ceramic, in addition to removing water [9]. Since then, and mainly from the 90s on [17], MWs have been employed extensively in solid state chemistry and materials science. A variety of materials such as carbides, nitrides, complex oxides (including zeolites and apatites) – and silicides - have been synthesized [34-36]. Further, heating and sintering of uranium oxide, barium titanites, ferrites, aluminas, and glass ceramics were also investigated [6, 37]. Interest was

21

fuelled further by some publications which contradicted the misconception between researchers that all metals reflect MWs, leading to large electric field gradients within a MW cavity and causing plasma discharge, thus being unsuitable for MW-assisted syntheses [38-41]. This is valid only for sintered or bulk metals at room temperature, but not for powdered metals and/or at high temperatures [41].

Several comprehensive reviews and papers give a broad picture of the status of MW processing over the last three decades: Katz in 1992 [6], Schiffman in 1995 [42], Clark and Sutton in 1996 [9], Rao in 1999 [43] and, more recently, Menendez in 2010 [44], among others. All the authors agree on the fact that the use of MWs can produce several advantages over conventional methods: enhanced diffusion, enhancement of mass transport, lower potential processing costs, improved mechanical properties of the products, higher resulting density at lower temperatures, extremely rapid processing times, high energy efficiency, ecologically friendly processes [45] - aspects described in more detail in section 1.2.

Conversely, the application of MWs in materials processing presents a number of challenges as well, which have been well summarized by Clark and Sutton [9]. These include: the inability to heat poorly MW-absorbing materials, the inefficient transfer of MW energy into the sample, the control of accelerated heating, and the high starting costs for MW equipment.

1.3 Microwave Interactions with Dielectric Materials.

In the MW S-band range and, in particular, at 2450 MHz, the dominant mechanism for dielectric heating is dipolar loss, also known as a *re-orientation loss mechanism*: when a material is subject to a varying electromagnetic field, heat is generated only if this material contains permanent dipoles. The polar molecules in fact try to follow the polarity of the MWs at a fast rate and when they are not able to follow the rapid reversals in the field, a phase lag takes place, which leads the power to be dissipated in the material and heat to be generated [4, 6].

This phenomenon makes MW-assisted processing essentially different from conventional thermal processing [46]: in the latter, energy is transferred to the material through convection, conduction and radiation of heat from the surfaces of the material inward, while MW energy is delivered directly to materials through molecular interaction with the electromagnetic field [5].

This gives many differences and advantages when using MWs for processing materials, with respect to conventional heating mechanisms:

- An inverse temperature gradient is observed [37, 41]. In conventional processing, the sample is heated from the surface inwards, while in MWs, the direction of heating is from inside to outside, thus resulting in higher temperature of the sample core than the surface.
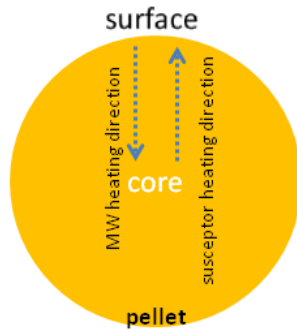
Figure 1.4 The inverse temperature profile in MW heating.

- Rapid/volumetric heating. MWs directly penetrate materials interacting with particulates within the sample, rather than being conducted into the bulk from an external heat source. This provides rapid volumetric heating which enables the process of both large and small samples very rapidly and uniformly [47].

- Enhanced densification and quality of products [5, 47, 48]. The densification rate strongly depends on the diffusion of ions between sample particles, and the grain growth rate is mostly determined by the grain boundary diffusion. Dube and coworkers, have found that the intense MW field concentrates around samples during MW sintering [49]. Especially, the power of MW field between sample particles is almost 30 times larger than the external field, giving rise to ionization at the surface of sample particles. As a result, the diffusion of ions between sample particles is accelerated and the densification stage is promoted [50]. Moreover, surrounding electromagnetic field can intensely couple with ions at grain boundaries. Under drive of MW field, the kinetic energy of

24

ions at grain boundaries increases, which results in decreasing activation energy for a forward jump of ions and increasing the barrier height for a reverse jump. So the forward diffusion of intergrain ions is promoted and thus accelerates the grain growth during sintering.

- Selective heating of materials and new materials production [51, 52].

- MWs selectively couple in different ways with materials showing different dielectric properties; therefore, in multiple phase materials, some phases may couple more readily with MWs, leading to new or unique microstructures.

- High control of chemical reactions [52]. Reactions can be "switched on and off" by simply switching on and off the power supply.

- Economically viable and ecology friendly [51]. The deposition of energy directly in the bulk of the material eliminates wasting energy due to the simultaneous heating of furnaces and reactor walls. With MWs, it is the sample itself that heats up and in turn acts as the source of heat, thus lowering the effective thermal mass and reducing the required power input. Hence, MW methods can drastically reduce the energy consumption which is experienced in high temperature processes, where heat losses increase with increasing process temperature, thus permitting energy-efficient reactions [41].

The dielectric properties of a sample – together with its shape and size - are the main features determining the way in which a material will be heated with MWs. They are expressed in terms of the dielectric constant (ε') – which is the measure of the response to the applied external electric field (E) and in particular, it is the measure of the polarizability of a material in an E and it determines whether or not a material will heated by MWs [53]- and the dielectric loss factor (ε'') - which quantifies the ability of the material to convert the absorbed MW power into heat [5].These two components are expressed in terms of the complex dielectric permittivity (ε*):

$$\varepsilon^* = \varepsilon' - i\varepsilon'' (= \varepsilon^0(\varepsilon_{r'} - i\varepsilon_{eff''})) \qquad \text{Eq.1.1}$$

(where ε^0 is the permittivity in free space, $\varepsilon_{r'}$ the relative dielectric constant, $\varepsilon_{eff''}$ the effective relative dielectric loss factor, and $i = (-1)^{1/2}$.)

The dielectric response is also expressed in terms of the energy dissipation factor, or loss tangent, *tan δ*, which is a measure of the absorption of MWs by the material:

$$\tan \delta = \varepsilon'' \big/ \varepsilon' \qquad \text{Eq.1.2}$$

A tanδ around 0.01 indicates a low absorption material, a tanδ of 0.1 a medium absorption material, while a tanδ around 1 indicates a high absorber of MWs.

The knowledge of the complex dielectric constant is relevant for specification of optimal MW heating strategies and optimal set-up design:

it determines the best working frequency, the shape of the applicator (where the interaction material/MWs occurs, also referred to as cavity or reactor), and the best position of the sample in the applicator. However, it is a complex function of temperature, moisture content, density and electric field direction, which make its determination not an easy task – as is also demonstrated by the presence of over thirty methods for measuring it [53].

The problem of processing materials which are poor absorbents of MWs can be overcome by the so-called "hybrid heating". This process is commonly performed to sinter a material with low dielectric loss at low temperature and high dielectric loss at high temperature. MWs are absorbed by the component that shows the highest dielectric loss in the mixture and passed through the low-loss material with little drop in energy [41, 54]. This can be performed by using a material, called susceptor, with high loss at low temperature, which will absorb MWs and reaches fast high temperatures. Then, the susceptor will transfer heat to the sample via conventional heating mechanism and the sample with high dielectric loss at high temperature will be now able to absorb MWs alone (Figure 1.4). In this thesis, an example of hybrid heating is presented in Chapter 4, given by a mixture of titanium (Ti) – "low-lossy" material, with $\tan\delta$ below 0.01 – and carbon graphite (C) – good MW absorber, $\tan\delta$ of *ca.* 0.35-0.83 [44]. Ti has been successfully heated up by means of MW in the presence of C, thus allowing fast formation of TiC.

1.3.1 The Microwave Effect

The term "microwave effect" refers to the drastic increase of speed observed in reactions promoted by MWs, and it is usually quantified by the difference between the temperatures of the two treatments leading to the same microstructure:

$$\Delta T = T_{conv} - T_{MW} \qquad\qquad \text{Eq. 1.3}$$

where T_{conv} stands for conventional heating and T_{MW} for heating by means of MWs.

Examples of the enhanced speed of reactions promoted by MWs include, among many others [52], sintering of ceramics [55-57], MW-driven radioactive tracer ion diffusion [3], MW-driven ion-exchange reactions in glasses [58], MW joining of ceramics [59], MW decomposition of solid solutions [57], synthesis of metal-carbide powders [60], promotion of organic imidazation reactions [61].

The "microwave effect" is still a controversial issue and over the years different theories have been proposed to solve it: lowered activation energies [3], enhanced diffusion caused by increased vibrational frequency of ions due to the electric field component of the MW radiation [62], excitation of a non-thermal phonon distribution in the polycrystalline lattice, quasi-static polarization of the lattice near point defects, and the ponderomotive action of the high-frequency electric field on charged vacancies in the ionic crystal lattice [47, 48, 52].

The first complication in revealing this – sometimes huge - difference in reaction behaviour can be addressed mainly to temperature measurements experienced in MW processing. When the temperature is obtained by means of a thermocouple, for example, only the zone close to the tip of the thermocouple is considered (which means no bulk temperature measurement). Further, the thermocouple needs to be shielded because it can interact with the MW field, giving systematic errors. Another method of temperature measurement makes use of optical pyrometry; however, where the surface:volume ratio is small, optical methods do not give a reliable measure of internal temperature [47], but only surface temperature [37, 48], which in the case of MW heating is the coolest part of the sample (while in conventional heating is the hottest), thus making the measurement problematic and affected by error [48].

Over time, these difficulties have misled the knowledge of the real ΔT. In 1990, Janney *et al.* reported a $\Delta T = 300\text{-}400°C$ in the processing of oxides, in both 2.45 and 28 GHz MW furnaces [3]. Today, a more precise determination of the temperature can be obtained. For example, Link and co-workers applied Raman spectroscopy as a means of temperature measurement of single phases in a multi-phase material [63], from which values of ΔT well below those reported in the literature earlier ones - typically: $\leq 50°C$ instead of $> 200°C$ – were obtained.[3]

In the light of these findings, it is crucial to understand if these differences between MW-induced and traditional sintering processes are a "simple" consequence of the ΔT (i.e., given by a pure thermal effect) or other phenomena have to be considered.

At present, two views regarding the increased reaction rates predominate [64]:

a) Increased reaction rates are given by differences in temperature between the two heating methods (MW and conventional), therefore they are governed by *thermal effects*;

b) MWs enhance reaction speed because of *non-thermal effects*.

Many MW-induced reactions in liquid phases exhibiting enhanced reaction rates have been exhaustively explained by means of localized superheating effects [27, 47, 65], also known as "hot spots"[65]; in such cases, reaction rates are determined by thermal effects.

For solid state case, in 1994, Rybakov and Symenov [66], and independently other authors after them [48, 52, 67], proposed a possible mechanism of the non-thermal influence of the high frequency (HF)

---

[3] As described in more details in Chapter 2, section 2.3.4, Raman spectroscopy relies on inelastic scattering of monochromatic light. In case that part of the photon energy is transmitted to the material this is called Stokes scattering. The resulting photon of lower energy generates a Stokes line on the red side of the incident light. On the other hand if energy from the tested material is transmitted to the photon this is called Anti-Stokes scattering. As a consequence, these shifts in photon energy contain information about the energy states in the system - comparable to information resulting from infrared spectroscopy. Thus Raman spectra reveal information about the phase composition of the material. Furthermore, since in general the shift of observed spectral lines is temperature dependent, this information can be used to get phase specific temperature information out of a measured Raman spectrum [63].

electromagnetic field (typically, 2.45GHz). They considered that the effect of MWs is not to increase transport coefficient – which would have lead to a *multiplicative* increase in the transport flux in the presence of a pre-existing conventional driving force – but rather introduce an *additional* driving force, which should manifested as an additive increase in the transport flux. They also found that when considering lattice defects, the vacancy mobility was not affected. An enhancement in densification when using MWs was consistent with a dependence on the electric field experienced by the material. This suggested that the MW field was inducing an additional (electric) driving force.

Whittaker experimentally investigated the effect of the *direction* of the electric field upon the rate of ion transport – rather than on the strength of the electric field – by studying the change in the mass transport as a function of the angle to the MW electric field. He found that MWs may directly influence ion transport in a high temperature sintering process. An effect of this intense field is to concentrate the lattice defects and enhance ion mobility at the interface. This mechanism may therefore enhance the rate of mass transport at *a given temperature* when a MW field is present [47].

1.4 MW-Induced Synthesis of Ceramics: Binary and Ternary Carbides.

Microwave technology has been increasingly used for producing ceramic materials in recent years. One of the most important reasons is the potential of reduction in the manufacturing cost due to short synthesis time and energy-efficiency [15, 68]. Standish *et al.* concluded – based on rational assumptions for capital and operating costs – that a MW reduction process could save 15% to 50% over a conventional operation [69].

1.4.1 Titanium Carbide

Titanium carbide (TiC) is an important nonoxide ceramic material used for mechanical, chemical and electronic applications, as it possesses a number of desirable properties, such as high melting temperature (3260 °C), high hardness (Knoop's hardness = 32.4 GPa), high electrical conductivity (3×10^6 S/cm) [70-72], high thermal conductivity (16.7 W mK^{-1}), high chemical stability, high wear resistance and high solvency for other carbides [73] (and ref therein). Therefore, it can be used in cutting tools, grinding wheels, wear resistant coatings, high-temperature heat exchangers, magnetic recording heads, turbine seals, etc [74]. It is widely used as a substitute for tungsten carbide (WC), a common machining material, thus reducing manufacturing costs. In fact, currently 10% of the world's consumed cobalt is employed as a binder material for WC

composites, while equivalent TiC materials use nickel as a binder, which costs only half as much [75].

TiC and titanium carbonitride are also utilized in production of Al_2O_3-TiC and ZrO_2-Ti(C,N) composites [74]. In addition, a promising field of application comprises plasma and flame spraying processes in air atmosphere, where again TiC-based powders show higher phase stability than WC-based powders [76].

There are a number of different methods for synthesizing TiC, such as the reaction of liquid magnesium and vaporized $TiCl_4+C_xCl_4(x=1, 2)$ solution [77], combined sol-gel and microwave carbothermal reduction methods [78], gas phase reaction of $TiCl_4$ with gaseous hydrocarbons [77] and, synthesis by thermal plasma techniques [79]. TiC is traditionally produced, however, by carbothermal reduction of titanium dioxide (TiO_2) in a temperature range between 1700 - 2100 °C for 10 – 20 h [73, 79].

TiO_2 has generally been used as a raw material because of its low costs and ease of handling. Further, TiO_2 is abundantly available in nature. It can be derived in fact from ilmenite ($FeTiO_3$) which represents the main matrix of sand found on beaches. Ilmenite contains TiO_2 in the range of 40-60% along with iron oxide – depending on the source [80]. Globally, nearly all TiO_2 is produced from ilmenite as it naturally occurs in accessible high concentrations and in a form which allows the preparation of synthetic rutile [81].

However, in the production of TiC via the conventional carbothermal reduction of TiO_2/carbon, high temperatures and long reaction times – and consequently high synthesis costs – are required. Moreover, there are significant challenges to forming oxygen-free TiC [60, 78, 79].

A number of attempts have been made to produce TiC in a more energy efficient way and the first successful effort in the synthesis of TiC via carbothermal reduction assisted by MWs (MICROwave Controlled COMbustion Synthesis, MICROCOM) was made by Ahmad and coworkers in 1991. They ignite the starting powders, Ti and C graphite, in a high power industrial multimode microwave oven (Raytheon 6.4kW maximum, 2.45GHz) at 2.4kW and collected the product, TiC, after several minutes [82].

In 1995, Hassine and co-workers attempted the synthesis of TiC and tantalum carbide (TaC), starting from the oxides (TiO_2 and Ta_2O_5, respectively), via carbothermal reduction induced by MW power. Despite both oxide precursors being relatively poor absorbers of MWs (with low loss tangent, *tan δ*), the TiO_2/C and Ta_2O_5/C mixtures showed good coupling abilities to MW energy, thanks to the high dielectric loss of the carbon black reactant. However, while they succeeded in the formation of TaC – which formed a pure phase without evidence of any intermediate phases during the reaction - they encountered problems in synthesizing TiC. The reaction exclusively yielded a titanium oxycarbide phase, $Ti(O_{0.2}C_{0.8})$. They ascribed this to the experimental conditions: a relatively

34

low reaction temperature was reached (1550 °C instead of 2000 °C) and a flux of argon was employed (which could contain oxygen as impurity) [60].

More recently, Winkler *et al.* performed an in situ observation of TiC formation via conventional heating, by using a high temperature furnace, starting from Ti (powder, average grain size < 43 μm) instead of TiO_2 as a starting material in combination with C (graphite powder, average grain size <16 μm), working in vacuum. They observed TiC formation after four 4 hours at a temperature of 1073K [83], with no formation of intermediate phases:

$$Ti + C \rightarrow TiC \ (-139\pm6 \ kJ/mol) \qquad Eq.1.4$$
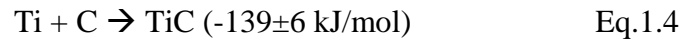
This reaction represents the first success in the production of TiC starting from Ti and C *via* conventional means at shorter times and at lower temperatures than previously observed. They employed powder neutron diffraction (PND) to follow this reaction *in situ*. This study represents a good starting point for the comparison of the MW synthesis of TiC followed by in situ PND, as performed in this thesis.

1.4.2 Other ternary compounds

Additional, TiC-based ternary chemical systems have been tested in this thesis, by using the same methodology already optimised for the preparation of TiC.

TiC-based transition metal systems are classified as *cermets*, materials composed of ceramic (*cer*) and metallic (*met*) parts, specifically designed to have the optimal properties of both elements, namely high temperature resistance and hardness of ceramic and the ability to undergo plastic deformation, typical of metals. It is known, in fact, that the incorporation of a second phase into a ceramic matrix result in improvement in the mechanical properties of the composite material; *e.g.,* when TiC particles (grain size of 1–1.5 μm) are added to Al_2O_3, the carbide limits the Al_2O_3 grain growth in the matrix during sintering and gives a higher strength, higher hardness material, which is resistant to crack propagation [3]. Al_2O_3–TiC composite has been widely used in industry as cutting tools and wear resistance coating due to its high hardness, chemical stability, good strength and toughness at elevated temperature, and excellent wear resistance [74].

Also metals such as Ni, Co, and Fe have been incorporated as a ductile second phase to improve monolithic TiC toughness at ambient temperatures. Liquid phase sintering, and melt infiltration are the two common production techniques used in the processing of these materials. Nickel is the most commonly used metallic binder phase in TiC based composites, which is mainly due to the low wetting angle[4], 30° under

---

[4] The wetting (or contact) angle is an angle conventionally measured through the liquid, where a liquid/vapor interface meets a solid interface. It quantifies the wettability of a solid surface by a liquid *via* the Young equation. A given system of solid, liquid and vapor at a given temperature and pressure has a unique wetting angle. However, contact angle hysteresis is observed, ranging from the maximal and minimal angle. The equilibrium contact is within these values: it reflects the relative strength of the liquid, solid and vapor molecular interaction.

vacuum (10^{-5} torr) at 1450° C [84], that liquid Ni forms with solid TiC. Addition of molybdenum to nickel reduces the wetting angle with TiC to zero [84], and this leads to TiC-based composites with very good mechanical properties. In the 1950s considerable effort had been devoted to the development of TiC-based composites for high temperature critical applications such as turbine blades. The major binder metallic alloys being investigated were: Ni-Mo, Ni-Mo-Al, Ni-Cr, and Ni-Co-Cr. These systems, however, were not able to meet the high temperature requirements, such as high strength, oxidation resistance and ductility, and TiC-based composites found use in less critical applications such as cutting tools and metal working tools [75]. In the 1980s, ordered intermetallic compounds, especially nickel aluminides (Ni_3Al, NiAl), titanium aluminides (Ti_3Al, TiAl, $TiAl_3$), and iron aluminides (Fe_3, Al, FeAl), have been considered as potential high temperature materials. This is mainly due to the properties that these intermetallics possess, such as increase in strength with temperature, relatively low density, and good oxidation resistance. The research efforts on aluminides were successful, and in the 1990s two of these aluminides, Ni_3Al and TiAl, are commercialized as high temperature materials for critical components [85]. Recently, intermetallic aluminides have also been utilized as binder phase in the preparation of TiC-based composites [86-89]. Hot pressing and presureless melt infiltration techniques were utilized for the processing of TiC-Ni_3Al [86] and TiC-FeAl [87-89] composites with

37

promising mechanical properties comparable to that of commercially available TiC-Ni and WC-Co cermets [87-89]. Of these intermetallic composites, TiC-Ni$_3$Al composites might be used for high temperature (~1100°C) applications, and TiC-FeAl composites can be used under more severe corrosion conditions [87-89]. Intermetallic aluminides have also been used as binder phase in the processing of other carbides, oxides, and borides, such as WC-Ni$_3$Al and Al$_2$O$_3$-Ni$_3$Al [86], Al$_2$O$_3$-(Ti,Fe,Nb,Mo,Zr,Ni) aluminides of different stoichiometry [90], WC-FeAl, TiB$_2$-FeAl and ZrB$_2$-FeAl [91], Al$_2$O$_3$-NbAl$_3$ [92] and Al$_2$O$_3$-FeAl [93]. Hot pressing and pressureless infiltration techniques have been used in the processing of TiC-Ni$_3$Al and TiC-FeAl composites. An alternative processing technique for the production of TiC-based intermetallic composites is the reactive sintering technique [75].

In past few years, also Ni, Fe, Al, Cu, Mo, W – among other metals - were incorporated into reactant mixtures of Ti and C to study their effects on the formation of TiC–metal composites. Conventional synthesis routes for these compounds included self propagation high temperature synthesis (SHS) and combustion synthesis (CS) [94-99]. However, carbide preparation in these conventional routes require a huge instrumentation regarding melting the metal and graphite under vacuum at a very high temperature. Mechanical alloying of powder ingredients at room temperature can easily produce nanocrystalline metal carbides, thus

representing one of the alternative, cost-effective way of producing these compounds.

In this thesis, tantalum (Ta) and tungsten (W) - and their related oxides, Ta_2O_5 and WO_2 respectively - were mixed with Ti and graphite, in different stoichiometric ratios.

To the knowledge of the author, cermets formed by Ta-TiC system are not reported in literature, except for an extensive study of $TaTiC_2$ at high temperature (from 1500°C upwards) [100].

The synthesis of these compounds by means of MWs has been performed, for the first time, during this thesis and preliminary results are presented in Chapter 4.

1.5 Role of *in situ* Neutron Powder Diffraction in MW Processing of Carbides and Aim of the Thesis.

At present, the characterization of products obtained by means of MW heating is performed *ex situ*, but in order to reach a full understanding of the interaction of a MW field with solids and to measure and interpret bulk temperature, *in situ* analysis is essential.

Hence, although *ex situ* analysis allows the characterization of the materials which is obviously important, it provides very little information regarding the process of the reaction or why and how the reaction occurs.

The principal aim of this thesis has been the design of a single mode MW reactor capable of inducing the fast synthesis of binary and ternary

carbides and *in situ* powder neutron diffraction (PND) observation, in order to reveal the mechanism of formation of the compounds in study and the sample/MW interaction.

In situ PND has been chosen as ideal probe over electrons and X-rays methods, because transient intermediate phases − *i.e.*, in the case of TiC synthesis, Ti_2O_3, Ti_3O_5, Ti_4O_7, and $Ti(O_x, C_y)$ in different O:C ratios − were intended to be observed and neutrons discern C and O better than the other techniques. This provides more insight in probing the reaction mechanism for the formation of the expected final products.

References

1. Klein, M.V., J.A. Holy, and W.S. Williams, *Raman scattering induced by carbon vacancies in TiCx.* Physical Review B, 1978. **17**(4): p. 1546-1556.
2. Fukushima, H., *Rapid Heating by Single-Mode Cavity Controlled at 6GHz.* Novel Materials Processing (MAPEES'04), 2005.
3. Janney, M.A. and H.D. Kimrey, *Diffusion-Controlled Processes in Microwave-Fired Oxide Ceramics.* MRS Online Proceedings Library, 1990. **189**: p. 215.
4. Bradshaw, S.M., E.J. van Wyk, and J.B. de Swardt, *Microwave heating principles and the applications to the regeneration of granular activated carbon.* Journal of South African Institute of Mining and Metallurgy, 1998.
5. Thostenson, E.T. and T.-W. Chou, *Microwave processing: fundamentals and applications.* Composites: Part A, 1999. **30**: p. 1055-1071.
6. Katz, J.D., *Microwave Sintering of Ceramics.* Annual Review of Material Science, 1992. **22**: p. 153-170.
7. Ghammaz, A., S. Lefeuvre, and N. Teissandier, *Spectral behaviour of domestic microwave ovens and its effects on the ISM band.* Ann. Telecommun., 2003. **58**(7-8): p. 11.
8. Kuwahara, N. in *Third Symposium Microwave Science and Application Related Fields*. 2003. Osaka University.

9.   Clark, D.E. and W.H. Sutton, *Microwave Processing of Materials.* Annual Review of Material Science, 1996. **26**: p. 299-331.

10.   Lewis, D., et al., *Conventional and High Frequency Microwave Processing of Nanophase Ceramic Materials.* Nanostructured Materials, 1997. **9**(1-8): p. 97-100.

11.   Hull, A.W., *The Effect of a Uniform Magnetic Field on the Motion of Electrons Between Coaxial Cylinders.* Physical Review, 1921. **18**(1): p. 31-57.

12.   Wathen, R.L., *Genesis of a generator—The early history of the magnetron.* Journal of the Franklin Institute, 1953. **255**(4): p. 271-287.

13.   Helmich, R.J. *Microwave-assisted Synthesis of Inorganic Materials*. 2006; Literature seminar:[

14.   Osepchuk, J.M., *A History of Microwave Heating Applications.* IEEE Transactions on Microwave Theory and Techniques, 1984. **32**(9): p. 1200-1224.

15.   Global Industry Analysts, I., *Microwave Ovens MCP-6255. A Global Strategic Business Report*, in *Global Microwave Ovens Industry*. 2010.

16.   Clark, D.E. and D.C. Folz, *What is Microwave Processing?* 1994, National Academy Press.

17.   Agrawal, D., et al., *Microwave Processing of Ceramics, Composites and Metallic Materials*, in *Microwave Solutions for Ceramic Engineers*, D.E. Clark, et al., Editors. 2006, The American Ceramic Society: Westerville, Ohio.

18.   Von Hippel and A. R., *Dielectric Materials and Applications*, ed. M.M.I.T.P. Cambridge. 1954, Cambridge.

19.   Tinga, W.R. and W.A.G. Voss, *Microwave Power Engineering*, A. Press, Editor. 1968: New York. p. 189-194.

20.   Levinson, M.L., *Method of Firing Ceramic Articles Utilizing Microwave Energy*, in *U.S. Patent No. 3585258*. 1971.

21.   Bennett, C.E.G., N.A. McKinnon, and L.S. Williams, *Sintering in Gas Discharges.* Nature, 1968. **217**: p. 1287-1288.

22.   Liu, S.W. and J.P. Wightman, *Decomposition of simple alcohols, ethers and ketones in a microwave discharge.* Journal of Applied Chemistry and Biotechnology, 1971. **21**(6): p. 168-172.

23.   Gedye, R., et al., *The use of microwave ovens for rapid organic synthesis.* Tetrahedron Letters, 1986. **27**(3): p. 279-282.

24.   Giguere, R.J., et al., *Application of commercial microwave ovens to organic synthesis.* Tetrahedron Letters, 1986. **27**(41): p. 4945-4948.

25.   Gedye, R.N., F.E. Smith, and K.C. Westaway, *The rapid synthesis of organic compounds in microwave ovens.* Canadian Journal of Chemistry, 1988. **66**(1): p. 17-26.

26.   Gedye, R.N., W. Rank, and K.C. Westaway, *The rapid synthesis of organic compounds in microwave ovens. II.* Canadian Journal of Chemistry, 1991. **69**(4): p. 706-711.

27.   Baghurst, D.R. and D.M.P. Mingos, *Superheating Effects Associated with Microwave Dielectric Heating.* Journal of Chemical Society, Chemical Communications, 1992(9): p. 674-677.

28.   Martelli, G., G. Spunta, and M. Panunzio, *Microwave-assisted solvent-free organic reactions: Synthesis of β-lactams from 1,3-azadienes.* Tetrahedron Letters, 1998. **39**(34): p. 6257-6260.

29.   Varma, R.S., R. Dahiya, and S. Kumar, *Clay catalyzed synthesis of imines and enamines under solvent-free conditions using microwave irradiation.* Tetrahedron Letters, 1997. **38**(12): p. 2039-2042.

30.   Caddick, S., *Microwave assisted organic reactions.* Tetrahedron, 1995. **51**(38): p. 10403-10432.

31.   Lidström, P., et al., *Microwave assisted organic synthesis—a review.* Tetrahedron, 2001. **57**(45): p. 9225-9283.

32.   Kappe, C.O., *Controlled Microwave Heating in Modern Organic Synthesis.* Angewandte Chemie International Edition, 2004. **43**(46): p. 6250-6284.

33.   de la Hoz, A., et al., *Cycloadditions under Microwave Irradiation Conditions: Methods and Applications.* European Journal of Organic Chemistry, 2000. **2000**(22): p. 3659-3673.

34.   Bykov, Y.V. and V.E. Semenov, *High-temperature microwave processing of materials.* Journal of Physics D: Applied Physics, 2001. **34**: p. R55-R75.

35.   Cheng, J., et al., *Microwave reactive sintering to fully transparent aluminum oxynitride (ALON) ceramics.* Journal of Materials Science Letters, 2001. **20**: p. 77-79.

36.   Fang, Y., et al., *Enhancing densification of zirconia-containing ceramic-matrix composites by microwave processing.* Journal of Material Science, 1997. **32**: p. 4925-4930.

37.   Boch, P. and N. Lequeux, *Do microwaves increase the sinterability of ceramics?* Solid State Ionics, 1997. **101-103**: p. 1229-1233.

38.   Zhou, G.-T., et al., *Microwave-assisted solid-state synthesis and characterization of intermetallic compounds of Li3Bi and Li3Sb.* Journal of Materials Chemistry, 2003. **13**(10): p. 2607-2611.

39.   Palchik, O., et al., *Microwave-Assisted Preparation, Morphological, and Photoacoustic Studies of the Na_4SnSe_4, $K_4Sn_2Se_6$, and $K_4Sn_3Se_8$, Zintl Molecular Sn–Se Oligomers.* Journal of Solid State Chemistry, 2002. **165**(1): p. 125-130.

40.   Landry, C.C. and A.R. Barron, *Synthesis of Polycristalline Chalcopyrite Semiconductors by Microwave Irradiation.* Science, 1993. **260**: p. 1653-1655.

41. Goldstein, J., et al., *Special Topics in Scanning Electron Microscopy*, in *Scanning Electron Microscopy and X-ray Microanalysis*. 2003, Springer US. p. 195-270.

42. Schiffman, R.F., *Commercializing Microwave Systems: Paths to success or Failure.* Ceramic Transactions, 1995. **59**: p. 7-17.

43. Rao, K.J., et al., *Synthesis of Inorganic Solids Using Microwaves.* Chemical Materials, 1999. **11**: p. 882-895.

44. Menéndez, J.A., et al., *Microwave heating processes involving carbon materials.* Fuel Processing Technology, 2010. **91**: p. 1-8.

45. Michael, D., D.M.P. Mingos, and D.R. Baghurst, *Microwaves in Chemical Synthesis*, in *The New Chemistry*. 2000, Cambridge University Press.

46. Clark, D.E., I. Ahmad, and R.C. Dalton, *Microwave ignition and combustion synthesis of composites.* Journal of Materials Science and Engineering A, 1991. **144**: p. 91-97.

47. Whittaker, A.G., *Diffusion in Microwave-Heated Ceramics.* Journal of Chemical Materials, 2005. **17**: p. 3426-3432.

48. Wang, J., et al., *Evidence for the Microwave Effect During Hybrid Sintering.* Journal of the American Ceramic Society, 2006. **89**(6): p. 1977-1984.

49. Dube, D.C., et al., *Experimental evidence of redistribution of fields during processing in a high-power microwave cavity.* Applied Physics Letters, 2004. **85**(16): p. 3632-3634.

50. Nightingale, S.A., *Interfacial phenomena in microwave sintering.* Ionics, 2001. **7**: p. 327-331.

51. Agrawal, D., et al., *Microwave Energy Applied to Processing of High-Temperature Materials.* American Ceramic Society Bulletin, 2008. **87**(3): p. 39-44.

52. Bookse, J.H., et al., *Microwave ponderomotive forces in solid-state ionic plasmas.* Physics of Plasmas, 1998. **5**(5): p. 1664-1670.

53. Tinga, W.R. and E.M. Edwards, *Dielectric Measurements Using Swept Frequency Techniques.* Journal of Microwave Power and Electromagnetic Energy, 1968. **3**(3): p. 114-125.

54. Immirzi, A., *La diffrazione dei cristalli*, ed. L. Editore. 2002, Napoli.

55. Bykov, Y., A. Eremeev, and V. Holoptsev, *Experimental Study of the Non-Thermal Effect in Microwave Sintering of Piezoceramics.* MRS Online Proceedings Library, 1994. **347**.

56. Wroe, R. and A.T. Rowley, *Evidence for a non-thermal microwave effect in the sintering of partially stabilized zirconia.* Journal of Materials Science, 1996. **31**(8): p. 2019-2026.

57. Willert-Porada, M., *Microwave Effects on Spinodal Decomposition.* MRS Online Proceedings Library, 1996. **430**.

58. Fathi, Z., D.E. Clark, and R. Hutcheon, *Surface Modification of Ceramics Using Microwave Energy.* MRS Online Proceedings Library, 1992. **269**.

59. Palaith, D. and R. Silberglitt, *Microwave joining of ceramics.* American Ceramic Society Bulletin, 1989. **68**(9): p. 1601-1606.

60. Hassine, N.A., J.G.P. Binner, and T.E. Cross, *Synthesis of Refractory Metal Carbide Powders via Microwave Carbothermal Reduction.* International Journal of Refractory Metals & Hard Material, 1995. **13**: p. 353-358.

61. Lewis, D.A., et al., *Accelerated imidization reactions using microwave radiation.* Journal of Polymer Science Part A: Polymer Chemistry, 1992. **30**(8): p. 1647-1653.

62. Clark, D.E., W.R. Tinga, and J.R. Laia, *Microwaves: Theory and application in materials processings* Ceramic Transactions, ed. A.C. Society. 1993.

63. Link, G., et al., *Investigation of selective microwave heating by use of Raman spectroscopy.* Ceramic Transactions, 2010. **220**: p. 27-34.

64. Antonio, C. and R.T. Deam, *Can "microwave effects" be explained by enhanced diffusion?* Journal of Physical Chemistry Chemical Physics, 2007. **9**: p. 2976-2982.

65. Jacob, J., L.H.L. Chia, and F.Y.C. Boey, *Thermal and non-thermal interactions of microwave radiation with materials.* Journal of Materials Science, 1995. **30**: p. 5321-5327.

66. Rybakov, K.I. and V.E. Semenov, *Possibility of plastic deformation of an ionic crystal due to the nonthermal influence of a high-frequency electric field.* Physical Review B, 1994. **49**(1): p. 64-68.

67. Rowley, A.T., et al., *Microwave-assisted oxygenation of melt-processed bulk $YBa_2Cu_3O_{7-\delta}$ ceramics.* Journal of Materials Science, 1997. **32**: p. 4541-4547.

68. Liu, P., et al., *Microwave synthesis of nano-titanium carbide.* Advanced Materials Research 2012. **399-401**: p. 561-564.

69. Standish, N. and H. Worner, *Microwave Application in the Reduction of Metal Oxides with Carbon.* Journal of Microwave Power and Electromagnetic Energy, 1990. **25**(3): p. 177-180.

70. Rahaei, M.B., et al., *Mechanochemical synthesis of nano TiC powder by mechanical milling of titanium and graphite powders.* Powder Technology, 2012. **217**(0): p. 369-376.

71. Li, S.-B., et al., *Formation of TiC hexagonal platelets and their growth mechanism.* Powder Technology, 2008. **185**(1): p. 49-53.

72. Benoit, C., et al., *TiC nucleation/growth processes during SHS reactions.* Powder Technology, 2005. **157**(1–3): p. 92-99.

73. Koc, R., *Kinetics and phase evolution during carbothermal synthesis of Titanium Carbide from ultrafine titania/carbon mixture.* Journal of Materials Science, 1998. **33**: p. 1049-1055.

74. Niyomwas, S., *Synthesis and Characterization of TiC and TiC-Al$_2$O$_3$Composite from Wood Dust by Self-Propagating High Temperature Synthesis.* Energy Procedia, 2011. **9**(0): p. 522-531.

75. Durlu, N., *Titanium Carbide Based Cmposites for High Temperature Applications.* Journal of European Ceramic Society, 1999. **19**: p. 2415-2419.

76. Liang, Y. and S.P. Dutta, *Application trend in advanced ceramic technologies.* Technovation, 2001. **21**(1): p. 61-65.

77. Lee, D.W., S. Alexandrovskii, and B.K. Kim, *Mg-thermal reduction of TiCl$_4$+C$_x$Cl$_4$ solution for producing ultrafine titanium carbide.* Materials Chemistry and Physics, 2004. **88**(1): p. 23-26.

78. Zhang, H., et al., *Preparation of titanium carbide powders by sol-gel and microwave carbothermal reduction methods at low temperatures. .* Journal of Sol-Gel Science and Technology, 2008. **46**: p. 217-222.

79. Mohapatra, S., D.K. Mishra, and S.K. Singh, *Microscopic and Spectroscopic Analysis of TiC Powder Synthesized by Thermal Plasma Technique.* Powder Technology, 2013. **237**: p. 41-45.

80. Force, E.R., *Geology of Titanium-Mineral Deposits.* Vol. 259. 1991, Boulder, Colorado: The Geological Society of America, Inc.

81. Sundararajan, M., et al., *Characterization of Ilmenite from Kerala Coastline, India: Implications in the Production of Synthetic Rutile.* Journal of Minerals and Materials Characterization and Engineering, 2009. **8**(6): p. 427-438.

82. Ahmad, I., R. Dalton, and D. Clark, *Unique Application of Microwave Energy to the Processing of Ceramic Materials.* Journal of Microwave Power and Electromagnetic Energy, 1991. **26**(3): p. 128-138.

83. Winkler, B., et al., *In situ observation in the formation of TiC from the elements by neutron diffraction.* Journal of Alloys and Compounds, 2007. **441**: p. 374-380.

84. Humenik, M. and N.M. Parikh, *Cermets: I, Fundamental Concepts Related to Micro-structure and Physical Properties of Cermet Systems.* Journal of the American Ceramic Society, 1956. **39**(2): p. 60-63.

85. Subramanian, P.R., et al., *Advanced intermetallic alloys—beyond gamma titanium aluminides.* Materials Science and Engineering: A, 1997. **239–240**(0): p. 1-13.

86. Tiegs, T.N., et al., *Ceramic composites with a ductile Ni$_3$Al binder phase.* Materials Science and Engineering: A, 1996. **209**(1–2): p. 243-247.

87. Subramanian, R., et al., *Iron aluminide-titanium carbide composites by pressureless melt infiltration — Microstructure and mechanical properties.* Scripta Materialia, 1996. **35**(5): p. 583-588.

88. Subramanian, R. and J.H. Schneibel, *FeAl-TiC cermets—melt infiltration processing and mechanical properties.* Materials Science and Engineering: A, 1997. **239–240**(0): p. 633-639.

89. Subramanian, R. and J.H. Schneibel, *FeAl–TiC and FeAl–WC composites—melt infiltration processing, microstructure and mechanical properties.* Materials Science and Engineering: A, 1998. **244**(1): p. 103-112.

90. Claussen, N., D.E. Garcia, and R. Janssen, *Reaction sintering of alumina-aluminide alloys (3A).* Journal of Materials Research, 1996. **11**(11): p. 2884-2888.

91. Schneibel, J.H., et al., *Liquid-phase sintered iron aluminide-ceramic composites.* Intermetallics, 1997. **5**(1): p. 61-67.

92. Garcia, D.E., et al., *Synthesis of Novel Niobium Aluminide-Based Composites.* Journal of the American Ceramic Society, 1997. **80**(9): p. 2248-2252.

93. Schicker, S., et al., *Reaction Processing of Al_2O_3 Composites Containing Iron and Iron Aluminides.* Journal of the American Ceramic Society, 1997. **80**(9): p. 2294-2300.

94. Choi, Y., J.K. Lee, and M.E. Mullins, *Densification process of TiCx–Ni composites formed by self-propagating high-temperature synthesis reaction.* Journal of Materials Science, 1997. **32**(7): p. 1717-1724.

95. Fan, Q., H. Chai, and Z. Jin, *Role of iron addition in the combustion synthesis of TiC–Fe cermet.* Journal of Materials Science, 1997. **32**(16): p. 4319-4323.

96. Dunmead, S.D., et al., *Kinetics of Combustion Synthesis in the Ti-C and Ti-C-Ni Systems.* Journal of the American Ceramic Society, 1989. **72**(12): p. 2318-2324.

97. LaSalvia, J.C. and M.A. Meyers, *Combustion synthesis in the Ti-C-Ni-Mo system: Part II. Analysis.* Metallurgical and Materials Transactions A, 1995. **26**(11): p. 3011-3019.

98. Brinkman, H.J., et al., *Production of Al–Ti–C grain refiner alloys by reactive synthesis of elemental powders: Part I. Reactive synthesis and characterization of alloys.* Journal of Materials Research, 2000. **15**(12): p. 2620-2627.

99. Bandyopadhyay, S., H. Dutta, and S.K. Pradhan, *XRD and HRTEM characterization of mechanosynthesized $Ti_{0.9}W_{0.1}C$ cermet.* Journal of Alloys and Compounds, 2013. **581**(0): p. 710-716.

100. Rudy, E., *Phase Equilibria Investigation of Binary, Ternary, and Higher Order Systems. Part I. The Phase Diagram of the Systems Ti-Nb-C, Ti-Ta-C, and Ti-Mo-C.* 1970, Aerojet-General Corporation Materials Research Laboratory: Sacramento. p. 132.

Chapter 2

Experimental Theory and Methods

2.1 Microwave Radiation and Instrumentation.

A material can interact with radiation of wavelengths from meter to millimeter (microwaves, MWs) if either permanent or induced dipoles are present. Such a material is referred to as dielectric. In a dielectric, dipoles will generally be in random orientations if no electric field (**E**) is applied, while an applied field **E** – for example, if the dielectric is placed between two charged plates - will polarize the material by orienting the dipole moments of polar molecules. This reorientation of dipoles decreases the effective electric field (E_{eff}) between the plates, while increasing the capacitance[5] of the plate structure. The dielectric constant, ε', is the factor by which the E_{eff} is decreased by the polarization of the dielectric:

$$E_{eff} = E - E_{polarization} = \frac{\sigma}{\varepsilon'\varepsilon_0} \qquad \text{Eq.2.1}$$

Here, σ is the charge per unit area and ε_0 is the permittivity of free space (8.854×10^{-12} F m^{-1}).

---

[5] In the case of two parallel charged plates, capacitance is equal to the ratio between the magnitude of charge stored on each plate, Q [Coulomb], and the voltage applied to the plates, V [Volt]. Therefore, C[Farad]=Q/V.

The reorientation of dipoles in an applied alternating field **E** is significant in the case of MWs and when the dipolar reorientation is unable to respond to the frequency of the alternating field **E** of the MWs, a phase lag happens which gives rise to a polarization current in phase with the applied field [1]. As consequence, heating in the material is observed.

a) Unpolarized electrodes

b) Polarization of electrodes when a dielectric is present and an external electric field is applied
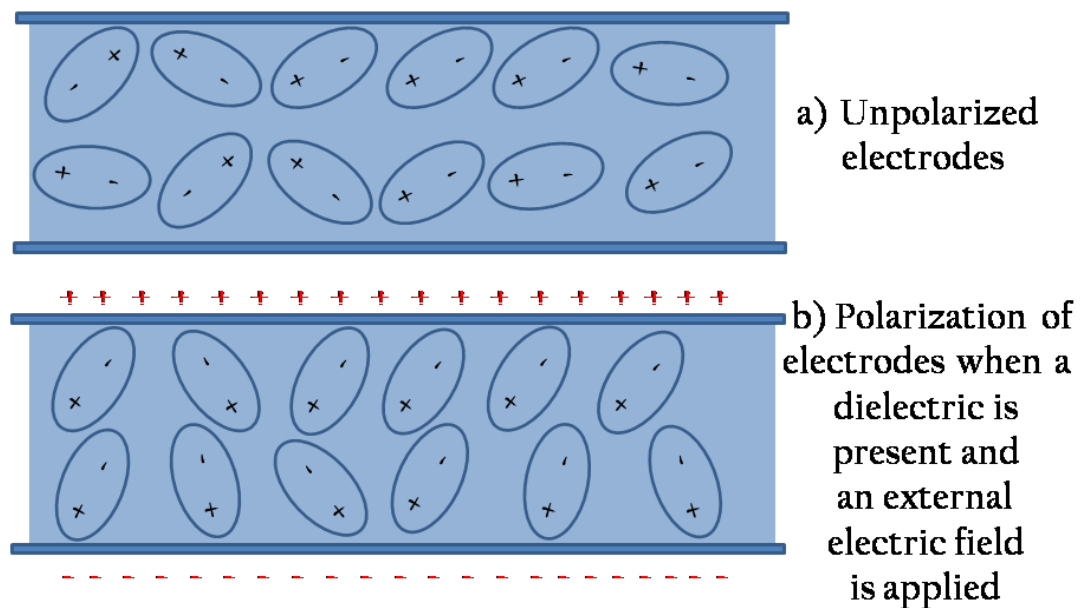
Figure 2.1. a) Schematic of two charged plates (electrodes) without applying an external electric field. b) The polarization of the dielectric produces an electric field opposing the field of the charges of the plates. The dielectric acts as a capacitor, allowing charge to be stored. As consequence, no conductivity is observed between the two plates [2]. (Picture adapted from: http://hyperphysics.phy-astr.gsu.edu/hbase/electric/dielec.html).

Dielectric heating is the process according to which dielectrics absorb MW energy [2]. In general, depending on the nature of materials, four mechanisms of dielectric heating can occur:

1) *Dipolar polarization*. It is caused by the molecular friction given by the reorientation of the dipole moments of the material under the influence of a MW field. This happens for liquids. Water represents an example, as shown in Fig. 2.2.

(a)	(b)	(c)	(d)
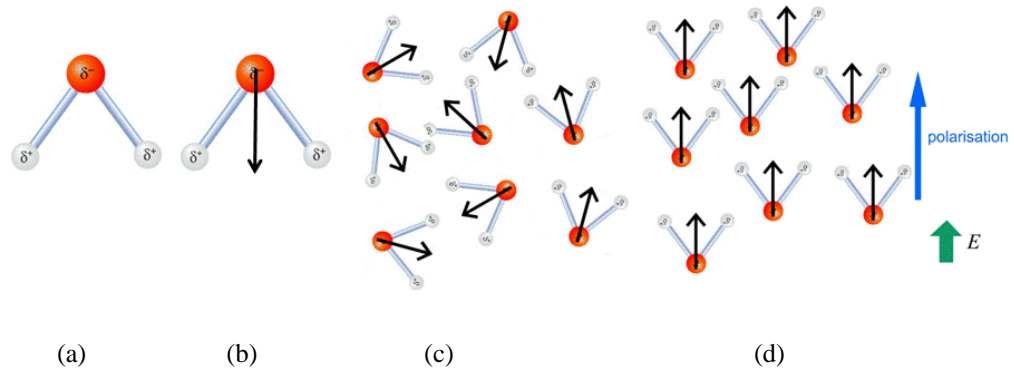
Figure 2.2 (a) H_2O molecules showing a permanent dipole. (b) Permanent dipoles are usually represented by an arrow. (c) In thermal equilibrium, dipoles are randomly arranged. The dipole moments from different molecules cancel out and the net polarization is zero. (d) When applying an external electric field, dipoles rotate in order to align with the field **E** and with each other: the net polarization is therefore non-zero. (Picture adapted from: http://www.doitpoms.ac.uk/tlplib/dielectrics/polarisation_mechanisms.php).

2) *Ionic polarization*. Permanent dipoles also exist in ionic structures such as crystals, and ionic polarization is a mechanism very similar to dipolar polarization described above for molecules in liquids. When no field is applied ($|E| = 0$), internal dipoles in an ionic solid exactly cancel each other and are unable to rotate. The applied external field induces net dipoles by slightly displacing the ions from their thermal equilibrium position (Fig.2.3).
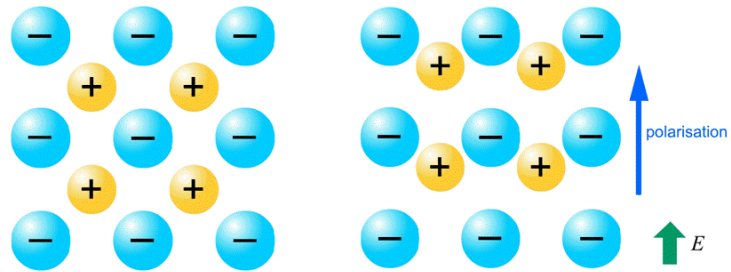
Figure 2.3 Very similar to dipolar polarization, ionic polarization occurs in crystals under external field *E*. (Picture adapted from: http://www.doitpoms.ac.uk/tlplib/dielectrics/polarisation_mechanisms.php).

3) *Electronic (or atomic) polarization*. It happens because a field **E** will always displace the center of charge of the electrons with respect to the nucleus, inducing a dipole moment (Fig. 2.4). This polarization usually takes place in the case of atoms with a spherical symmetry, like noble gases, in all aggregate forms.
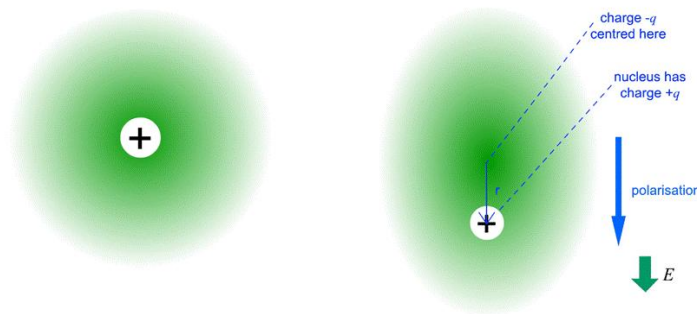
Figure 2.4 In the case of noble gases, dielectric heating occurs when its electron cloud has been shifted by the influence of an external charge, and it is not centered on the nucleus. (Picture taken from: http://www.doitpoms.ac.uk/tlplib/dielectrics/polarisation_mechanisms.php).

4) *Interphase polarization mechanism*. This occurs especially in metals showing surfaces, grain boundaries, interphase boundaries containing dipoles, which are charged by the external field **E** and contribute to the overall polarization of the material [2]. This effect often also happens

50

between particles of different phases which may have different electronic properties.

The dielectric interaction of materials with MWs is expressed principally by two parameters, the power density, P [W/m^3] - Eq. 2.2 - and the penetration depth of MWs, D [m] - Eq. 2.6:

$$P = \sigma|E|^2 = 2\pi f \varepsilon_0 \varepsilon''|E|^2 = 2\pi \varepsilon_0 \varepsilon' \tan\delta |E|^2 \qquad \text{Eq. 2.2}$$

In Eq. 2.2, $\mathbf{E}$ and f are the electric field intensity (V m^{-1}) and its frequency (Hz), respectively; ε_0 is the permittivity of free space (see also Eq. 2.1), ε'' is the dielectric loss, and $tan\ \delta$ is the loss factor, equal to:

$$\tan\delta = \frac{\varepsilon''}{\varepsilon'} \qquad \text{Eq. 2.3}$$

The dielectric constant ε' - or relative permittivity - is the ratio of the permittivity of a substance to that of free space. It is a measure of the response of the material to the external field $\mathbf{E}$. The dielectric loss, ε'', quantifies the ability of the material to convert the absorbed MW power into heat. These two components are commonly expressed in terms of the complex dielectric permittivity, ε^* [F/m]:

$$\varepsilon^* = \varepsilon' - i\varepsilon'' \qquad \text{Eq. 2.4}$$

When the absorbed MW power in the material is converted into heat, it leads to a temperature increase, according to Eq. 2.5:

$$\frac{\Delta T}{\Delta t} = \frac{2\pi f \varepsilon_0 \varepsilon''|E|^2}{\rho C} \qquad \text{Eq.2.5}$$

where C (J/kg·K) is the specific heat of the material. The increase ΔT in temperature is dependent on the density ρ of the sample: as the density

51

increases (and the corresponding thermal conductivity increases) the heating rate decreases [3].

The penetration depth, *D,* determines the depth at which the incident power is reduced by one half exhibiting the uniformity of heating throughout the material:

$$D = \frac{\lambda \sqrt{\varepsilon'}}{2\pi\varepsilon''}$$

Eq. 2.6

Materials with higher loss factor ε'' (imaginary part of the complex permittivity) show faster microwave energy absorption. The power density will decrease exponentially from the surface to the core region. Moreover, high frequencies and large values of the dielectric properties will result in a surface heating, while low frequencies and small values of dielectric properties will result in more volumetric heating [4, 5]. *D* is a very important parameter, because it gives an upper limit to the thickness of the material that can be heated directly with MWs.

Materials are classified into three groups with respect to their interaction with MWs (Fig. 2.5):

a) MW transmitters (*i.e.*, quartz, zirconia, several glasses and ceramics with no transition metals, Teflon, etc…) which are transparent to MWs. These are used as sample holders or containers for MW reactions;

b) MW reflectors, such as bulk metals and alloys (*i.e.*, brass). They are normally used for waveguides;

c) MW absorbers (*i.e.*, silicone, urethane, natural rubber) which are able to take up the energy from the MW field and get heated up very rapidly, thus playing an important role in MW reactions [6].
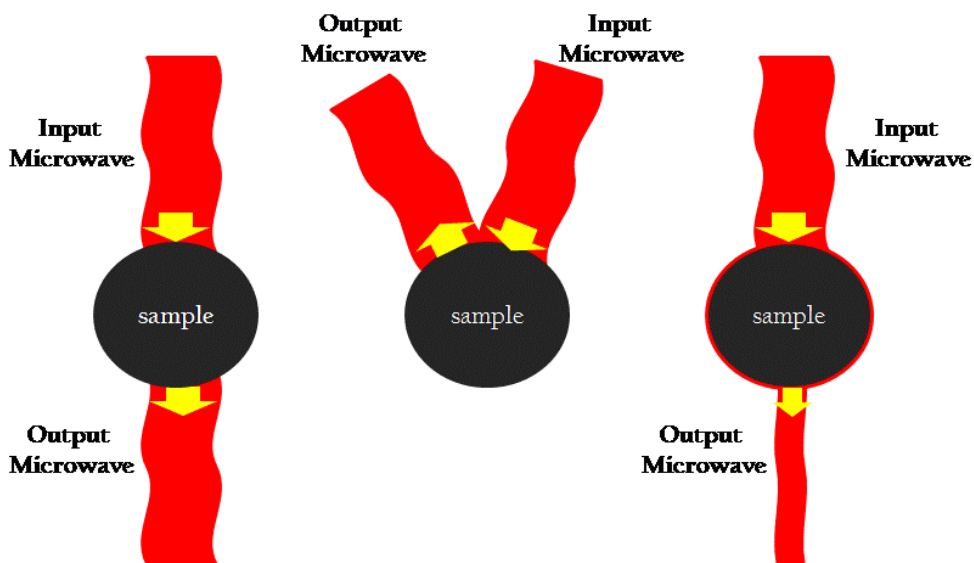
Figure 2.5 Materials are grouped into three categories (from left to right): MW transmitters; MW reflectors, and MW absorbers.

Summarizing, the polarization of dielectrics and consequent MW heating arises from the finite displacement of charges or the rotation of dipoles in a field **E**. It is a different mechanism than that occurring in conventional ovens, which results from translational motion of charges. In the conventional heating mechanism, heat is transferred through conduction, radiation and convection. The surface of the material is heated first, followed by the heat moving inward [4]. In the MW case, a heat propagation from inside to outside is observed (Fig. 2.6).
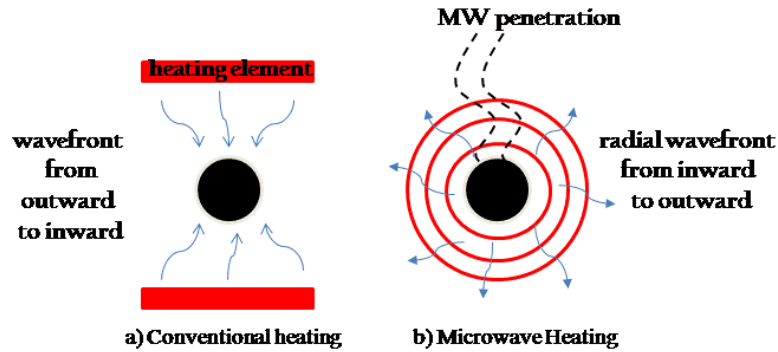
Figure 2.6 Difference between conventional and MW heating. A wavefront is the surface of points of the radio wave having the same phase.

2.1.1 Microwave Instrumentation for Single Mode Cavity (SMC) and Multi Mode Cavity (MMC) reactors.

MW sources. To achieve the high power and frequencies required for MW heating, most of MW sources are vacuum tubes – such as magnetron tubes and travelling wave tubes (TWTs). Magnetrons are used in domestic microwave ovens (DMOs) and in industrial-scale MW devices. They use resonant structure to generate the electromagnetic field, therefore they are able of generating only fixed frequency electromagnetic fields. Magnetrons are made of thermo-ionic diodes with heated cathodes, acting as source of electrons [6]. In vacuum tubes, the circular anode is concentric and surrounds the cathode (Fig 2.7(a)). The anode is at a high potential compared to the cathode (potential difference between the two electrodes: 2-20 kV) thus producing a strong electromagnetic field. Electromagnetic radiation is generated from the acceleration of electrons; these are emitted by the cathode and accelerated radially towards the

54

anode by the electric field. An external magnet is used, at the top and the bottom, to create a magnetic field orthogonal to the electric field, so that the electrons move circularly - rather than directly - to the anode, creating a swirling cloud of electrons.

(a)

b)
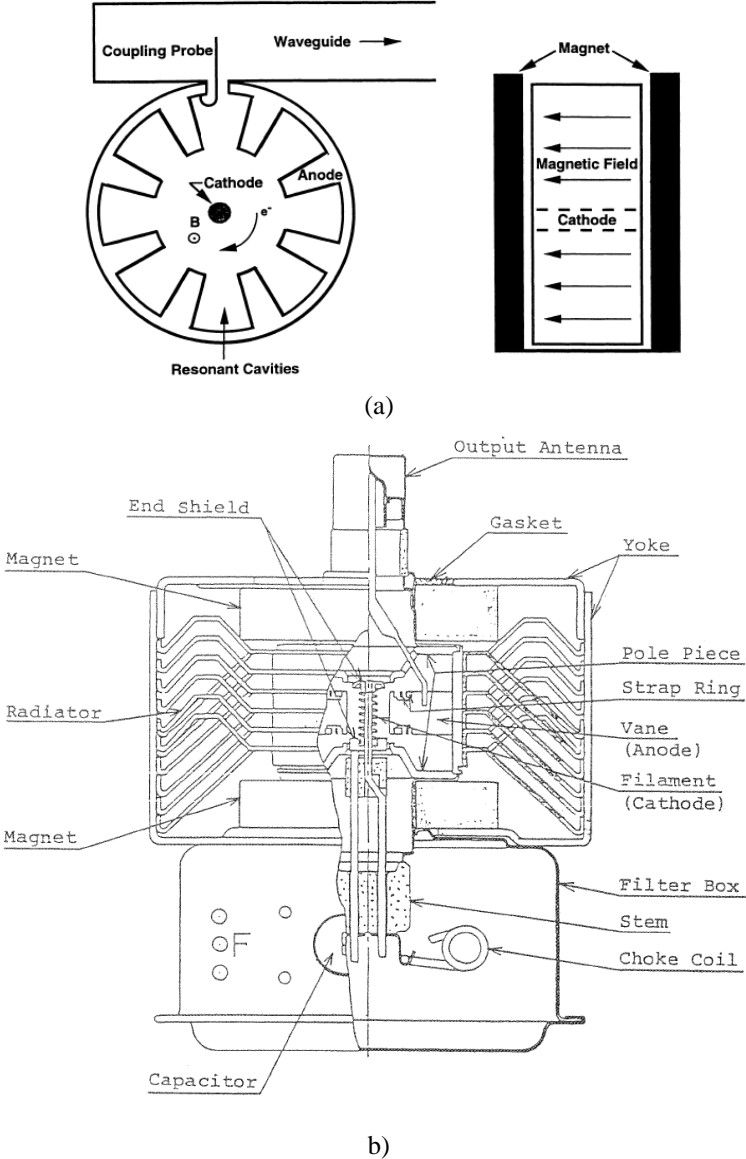
Figure 2.7 a) Schematic diagram of the magnetron tube: top view (left); side view (right), as in reference [7]. b) Scheme of a DMO magnetron, as in reference [8].

As the electrons pass the resonant cavities on the anode, the cavities set up oscillations in the electron clouds and frequency of the oscillation depends on the size of the cavity (Fig. 2.8). The electromagnetic field is then extracted by an antenna and channeled to the cavity through a coaxial cable or a waveguide (see following section on "*Waveguides*").

| a) | b) |
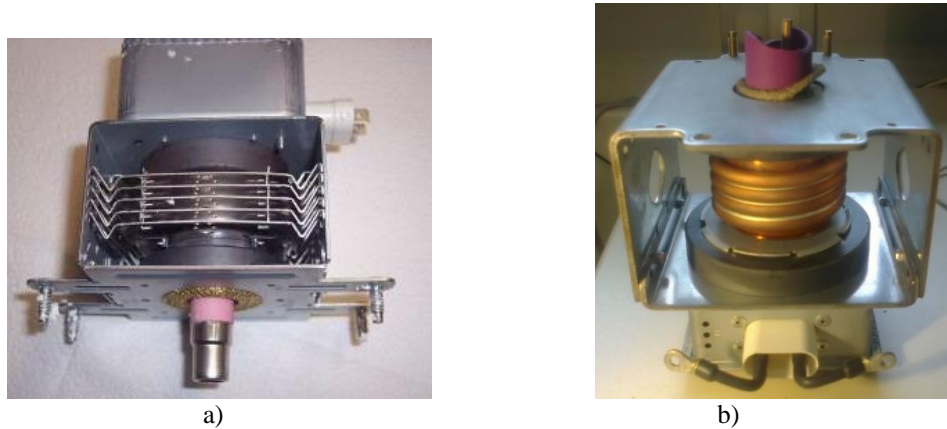
Figure 2.8 a) A DMO magnetron section (Picture taken from http://www.microwaves101.com/encyclopedia/magnetron.cfm). b) A *Sairem*® 2 kW magnetron section (this magnetron has been used in the thesis: the ceramic protection of the antenna has been broken by an arc, which occurred during experiments).

The output power of the magnetron can be controlled either by adjusting the period of operation or adjusting the cathode current or magnetic field strength. In DMOs, the magnetron operates at full power and the average output power is controlled by cycling the current on and off for segments of time. This on/off mechanism is referred to as "duty cycle control".

In industrial MWs generators, a continuous, variable power is provided so that the output average power can be varied by changing the current amplitude of the cathode or by varying the intensity of the magnetic field. These magnetrons can display both the generated *forward power* (FP) and the amount of MW energy reflected by the system components (or

56

sample) back to the magnetron, the *reflected power* (RP). They have a circulator, which is a three-port ferrite device allowing transmission of energy in one direction only (from magnetron to applicator). In a three-port circulator, one port is connected to the MW source, another to the applicator and a third port goes to a dummy load, which deflects the RP energy into a water load, thus preventing the RP to bounce back into the magnetron (see, for example, Fig. 2.13).

High-power Travelling Wave Tubes (TWTs) are used as MW source for variable frequency MWs. While in magnetrons the tube is used both to create the frequency of oscillation and to amplify the signal, TWT is used as amplifier only. A voltage-controlled oscillator generates the MW signal and then the signal is sent to the TWT for amplification (Fig. 2.9).
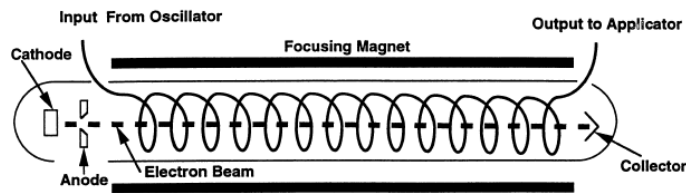
Figure 2.9 TWT, as in reference [7], consisting of two main components: an electron gun and a helical transmission line. Because there are no resonant structures, TWT can amplify a large variation of frequencies (bandwidth) within the same tube. The heated cathode emits a stream of electrons that is accelerated toward the anode, and the electron stream is focused by an external magnetic field. The purpose of the helix is to slow the phase velocity of the MW (the velocity in the axial direction of the helix) to a velocity approximately equal to the velocity of the electron beam. For amplification of the signal to occur, the velocity of the electron beam should be just faster than the phase velocity of the helix. In this case, more electrons are being decelerated than accelerated, and the signal is amplified because energy is being transferred from the electron beam to the MW field.

Transmission lines. Once generated by the magnetrons, MWs are transported to the cavity, through transmission lines. While in low power devices (such as a DMO) transmission lines are co-axial cables, at higher frequencies and higher power transmission sections are often waveguides, in order to reduce losses that would occur if using coaxial cables.

Waveguides are hollow tubes, in which the electromagnetic waves propagate. The choice of materials is a compromise between high conductivity to minimize losses, corrosion resistance, and ease of manufacture. Aluminum is widely used for waveguides transmitting high power, and is selected for its high electrical and thermal conductivity.

In waveguides, two modes[6] of MW propagation exist (Fig. 2.10(a)):

- Transverse electric (TE): the electric intensity in the direction of propagation is null (E_z=0). A TE mode has been used in this work.

- Transverse magnetic (TM): the magnetic intensity in the propagation direction is null (H_z=0).

A transverse electromagnetic mode (TEM) also exists, where neither the electric nor the magnetic field is in the same direction of signal propagation (Fig. 2.10(b)), but the boundary conditions that apply to waveguides will not allow a TEM wave to propagate. However, the wave in the waveguide will propagate through air or an inert gas dielectric in a manner similar to free space propagation. The phenomenon is bounded by

---

[6] A field pattern within a MW applicator is known as a mode.

the walls of the waveguide and that implies that certain conditions must be met. The boundary conditions for waveguides are:

1. The electric field must be orthogonal to the conductor in order to exist at the surface of that conductor;

2. The magnetic field must not be orthogonal to the surface of the waveguide.

(a)

(b)
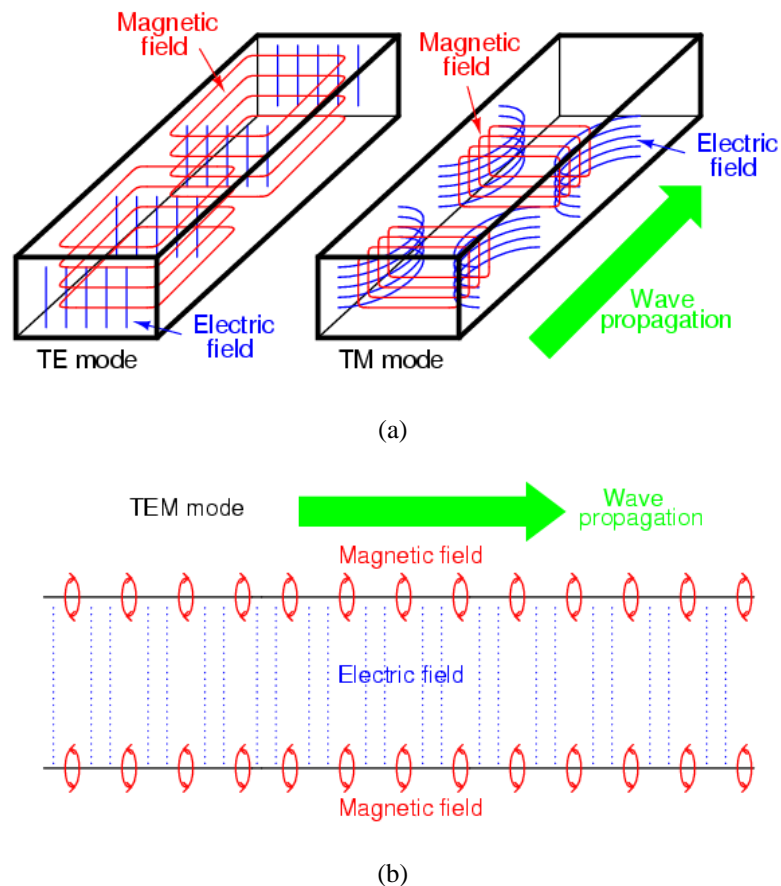
Figure 2.10 a) TE (transverse electric - left) and TM (transverse magnetic - right) mode. (Picture from: http://www.allaboutcircuits.com/vol_2/chpt_14/8.html); b) TEM mode waveguide: both field planes (electrical and magnetic) are perpendicular (transverse) to the direction of signal propagation.

Subscripts (*m* and *n*) are used to complete the description of the field pattern for both TE_{mn} and TM_{mn} modes. In rectangular waveguides, the

first subscript indicates the number of half-wave patterns in the "a" dimension, and the second subscript i ndicates the number of half-wave patterns in the "b" dimension (Fig.2.11-left). For rectangular waveguides, the coordinate system is usually oriented such as $a \geq b$ (a common dimension is 86×43 mm (inner dimensions), as for the WR340-type waveguide described in this thesis. An international standard of waveguides lists the most common optimum waveguide type for specific frequencies [9]. A similar system is used to identify the modes of circular waveguides (Fig. 2.11-right); however, in this case, the subscripts have a different meaning. The first subscript indicates the number of full-wave patterns around the circumference of the waveguide, and the second subscript indicates the number of half-wave patterns across the diameter.

The size of the waveguide determines the mode of MW that are propagated – so the optimum size for a specific frequency band is a compromise of minimizing power loss and heating, requiring a large cross-section and avoiding possible excitation of higher-order modes [10].
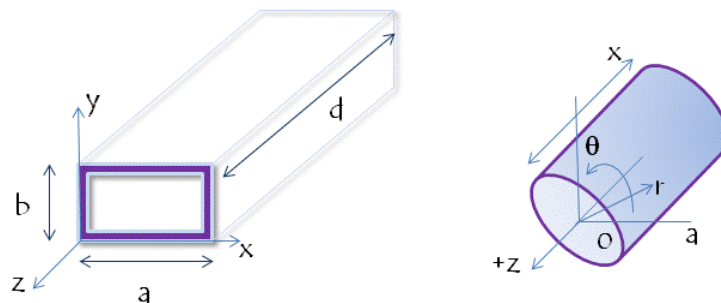
Figure 2.11 Scheme of a rectangular waveguide, in Cartesian coordinate system (left). Scheme of a circular (or cylindrical) waveguide of radius *a,* in cylindrical coordinate system. In both cases, the waveguide is positioned with the longitudinal direction along the *z*-axis.

The mode equation for a rectangular cavity is shown in Eq. 2.7:

$$f_{nml} = c\left[\left(\frac{1}{2d}\right)^2 + \left(\frac{m}{2b}\right)^2 + \left(\frac{n}{2a}\right)^2\right]^{1/2}$$

Eq. 2.7

Here f_{nml} is the TE$_{nml}$ or TM$_{nml}$ mode's resonant frequency; c is the speed of light; n, m, l, are the number of half-sinusoidal variations in the standing wave pattern along the x, y, and z-axes, respectively; a, b, and d are the dimensions of the cavity in the x, y and z directions.

The cutoff frequency (or corresponding wavelength) of an electromagnetic waveguide is the lowest frequency (respectively, the longest wavelength) for which a mode will propagate in it.

In the rectangular case, Eq. 2.8 defines the lower cut-off frequency [in Hz] for a particular mode:

$$(f_c)_{nm} = \frac{1}{2\pi\sqrt{\mu\varepsilon_0}}\sqrt{\left(\frac{m\pi}{a}\right)^2 + \left(\frac{n\pi}{b}\right)^2}$$

Eq.2.8

the lower cut-off wavelength [m] is shown in Eq. 2.9:

$$(\lambda_c)_{mn} = \frac{2}{\sqrt{\left(\frac{m}{a}\right)^2 + \left(\frac{n}{b}\right)^2}}$$

Eq. 2.9

Here a is the internal width (the longer dimension) [in m], b is internal height (the shortest dimension) [in m], m and n are, respectively, the number of half-wavelength variations of fields in the a direction and the

number of half-wavelength variations of fields in the b direction − as described above, while ε_0 is the permittivity of free space as already defined in Eq 2.1, and μ is the permeability of free space $(1.2566370614 \times 10^{-6}$ H/m$)$[7].

The dominant mode of any waveguide is the one of lowest cut-off frequency. From Eq. 2.8, it follows that the TE_{10} mode is the dominant mode of a rectangular waveguide with a>b, since it has the lowest attenuation of all modes. Either m or n can be zero, but not both. For TM guides, TM_{11} is the dominant mode, as $m=0$ and $n=0$ are not possible.

In the cylindrical case, the lower cut-off wavelength (or frequency) for a particular TE mode is determined by the following equation:

$$(\lambda_c)_{mn} = \frac{2\pi r}{p'_{mn}}$$
Eq. 2.10

where p'_{mn} is given in Table 2.1 for values of m=0,1,2:

m	p'_{m1}	p'_{m2}	p'_{m3}
0	3.832	7.016	10.174
1	1.841	5.331	8.536
2	3.054	6.706	9.970

Table 2.1. Values for p'_{mn} for cylindrical waveguides.

It follows that in cylindrical wave, TE_{11} is the dominant mode. The lower cutoff wavelength (or frequency) for a particular TM mode in circular waveguide is given by the following Eq. 2.11:

---

[7] Reference:http://www.rfcafe.com/references/electrical/waveguide.htm

$$ (\lambda_c)_{mn} = \frac{2\pi r}{p_{mn}} \qquad\qquad\text{Eq. 2.11} $$

where p_{mn} is given in Table 2.2, for values of m=0,1,2:

m	p_{m1}	p_{m2}	p_{m3}
0	2.405	5.520	8.654
1	3.832	7.016	10.174
2	5.135	8.417	11.620

Table   2.2   Values   for p_{mn} cylindrical   waveguides (http://www.rfcafe.com/references/electrical/waveguide.htm).

TM_{11} is the dominant mode for cylindrical TM guides.

Tuner. Tuners are used to maximize the power absorbed by the load (namely, the sample) through impedance matching (i.e., by reducing reflection to zero between source and load). They also resize the cavity to make it resonant at the working frequency of the source, as the presence of the sample perturbs the resonant frequency, so that the level of the desired signal at the load is optimized. Several tuners exist, such as irises, three-stub tuners, and E-H plane tuners. In this thesis, a three-stub tuner has been used. Most practical stub tuners make use of transmission line segments in which the segments are either open or short circuited [11].

In a standard stub tuner, the stubs are brass threaded bolts mounted in a flanged waveguide section. By setting the stubs for minimum RP from the load/tuner combination, it is possible to generate a reflection of any amplitude and phase, thus maximizing the power absorbed by the load. A stub tuner can be used at both low and high power.

63

Applicator. Applicators are devices designed to ensure the transfer of electromagnetic energy from the transmission line to the load. It is where the MW/sample interaction occurs.

Common types of applicators used in materials processing are: 1) multimode (MMC), and 2) single mode cavity (SMC) systems. Travelling wave applicators are also employed, but their use is mainly for continuous flow system, which is not the case of the work described in this thesis.

1) Multi mode applicators are capable of sustaining a number of high order modes at the same time, and these are commonly used in DMOs. The various modes result in non-uniformity inside the cavity, where regions of high and low electric fields are present. As the size of the MW cavity increases, the number of possible resonant modes also increases. Consequently, MMC are much larger than one wavelength.

In MMC, the presence of different modes gives multiple hot spots within the MW cavity. For cooking in DMOs (operating at 2.45 GHz), for example, this difficulty can be overcome by using a turntable that rotates during operation so that the food passes through areas of high power and therefore is subject to time-averaged, uniform heating. Another technique to improve uniformity is to use mode stirrers. These are reflectors similar to fans which rotate within the cavity near the waveguide input. These mode stirrers reflect waves off the irregularly shaped blades and constantly redistribute the magnetic field thus creating time-averaged uniformity in a similar way to turntables. But still, the non-uniformity of

MW field causes disadvantages when DMOs is used for synthesis and processing, such as unpredictable mode patterns, poor reproducibility of the synthesis results and the inability to modulate the power output. However, MMCs are cheap and readily accessible.

2) Unlike MMCs, theoretical analysis can be performed in an SMC to describe the response of MWs. An SMC consists of a metallic cage in which a MW signal of the correct electromagnetic field polarization will undergo multiple reflections. The superposition of the reflected and incident waves gives rise to a standing wave pattern, very well defined in space. Since the MW power density (Equation 2.2, in Section 2.1) is proportional to the electric field strength inside the material squared, such cavities offer extremely rapid heating rates and give the opportunity to heat materials transparent to MWs in an MMC.

The present thesis project builds on the results obtained through a collaboration between the University of Glasgow and the University of Nottingham, in which it was demonstrated that ultrarapid, energy efficient processing of materials was possible with MW irradiation [12, 13]. In that case, a *Sairem*® 3-5 kW GMP 150SM microwave-generator was used, connected through a WR430 waveguide to an automatic E-H tuner for impedance matching. The tuner was connected to an 82 mm internal diameter TE_{10n} single mode cavity (Fig. 2.12(a)). A short circuit tuner terminated the waveguide. In Fig 2.12(b), a schematic representation of

the position of the sample inside the cavity is depicted [13, 14]. Pyrometer

readings for temperature measurements were performed.
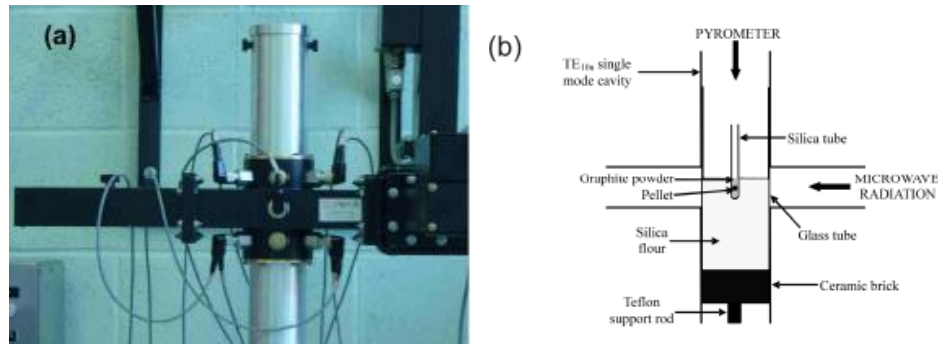
Figure 2.12 a) Photographic and b) schematic representation of the TE_{10n} MW heating cavity.

In this thesis, a single mode microwave cavity reactor − operating at a frequency of 2.45 GHz - able to promote material processing probed by in situ powder neutron diffraction (PND) has been designed and optimized (Fig 2.13). A detailed description will be given in Chapter 3.
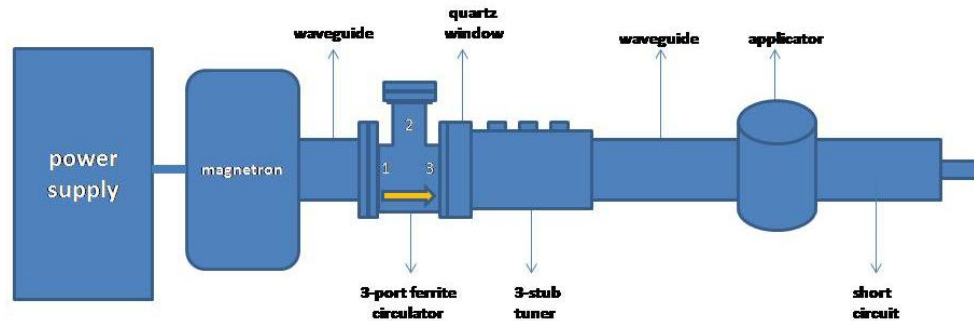
Figure 2.13. Schematic of a SMC MW device, suitable for material processing comprising a power supply; magnetron; rectangular waveguide; 3-port ferrite circulator; quartz window (for preventing plasma discharge destroying the magnetron); tuner; waveguide; applicator - also called cavity - (cylindrical or rectangular); short circuit (or metal plate). It is difficult to heat ceramics with a domestic microwave oven (MMC), because ε" for ceramics is extremely small compared to that, for example, of food. (The MMC type is suitable for heating of materials of comparatively large ε", and the SMC type is suitable for that of small ε") [15].

The main advantage of a SMC is that through proper design, the MW field can be focused at a given location. Further, precise knowledge of the electromagnetic field distribution enables materials to be placed in the position of highest field strength for optimum coupling. Therefore, these cavities have been used for laboratory-scale studies, while MMC are typically more versatile for batch operations and processing of large, complicated shape objects because of less stringent spatial requirements.

2.1.2 Temperature measurements.

As already mentioned in Chapter 1, Section 1.3.1, a complicated issue in MW processing of materials is the precise measurement of temperature. The two most common conventional methods for temperature measurement, thermocouples and pyrometers, are both problematic as discussed below.

Thermocouples. Thermocouples directly read the temperature when in contact with the sample. However, this need for thermocouples to make contact with the sample, often gives errors or uncertainties in the measurements. Being an electric conductor, in fact, it is probable that the thermocouple probe will change the local electromagnetic field pattern and therefore heat pattern in the MW [16].

Optical pyrometers (infrared temperature sensors). All materials give off infrared (IR) energy depending on their temperature and an infrared sensor consists of a lens to focus this IR energy to a detector. The detector then converts the energy to an electrical signal that can be displayed in units of temperature. IR temperature sensors do not require to be in contact with a sample to read temperature and, so they do not need to be located inside the cavity. However, field and angle of view (target size and distance), type of surface being measured (emissivity considerations) and the temperature range under consideration must be taken into account for correct measurements. The target being measured should completely fill the field of view of the instrument. Since the IR device determines the average temperature of all surfaces within the field of view, it tends to average local hot and cool spots. Emissivity is defined as the ratio of energy radiated by an object at a given temperature to the energy emitted by a perfect radiator, or black body, at the same temperature. The emissivity of a black body is 1.0. All values of emissivity fall between 0.0 and 1.0. If the emissivity of the sample measured is different from that which is calibrated in the sensor, an error can occur. For most applications, a factory setting is usually sufficient. A schematic of a pyrometer is shown in Fig. 2.14.
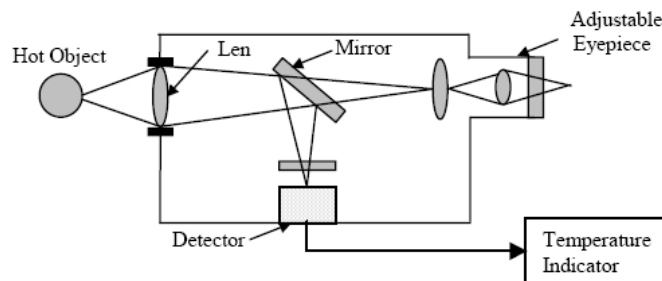
Figure 2.14 Schematic of a pyrometer. An optical system collects the visible and infrared energy from an object and focuses it on a detector. The detector converts the collected energy into an electrical signal to drive a temperature display or control unit. The detector receives the photon energy from the optical system and converts it into an electrical signal. Two types of detectors are used: thermal (thermopile) and photon (photomultiplier tubes). Photon detectors are much faster than the thermopile type. This enables the user to adopt the photon type for measuring the temperature of small objects moving at high speed. (Picture taken from: http://www.globalspec.com/reference/10956/179909/chapter-7-temperature-measurement-radiation-pyrometers).

Temperature measurement during MW reactions is difficult because emissivity changes as the chemical composition of the pellet changes and emissivity also depends on other factors such as size, shape and granularity of the sample. In addition to the issue of emissivity, due to the mechanisms involved during microwave heating the surface temperature of the pellet measured using the optical pyrometer could be significantly different from the bulk temperature.

To overcome these difficulties and avoiding misleading temperature measurements, in the work described in this thesis a crystallographic thermometer has been used as temperature probe, taking advantage of the presence of carbon graphite in all the samples and the fact that the linear thermal expansion of graphite, α, is known with a good accuracy for a wide range of temperatures in literature – 293 to 1473K [17, 18].

From Eq. 2.11, the c-axis value at a given temperature T can be calculated:

$$c(T) = c_{Tr} + \alpha\, c_{Tr}\ (T\text{-}Tr) \qquad\qquad \text{Eq. 2.11}$$

where α is the linear thermal expansion $(27.7(\pm 0.6) \times 10^{-6}\ K^{-1})$, $c(T)$ and c_{Tr} $(=6.7079\ \text{Å},\ \text{at } 298K)$ are the c-axis values at the unknown and at the reference temperature respectively; T and Tr are the unknown and the reference temperature, respectively. The unknown temperature T can be then derived from Eq.2.12:

$$T = T_r + \frac{c(T) - c_{Tr}}{\alpha} \qquad\qquad \text{Eq.2.12}$$

where $c(T)$ is calculated by performing sequential refinement against *in situ* data.

The error on T is given by the root mean square deviation (RMSD). If $\bar{T} = T - T_r$ and $\bar{c} = c - c_r$, then Eq.12 can be rewritten as:

$$\bar{T} = \frac{\bar{c}}{\alpha} \qquad\qquad \text{Eq.2.13}$$

and the error on $\bar{T}$ is given by:

$$\frac{\delta \bar{T}}{\bar{T}} = \sqrt{\left(\frac{\delta \bar{c}}{\bar{c}}\right)^2 + \left(\frac{\delta \alpha}{\alpha}\right)^2} \qquad\qquad \text{Eq.2.14}$$

2.2 Synthesis and Processing

MW synthesis of titanium carbide (TiC) and more complex ternary carbides constituted the main target of this thesis. While the synthesis of

TiC was conducted in both MMC and SMC, starting from both elemental powders (Ti and graphite), and its oxide (TiO_2 and graphite), the ternary carbides were processed in an SMC only, starting from their elemental powders. In all the cases, starting materials were used as purchased.

Mixtures of powders were ground in an agate mortar to make them homogeneous, and then cold pressed using an hydraulic press. Pellets were kept under a pressure of 5 tons for about 10 minutes before being removed. Pressed pellets (8 or 10 mm diameter; 1 g; 1 cm thickness) were embedded in graphite (acting as a MW susceptor) in a 10 or 12 mm diameter open silica tube (MW transparent). In the case of TiC synthesis in an MMC, the quartz tube was placed in a beaker filled with low dielectric loss silica flour.

A summary of the experimental set-up (both MMC and SMC) is reported in the following sections (2.2.1 and 2.2.2, respectively), while more detailed description is given in next Chapters 3 and 4.

2.2.1 Synthesis using a multi mode microwave cavity (MMC)

The synthesis of TiC was conducted in a DMO 800W MMC, operating at 2.45 GHz (Fig. 2.15(a)). All experiments were performed at ambient pressure, in air, using a 12 mm diameter, 1 mm wall thickness quartz tube as reaction vessel, closed at the bottom and open to the top. The tube was then inserted in a glass beaker filled with ground silica (Fig. 2.15(b)),

which provided the mechanical support and the thermal insulation for the quartz tube during the reaction.

(a)
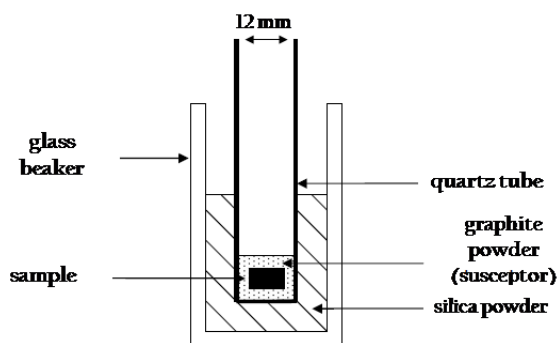
b)

Figure 2.15. a) Picture of the MMC used in the work described in this thesis; a) Schematic of silica beaker plus sample holder (quartz tube).

2.2.2 Synthesis using a single mode microwave cavity (SMC)

Two different SMC systems have been used in the work described in this thesis: a *Gaerling Applied Engineering* magnetron head, 0-1 kW power, 2.45 GHz frequency, available at the Glasgow University (Fig. 2.16(a),(b) and (c)), and a *Sairem®* GMP20K microwave-generator of 2 kW power and 2.45 GHz frequency, available at the ILL (Fig. 2.17).
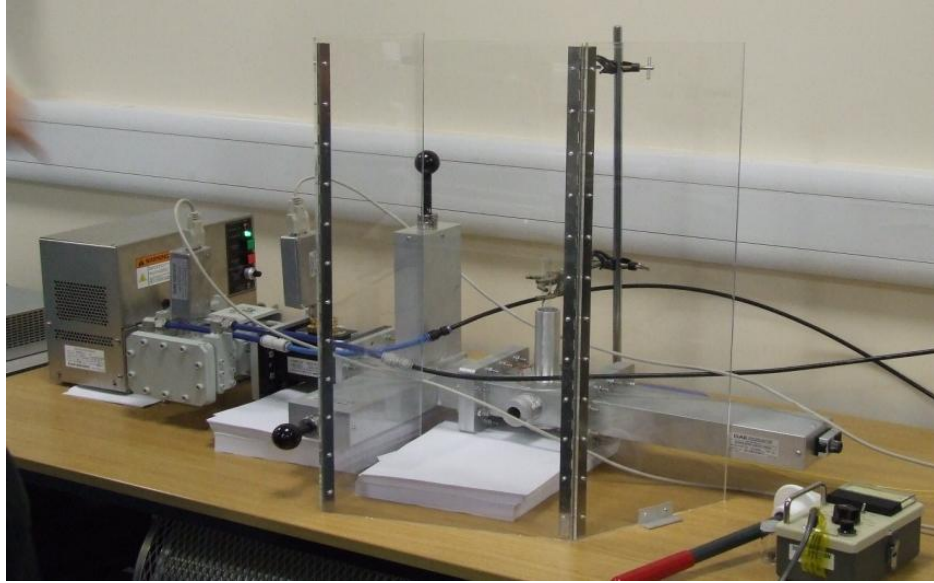
(a)
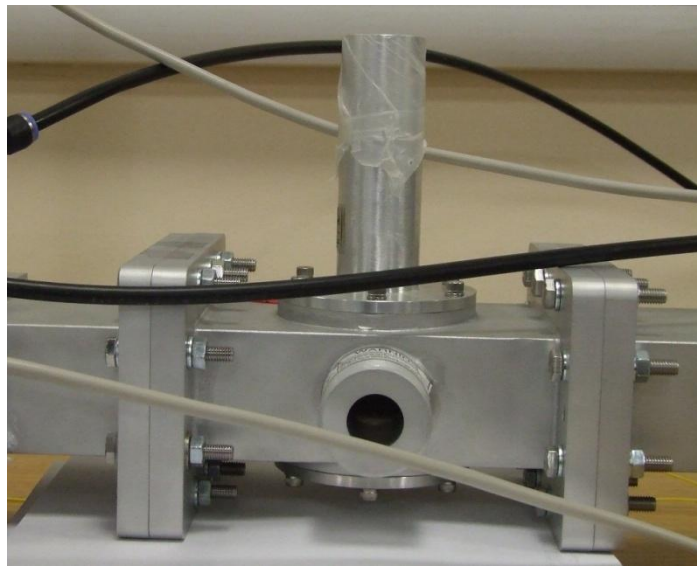
(b)
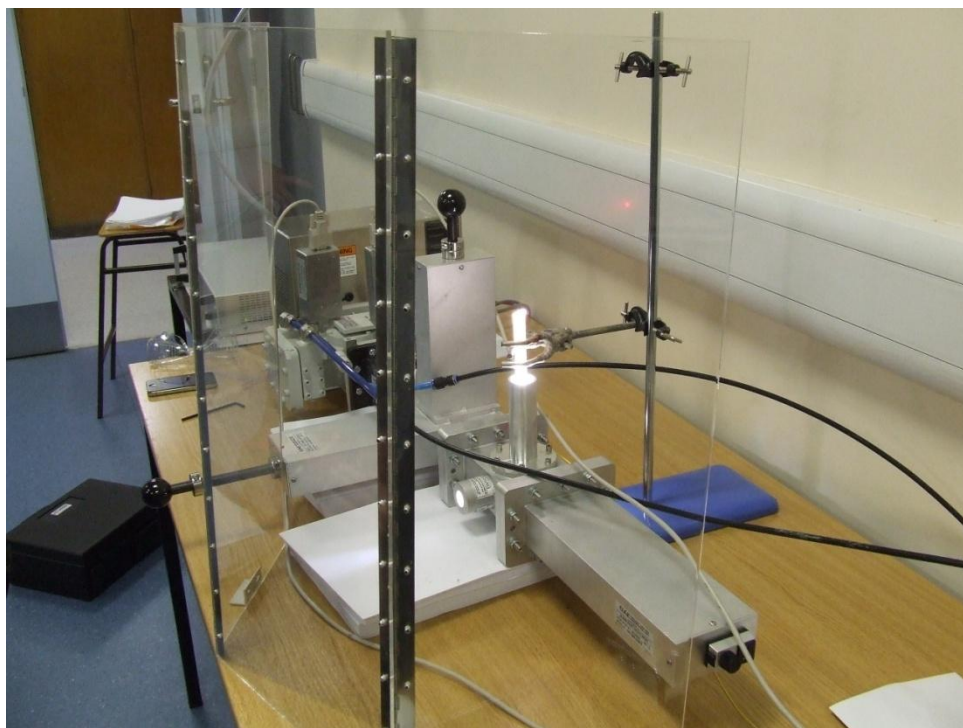
(c)

Figure 2.16 a) MW system used at Glasgow University; b) Cylindrical applicator – with a choke for pyrometer readings; c) TiC reaction under MW irradiation, in act.

In both cases, after initial preparation of the samples, the sample holder (quartz tube, 10 mm diameter, 1 mm wall thickness) was inserted into the SMC. Samples were then irradiated with MWs for a set time and power. Reflective power (RP) was also monitored on a display in both cases to detect anomalies.

2.3 Physical methods to characterize solids

Basic concepts of crystallography are presented in this section, which introduces both powder neutron diffraction (PND) and powder X-ray diffraction (XRD). Rietveld refinement is also discussed and a description

of the two axis diffractometer D20 is given. Raman spectroscopy and Scanning Electron Microscopy (SEM) are also described.

An experimental technique like PND can probe relatively large sample volumes due to the charge neutrality of neutrons.

a)   b)
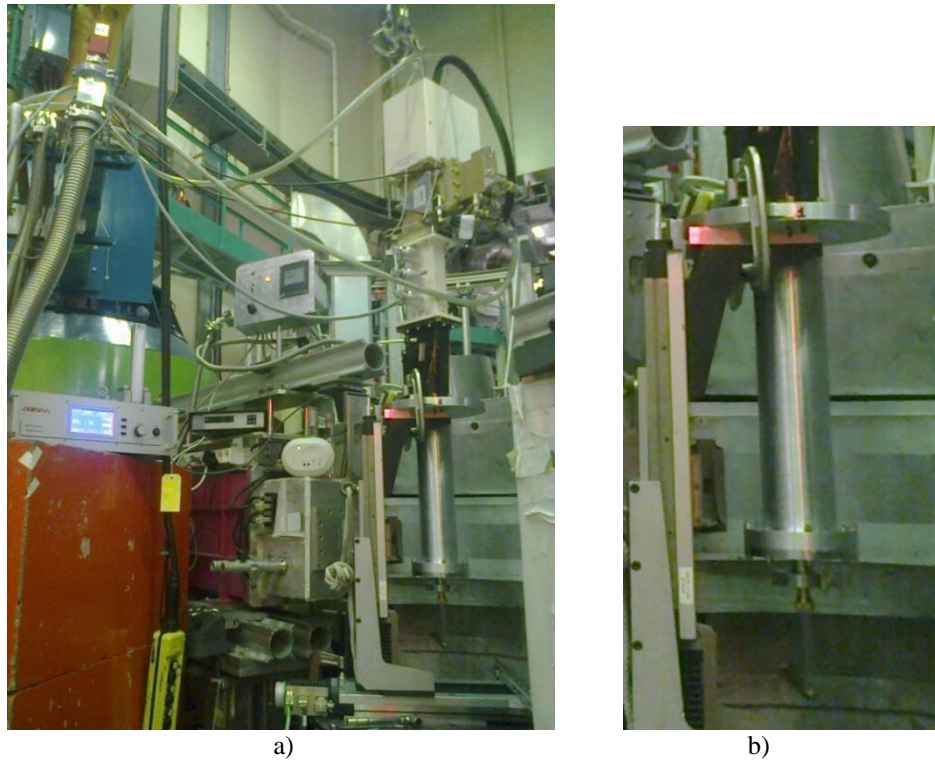
Figure 2.17 a) Single mode MW device, on two-axis diffractometer D20, at ILL. On the power supply display, FP and RP can be read. A MW leakage detector has been installed. b) The single mode cylindrical applicator has been designed specifically for D20. Its design addresses multiple issues, such as avoiding interference with both the sample and the neutron beam, complying with instrument geometry constraints and avoiding activation risks.

In situ PND on D20 has been chosen as an ideal probe to investigate the formation mechanisms of carbides for several reasons:

1) To observe intermediate phases in different $M_z:O_x:C_y$ stoichiometric ratios (where M stands for transition metals). The ability of neutrons to offer very good visibility for C and O, and to discern them more than

electrons or other techniques do, can give insight into the reaction mechanism of carbide formation;

2) To probe fast reactions (time range of seconds). D20 is a high intensity 2-axis diffractometer equipped with a large micro-strip detector gas chamber (MSGC) position sensitive detector (PSD). An extremely high neutron flux (up to 10^8 s^{-1} cm^{-2} at the sample position) makes real-time experiments on very small samples and/or with very short acquisition times possible;

3) To use powder samples, which makes it possible to observe simultaneously a true bulk average over the entire sample volume.

XRD has been used in some cases as an excellent tool for *ex-situ* experiments as it is able to give information on the long-range order of the structures, as PND can do. In addition, they are more easily available at laboratory scale, rather that PND, which makes them a very useful technique able to provide relatively fast answers. Raman spectroscopy has been used in some cases for probing bonding environments in both crystalline and amorphous structures, while SEM gave information about the morphology of some of the reaction products.

2.3.1 Basic Concepts of Crystallography

Crystals are characterised by a "building motif" which continuously repeats in three dimensions. This repeating block is called the *unit cell* of

the crystal and it is described in three dimensions by the length of its edges

a, *b*, and *c* and the α, β and γ angles between them (Fig. 2.18).
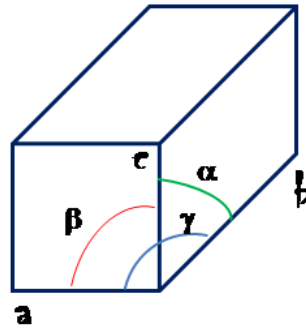
Figure 2.18 *a*, *b*, and *c* and the angles between them (α, between axes *b* and *c*; β, between axes *a* and *c* and γ, between axes *a* and *b*) describe the unit cell.

The size, shape, symmetry of the unit cell, and the position of the atoms within the cell define univocally a crystal. In Fig. 2.19, all the possible unit cell shapes that can fill a three dimensional space are showed. These are the seven crystal systems.

a)   b)   c)   d)   e)   f)   g)
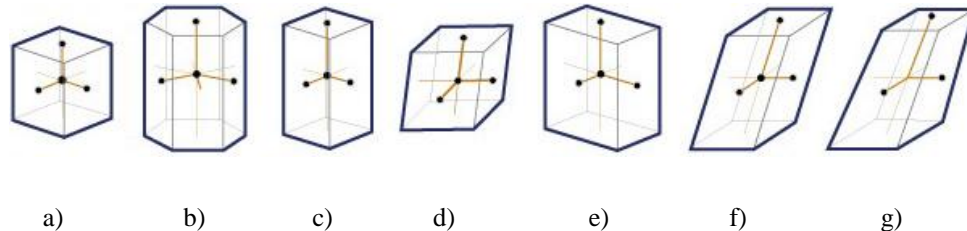
Figure 2.19 The seven crystal systems, listed in order of decreasing symmetry. a) Cubic (a=b=c, α=β=γ=90°); b) Hexagonal (a=b≠c, α=β=90°, γ=120°); c) Tetragonal (a=b≠c and α=β=γ=90°); d) Trigonal (a=b≠c, α=β=90°, γ=120° or alternative setting for the special case of rhombohedral lattice, a=b=c, α=β=γ≠90°); d) Orthorhombic (a≠b≠c, α=β=γ=90°); e) Monoclinic (a≠b≠c, α=γ=90°, β≠90°); f) Triclinic (a≠b≠c, α≠β≠γ≠90°).

Each of the seven crystal systems is governed by the presence or absence of symmetry elements in the structure. Table 2.3 summarises the possible symmetry elements and their two nomenclatures, the *Hermann-Mauguin*

notation – used mostly in crystallography - and the *Schö nflies* notation – used mostly in spectroscopy. The essential symmetry for each of the seven crystal system is listed in Table 2.4.

	Symmetry element	Hermann-Mauguin	Schönflies
Point symmetry	Mirror plane	m	σ_v, σ_h
	Rotation axis	n (=2,3,4,6)	C_n(C_2, C_3, etc.)
	Inversion axis	$\bar{n}$ (= $\bar{1}, \bar{2}, etc.$)	---
	Alternating axis (rotoreflection)	---	S_n(S_1, S_2, etc.)
	Centre of symmetry	$\bar{1}$	i
Space symmetry	Glide plane	n, d, a, b, c	----
	Screw axis	2_1, 3_1, ect.	----

Table 2.3 Symmetry elements.

Crystal system	Essential symmetry
Cubic	Four threefold axes
Hexagonal	One sixfold axes
Tetragonal	One fourfold axis
Trigonal (containing the special case of rhombohedral)	One threefold axis
Orthorhombic	Three twofold axis or mirror planes
Monoclinic	One twofold axis or mirror plane
Triclinic	None

Table 2.4 The essential symmetry for the seven crystal systems.

In three-dimensional space, in order to represent the distribution of atoms in a crystal, an array of points is used. This array - called *lattice* - and its points - called *lattice points* - defines completely the repetition characteristics - while there is no reference to the details of the repeated unit cell or the chemistry or bonding within the crystal. Fourteen distinctive lattices are possible, called Bravais lattices (Fig. 2.20).
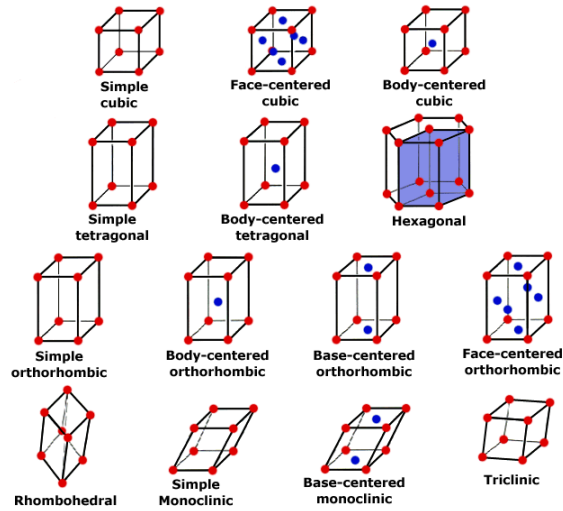
Figure 2.20 The fourteen Bravais lattice (Picture from: http://www.seas.upenn.edu/~chem101/sschem/solidstatechem.html).

These are an infinite array of discrete points generated by a set of discrete translation operations (Fig. 2.21).
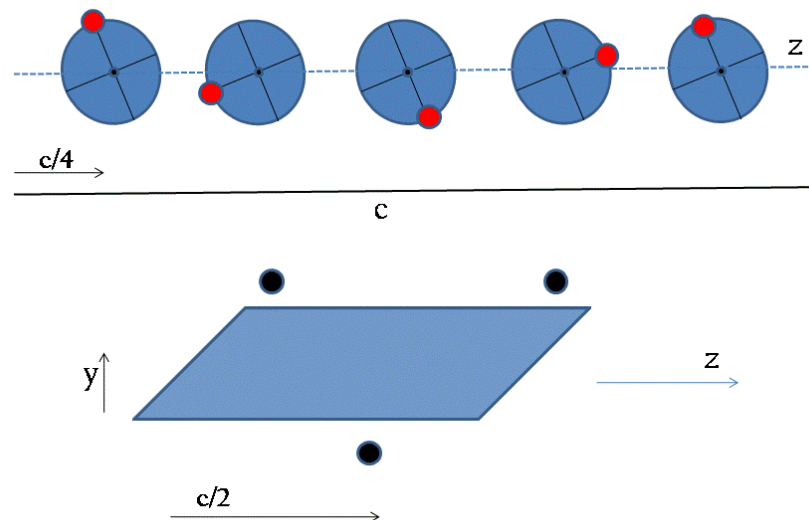
Figure 2.21 Translational symmetry operations: 4_1 *screw axis* (a) and *c glide plane* (b). Screw 4_1 is obtained by a $2\pi/4$ rotation around z axis, combined with a c/4 sliding along z axis. Glide plane c means a reflection perpendicular to y axis with a c/2 sliding along z axis.

Within the unit cell, the collection of symmetry elements constitutes a point group. Only 32 point groups are possible, which constitute 32 crystal classes. In three-dimensional space, all crystals can be assigned to one of them. If we combine the 32 crystal classes with the 14 Bravais lattices, we get 230 three-dimensional space groups. A space group can be also viewed as the combination of the symmetry operations of the point group plus translational symmetry operations. Crystal structures can only adopt these 230 distinctive space-filling arrangements. The *International Tables of Crystallography* reports a list of all of them.

The periodic arrangement of atoms in a crystal form planes passing through the lattice points and oriented in different directions. All of the planes oriented in a certain direction are parallel and separated from each other by a distance *d*, which depends on the nature of the material.

If a line is drawn parallel to the faces such that the intercepts on the unit cell edges are *a/h*, *b/k*, *c/l*; where *h*, *k* and *l* are integers, these integers are referred to as Miller indices which are used to refer to the faces and the planes within a crystal and they uniquely depend on the unit cell.

Diffraction and Bragg's law. Techniques to study crystals are based upon *diffraction* phenomena with radiation of wavelength of the order of 0.5-3.0 Å (roughly the range of interatomic nearest-neighbor distances). The following description focuses on X-rays[8], but same theory and

considerations apply to the case of neutrons (or electrons, however this is not discussed in this thesis).

In the Bragg approach to diffraction, crystals are considered to be built up in layers or planes where each of them can be regarded as a semi-transparent mirror. In Fig. 2.22, the array of blue circles represents a section through a crystal. They form a set of parallel planes with Miller indices *hkl* and interplanar spacing d_{hkl}. Two X-ray beams (1 and 2) are reflected from adjacent planes within the crystal, generating the reflected beams 1' and 2'. To see when 1' and 2' are in phase, we should consider that the beam 22' has to travel the extra distance *xyz* as compared to beam 11', and for beam 1' and 2' to be in phase, the distance *xyz* must equal a whole number of wavelengths. The perpendicular distance between pairs of adjacent planes, the d-spacing *d* and the angle of incidence, or Bragg angle θ, are related to the distance *xy* as described in Equation 2.15:

$$xy = yz = d \sin \theta \qquad \text{Eq. 2.15}$$

Thus:

$$xyz = 2d \sin \theta \qquad \text{Eq. 2.16}$$

But, from Fig. 2.22:

$$xyz = n\lambda \qquad \text{Eq. 2.17}$$

And therefore, Eq. 2.18 can be derived:

---

[8] This choice is merely due to historical reasons: Bragg father and son derived the Bragg's law in 1913 and in 1914 the first atomic-resolution structure was determined ("rock salt" structure, NaCl), while first neutron experiment on crystals was performed in 1946 by Shull and Wollan.

$$2d \sin \theta = n\lambda \qquad\qquad\text{Eq. 2.18}$$
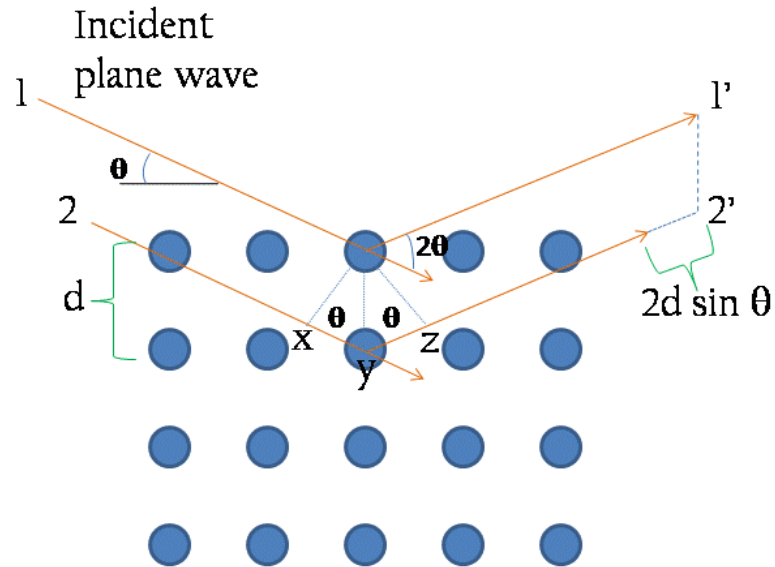
Figure 2.22 The Bragg condition for the reflection of X-rays by a crystal. X-ray crystallography relies on the fact that the distances between atoms in crystals are of the same order of magnitude as the wavelength of X-rays (1 Å). Hence a crystal acts as a three-dimensional diffraction grating to a beam of X-rays. The resulting diffraction pattern can be interpreted to give an insight into the crystal structure of the sample produced.

Equation 2.18 is known as Bragg's law and it relates the d-spacing, d_{hkl}, to the particular Bragg angle θ at which reflections from these planes are observed. When n=1, the reflections are called first order, when n=2 the reflections are second order and so on. However, the Bragg equation for a second order reflection from a set of planes *hkl* is

$$2\lambda = 2 \sin \theta_{hkl}\, d \qquad\qquad\text{Eq.2.19}$$

Which can be rewritten as:

$$\lambda = 2\frac{\sin \theta_{hkl} d}{2} \qquad\qquad\text{Eq. 2.20}$$

Equation 2.20 represents a first order reflection from a set of planes with interplanar spacing *2h 2k 2l*. Therefore, the second order reflection from *hkl* is indistinguishable from the first order reflection from *2h 2k 2l*, and the Bragg equation can be rewritten simply as

$$\lambda = 2 \sin \theta_{hkl} \, d \qquad\qquad \text{Eq.2.21}$$

2.3.2 Neutron Scattering and Powder Neutron Diffraction

Basic properties of the neutron. The neutron is a subatomic particle with the following properties:

- Zero charge (q=0), which makes it an effective and non-invasive probe of bulk samples due to its large penetration power. Therefore, it is suitable for "severe" sample environment (for example, in the case of sample holder with thick walls). The scattering cross section does vary over the periodic table of elements "arbitrarily" without any strong correlation to the atomic mass (as being independent of the electron shell). For some nuclides, the scattering is large. An important example is the lightest element hydrogen which is virtually transparent to X-rays but which scatters neutrons strongly;

- A mass of 1.675×10^{-27} kg, which results in a de Broglie wavelength of the order of inter-atomic and inter-molecular distances[9] ($\lambda_{dB}= h/mv$

---

[9] For example, at T=293 K and since $E_c = \tfrac{1}{2} mv^2 \approx k_B T$, we have the neutron wavelength: $\lambda_{dB} = h/mv \approx 1.8 \, \text{Å}$.

where h is the Plank constant equal to 6.626×10^{-34} J s). Therefore, neutrons are suitable for studying the atomic structure of condensed matter in diffraction studies. And we can also profit of sensitivity from the sensitivity of the neutrons to light atoms and isotopic substitution;

- A magnetic dipole moment (μ_n) equal to -1.913 μ_N (where μ_N is the nuclear *magneton* = 5.051×10^{-27} J T^{-1}), which is used for investigating microscopically the magnetic structure and magnetic fluctuations in materials;

- A spin (s) equal to $\frac{1}{2}$ - therefore, the neutron can be used for studying the arrangement of the nuclear spin orientation and it is suitable for both *coherent* and *incoherent* scattering experiments;

The energies of *thermal* neutrons are around 25 meV (1 eV=1.6×10^{-19} J), which are similar to the energies of many excitations present in solids and liquids. Thermal neutrons are usually obtained by slowing down energetic neutrons, produced in nuclear reactors, with a *moderator*. In the high flux reactor at the ILL, the heavy water in the moderator-reflector vessel, surrounding the fuel element, acts as moderator. After several collisions with the deuterium nuclei, the neutrons are in thermal equilibrium with the heavy water (slightly above room temperature thanks to a consequent pumping rate evacuating the heat of the 50 MW thermal power reactor). Heavy water, despite its difficulties (higher price, need of strict sealing, transmutation of deuterium to radioactive tritium) has been preferred over

light water, as the latter absorbs more neutrons, and as it moderates a little bit less quickly, bringing the maximum of thermal neutron flux further away from the outside of the fuel element (about 30 cm). The latter has two main advantages: it allows a tangential arrangement of evacuated aluminum- or zirkalloy-beamtubes (relatively transparent to neutrons) that lead in a straight line of sight neutrons to the instruments (i.e., the instrument has thus no direct sight on the reactor core with all its gamma and fast neutron radiation perturbing measurements and raising safety issues), and it allows the installation of so-called "cold" (or "hot") sources in the region of maximum flux, which would not be feasible too close to the reactor core. A vessel containing 25 liters of liquid deuterium acts as a cold moderating source, providing a velocity distribution with $T \approx 25$ K, thus "cold" neutrons of longer wavelength and less energy, and a block of hot graphite of about half this volume provides a distribution with a $T \approx$ 2000 K), thus, "hot" neutrons of shorter wavelength and more energy.

Scattering geometry and definition of scattering cross-section. Consider a beam of thermal neutron incident on a target (i.e., the sample), so that every neutron has the same energy E_0, wavelength λ_0 and wave-vector $k = 2\pi / \lambda$ (Fig.2.23):
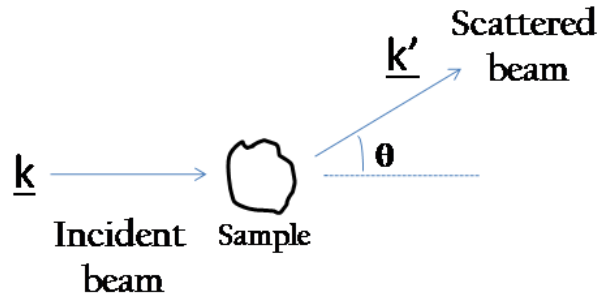
Figure 2.23 A beam of thermal neutrons incident on a sample.

Various types of measurement can be made on the neutrons after they have interacted with the sample. The result, in each case, can be expressed in terms of a quantity known as a *scattering cross-section,* defined as $d\Omega$ in Fig. 2.24.
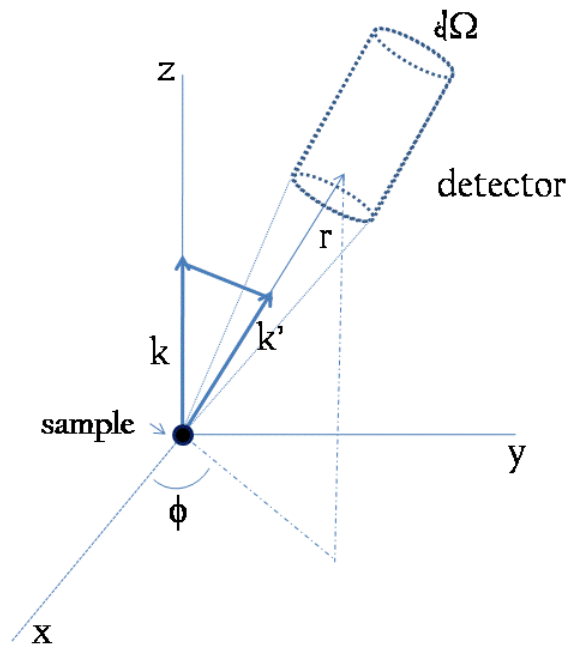
Figure 2.24 Scattering process of a neutron beam by a sample is described in terms of polar coordinates.

A neutron counter (detector) able to measure the number of neutrons scattered in a given direction as a function of their energy $E`$ is set-up. If the distance of the counter from the target is assumed to be large compared to the dimensions of the counter and the target, then the small angle $d\Omega$ is well defined. To specify the geometry of the scattering process, polar coordinates will be used, taking the direction of the incident neutrons as the polar axis. The direction of the scattered neutrons will be θ, ϕ.

Then the *partial differential cross-section*, $\dfrac{d^2\sigma}{d\Omega dE'}$, can be introduced, defined by the number of neutrons scattered per seconds into a small solid angle $d\Omega$ centered around the $k`$ direction in the direction $\theta, \phi$, with final energy between $E`$ and $E`+dE`$ over $\Phi d\Omega dE'$ (where Φ is the flux of the incident neutrons per unit area - area perpendicular to the direction of the neutron beam - and per unit time [area^{-1} time^{-1}]). The dimension of the cross-section is an area, given usually in the unit "barn": 1 barn = 10^{-24} cm^2.

As the counter cannot perform energy analysis (but only the number of neutrons scattered per second into the solid angle $d\Omega$ in the direction θ, ϕ) the cross-section corresponding to these measurements, known as the *differential scattering cross-section*, is defined by the following equation:

$$\frac{d\sigma}{d\Omega} = \int_0^\infty \left(\frac{d^2\sigma}{d\Omega dE'} \right) dE' \qquad \text{Eq. 2.22}$$

When all the neutrons scattered per unit time are detected, the total scattering cross-section is defined as:

$$\sigma_{tot} = \int_{alldirections} \left(\frac{d\sigma}{d\Omega} \right) d\Omega \qquad \text{Eq. 2.23}$$

The cross-sections are the quantities measured in a scattering experiment [19].

The energy of thermal neutrons is not high enough to cause any change of the internal energy of the nucleus. Nevertheless, the scattering is not only elastic, as collective vibration motion modes (i.e., phonons) can be triggered. In many cases, though, one considers the scattering as purely elastic when it comes to diffraction studies of static (time-averaged) crystal structure without this approximation having a significant impact on the structural result.

The scattering length. The diffraction theory assures that when waves of any kind are scattered by objects whose linear size is smaller than the wavelength λ, then the scattered waves are spherically symmetric (i.e., their amplitude depends only on the modulus $|r|$).

For a neutron coming along z, a plane wave is obtained:

$$\psi_{inc} = Ae^{ikz} \qquad \text{Eq. 2.24}$$

For a scattered neutron we use a spherical wave, such as:

$$\psi_{SC} = -A\left(\frac{b}{r}\right)e^{ik'r} \qquad \text{Eq.2.25}$$

The constant *b* is experimentally determined and it is defined as the *scattering length*. It is dependent on the particular nucleus. It is a length and usually given in femto-meters (thus, roughly the "size" of a nucleus): 1 fm=10^{-15} m.

In Eq 2.25, the sign '-' is arbitrary and corresponds to a positive value of *b* for a repulsive potential. Isotopes of the same element can be different in sign and value of *b*: hydrogen atom (to 99.99% the isotope ^{1}H, the proton) is one of those rare elements for which *b* is negative (*b* = -3.7390), while for its isotope deuterium (^{2}H) it is positive (*b* = 6.671).
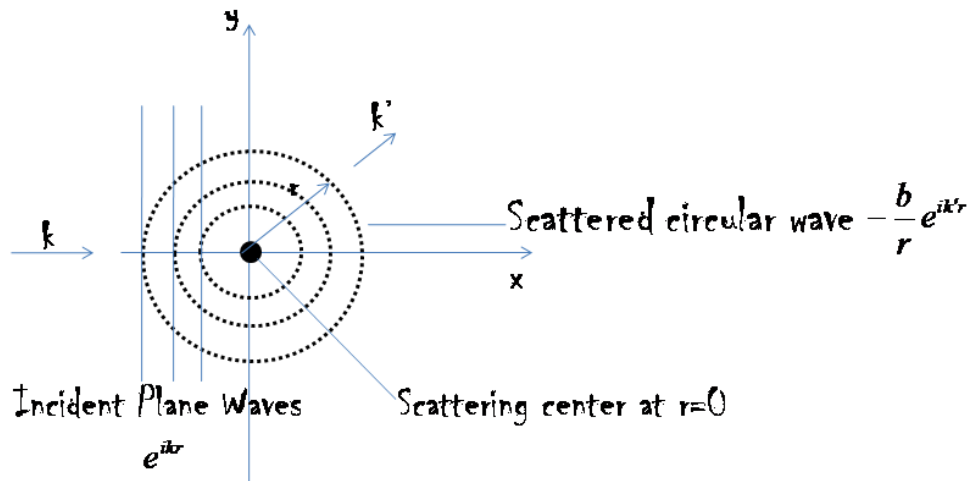
Figure 2.25 A spherical wave is used for describing a scattered neutron. b is the scattering length, experimentally determined, characteristic of the nucleus (Picture adapted from "Neutron Diffraction and Reflectometry", SISN Summer School 2012 - notes).

Two different kinds of nuclei exist:

i) Nuclei with complex b and strongly dependent on the incident neutron energy. In this case, the scattering is resonant and associated with the formation of a *compound nucleus* (namely, the original one plus the neutron) with an energy close to the one of the excited state.

The imaginary part of the scattering length is caused by absorption: these nuclei absorb neutrons strongly (e.g., ^{10}B, ^{113}Cd, ^{155}Gd and ^{157}Gd).

ii) Nuclei with a negligibly small imaginary part of b, and b independent on the neutron energy (in the energy range of neutrons used for scattering experiments). Most nuclei are of this type.

The value of b depends on the specific nucleus and on the spin of the nucleus-neutron system.

D20

The 2-axis diffractometer D20 is capable to follow ultrafast reactions over second timescales. It is equipped with a 1536 cell linear-curved PSD with a definition of 0.1° in 2θ per cell, enabling extremely rapid count rates with a neutron flux of up to 10^8 n/cm^{2}sec^{-1}, at the sample position [20]. Fig. 2.24 shows a schematic representation of D20.

In the frame of this study we used out of a choice of four different monochromators the variably vertically focusing germanium monochromator for higher take-off angles and thus higher resolution. It is composed of eleven mosaic crystal blades cut in the crystallographic orientation (113). In total, the monochromator arrangement is 6 cm wide

and 30 cm high. The blades above and below the central one can be inclined collectively to provide optimum vertical focusing of the incident neutron beam on the height of the 3.2 m distant sample of up to 50 mm height. The resulting higher vertical divergence has hardly any impact on the resolution of the diffraction pattern and is thus common practice in neutron powder diffraction, where one has to face a relatively low intensity as compared to modern synchrotron X-ray sources. Through rotation of the monochromator out of the mirror symmetry position, one can access further Bragg reflections obeying (hhl) with h and l impair or h and l even and the sum of h+h+l being a multiple of 4 (e.g., (224), but not (112), (113), but not (226)). In our measurement configuration, the monochromator take-off angle was set to $2\theta = 90°$, providing us a wavelength of $\lambda = 1.54$ Å when using the reflection (115) with a flux at the sample position of about 10^7 n cm^{-2} s^{-1}.

The precedent on using D20 for reactions of this type has been created by the pioneering work of Kisi *et al.,* who demonstrated that *self-propagating high-temperature synthesis* (SHS) could be followed over seconds with 300-millisecond collection of diffraction profiles suitable for kinetic analysis and, potentially, structure refinement [21-25].
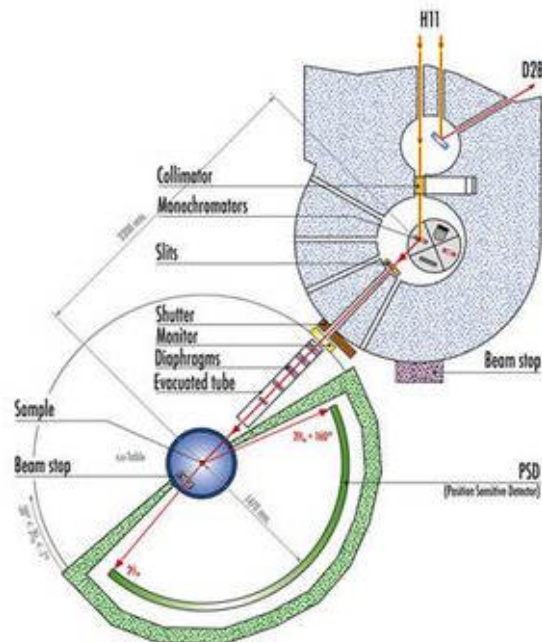
Figure 2.26 Schematic of 2-axis diffractometer D20, at the ILL (Picture from: http://www.ill.eu/instruments-support/instrumentsgroups/instruments/d20/description/instrument-layout/).

A sample prepared as described above (Section 2.2, Paragraph 2.2.2), 1 cm thickness and 10 mm diameter was used for all the samples described in this work. The pellet was positioned into an open quartz tube (10mm inner diameter). In all the cases, pellets were embedded in graphite, acting as MW susceptor. Acquisition times for a single diffractogram were in the range eight-twelve seconds, and different take off angles and wavelengths were tested. The best working set-up was found to be with a 90° take off angle and λ=1.56Å.

2.3.3 Powder X-ray Diffraction

Powder X-ray diffraction (PXD) is a rapid and accurate method to identify the crystalline phases – as well as atomic positions precisely - present in a

sample with relatively small amount of sample needed (ranging between 5 - 50 mg). This technique can be very useful in the case of carbides, where it is difficult to grow single crystals, due to their high melting point and high hardness.

In a powder X-ray diffractometer, electrons are emitted by a filament, usually tungsten, and accelerated by a high potential difference (20 - 50 kV) to strike the anode (water cooled), which emits sharp and intense X-ray peaks (K_α, K_β) superimposed to a continuous spectrum of white X-radiation. K_α and K_β have frequencies characteristic of the metal used as an anode. They depend on the difference of energy between the electron ejected from the innermost K shell ($n=1$) by the bombarding electrons, and the electron from outer shells to fill this vacancy. Electrons descending from the L shell ($n=2$) give K_α lines and electrons from the M shell ($n=3$) give the K_β lines. The target metals most commonly used in X-ray crystallography are copper (Cu) and molybdenum (Mo), chosen because their wavelengths are close to the interatomic distances of crystals (K_α lines at 1.5418 Å for Cu and K_α lines at 0.7107 Å for Mo).

Monochromatic radiation is often used, produced by filtering the K_β line by using a thin metal foil of the previous element (Z-1) in the Periodic Table as filter; (for example, nickel (Ni) filters out the K_β line of Cu, while niobium (Nb) is used for Mo). Otherwise a single crystal, usually graphite,

can be used to select a monochromatic beam of X-rays by reflecting the white radiation off a graphitic plane.

Powder X-ray diffraction sample preparation. Samples were prepared as described in Paragraph 2.2. When using a flat plate in Bragg-Brentano reflection configuration (see following section), part of the powder was then spread uniformly over a glass sample holder (18 mm × 0.8 mm), assuring a flattened upper surface using a glass slide. This is important for preventing displacement errors in the X-ray beam that happen if the sample sits above the surface of the slide.

Powder X-ray diffraction data collection and analysis. In the Bragg-Brentano geometry, the flat plate sample is irradiated using a stationary source and a moving detector to measure the intensity of the diffracted X-rays (Fig. 2.27). In particular, the detector is mounted on a moving arm, activated by a stepper motor, while a second stepper motor – synchronized with the first one – moves the sample at a half of the speed of the detector. This assures that, when the detector is tilted at an angle 2θ, the sample is tilted at an angle θ and the perpendicular of the sample is always the bisector of the incident and the diffracted beam. In this geometry, the lattice planes measured are the ones parallel to the sample surface. The X-rays penetrate to a certain depth into the sample, where they are diffracted. The Bragg-Brentano geometry is a type of reflection configuration where the source and detector of X-rays are positioned at the same angle with respect to the sample.
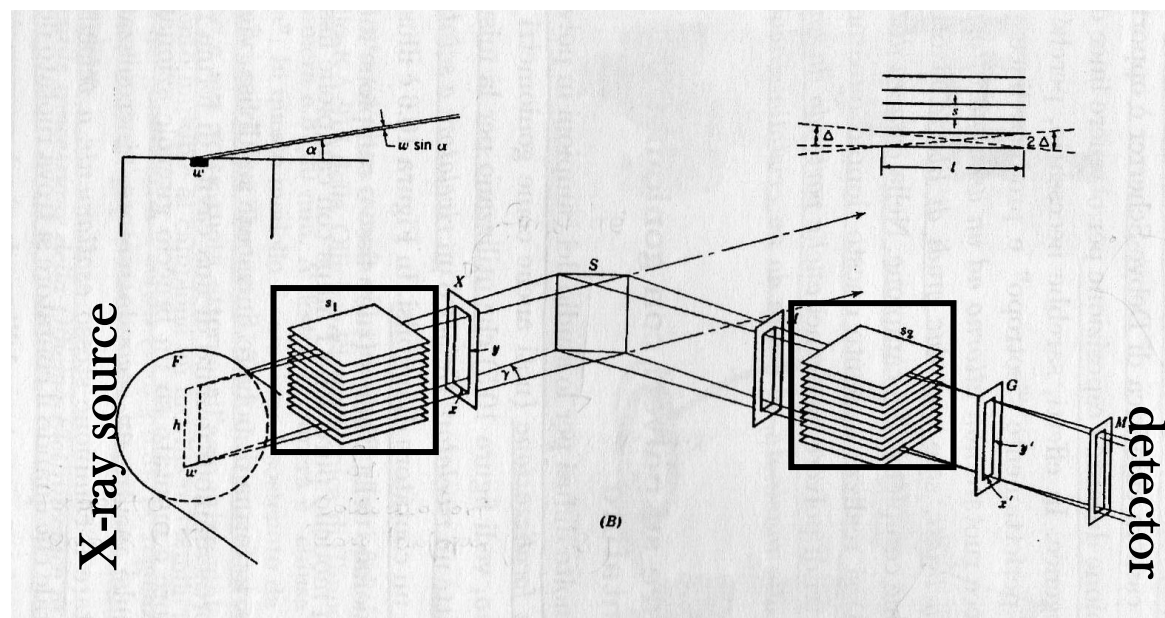
Figure 2.27 Bragg-Brentano geometry. Sample holder is in position "S". In black, collimators (Picture taken from:[5]).

The XRD measurements were performed using an X'Pert PRO MPD diffractometer, configured with Cu K_α radiation X-ray source and an X'Celerator solid-state detector. The standard operating power for the X-ray tube was 40 kV and 40 mA. Collimation of the X-ray beam was made

96

through a 10 mm beam mask, 0.04 rad Soller slits, 1/2° divergence slit and a 1/2° anti-scatter slit for a standard run, in order to prevent both horizontal and vertical divergence of the X-ray beam. Two types of scan were run, a standard 1 h phase identification scan or a 12 h overnight scan to have better data that could be used for structural refinement. The standard scan was run between 5° and 85° 2θ, step size of 0.0167° 2θ whereas the overnight scan was run between 10° and 120° 2θ, step size of 0.0167° 2θ and time per step 1120.14 s step^{-1}.

2.3.4 Rietveld refinement and Sequential refinement strategy

Neutron and X-Ray diffraction of powder samples give a pattern characterised by reflections (peaks in intensity) at certain positions. The Rietveld refinement [26, 27] uses the height, width and position of these reflections to extract detailed crystal structure information. This method also allows phase fractions in multi-phase mixtures to be determined quantitatively, from powder diffraction data. It makes use of fundamental analytical profile functions and a least-squares approach to refine a theoretical line profile until it matches the experimental scan [28].

For a Rietveld refinement, it is essential that the powder diffraction data is collected appropriately. Geometry of the diffractometer, quality of the instrument alignment and calibration, the radiation used (e.g. conventional X-ray, synchrotron X-ray or neutron), the wavelength, appropriate sample preparation and thickness, slit sizes, and necessary counting time are

factors that must be well known before refinement. Also, if the relative intensities and/or the 2θ values (and thus the d-spacings) are not correct, the structure refinement will be always affected by errors [29].

Structural refinement starts by using a trial structure as starting model, in case the structure to refine is only slightly different. When the structural model is very crude, it is advisable to analyse first the pattern with the so-called profile matching method without structural information in order to determine accurately the profile shape function, background and cell parameters before running the Rietveld method in a strict sense.

A powder diffraction profile must be calculated and compared with the experimental profile. The starting structure can then be gradually modified and refined by simultaneously changing parameters in the model. The final target is to achieve the best fit with the entire experimental powder diffraction pattern.

The parameters that the user can refine are divided into two groups:

I) Structural parameters, which describe the contents of the unit cell, including the atomic temperature factors, co-ordinates and occupancies of each atom;

II) profile parameters, which in turn could be divided into two further subgroups:

- instrumental parameters (resolution function, peak shape, wavelength, zero-shift);
- sample-dependant parameters (peak-broadening, unit cell metrics).

The refinement process is a least squares approach, during which the function M is minimised:

$$M = \sum_i w_i (y_i^{obs} - y_i^{calc})^2$$

Eq. 2.26

Here w_i is a weighting factor given by $1/y_i^{obs}$, y_i^{obs} are the observed intensity at each step/point i, and y_i^{calc} is the calculated intensity at each ith step.

The calculated intensities y_i^{calc} are obtained from the $|F_K|^2$ values, calculated from the structural model, summing the calculated contributions from Bragg reflections within a specified range k with the background, b_i:

$$y_i^{calc} = s \sum_k L_k |F_K|^2 \phi(2\theta_i - 2\theta_k) P_k A + y_{bi}$$

Eq. 2.27

where s is the scale factor, L_k contains Lorentz polarisation and multiplicity factors, ϕ is a reflection profile function, F_k is the structure factor for the kth Bragg reflection, P_k is the preferred orientation function, A is an absorption factor and y_{bi} is the background intensity at ith step.

From Equation 2.27, the relationships between the variable parameters and the intensities are not linear. This is why the starting model must be as close as possible to the correct one, otherwise the non-linear least squares procedure will either diverge or lead to a false minimum instead of the global minimum. Other considerations from Eq. 2.27:

• ϕ, the reflection profile function approximates the effects of both instrumental features and possible specimen features such as aberrations due to absorption, specimen displacement and specimen-caused broadening of the reflection profiles.

• *A*, the effective absorption factor, differs with instrument geometry. It is usually taken to be constant for the Bragg-Brentano geometry, the most commonly used.

• y_{bi}, the background intensity, can be obtained in different ways: from an operator supplied table of background intensities; linear interpolation between operator selected points in the pattern; or a specific background function. (When a background function is used, then y_{bi} is generally a cosine Fourier series with a leading constant term:

$$y_{bi} = B_l + \sum_{j=2}^{N} B_j \cos \left[P*(j-1) \right] \qquad \text{Eq. 2.28}$$

Different packages for Rietveld refinement are available. In this thesis, both neutron and X-ray patterns were analysed by using the program Fullprof [30]. In particular, in the case of *in situ* neutron diffraction, considering the numerous diffraction patterns collected over the time, the program Fullprof can run in so-called *sequential mode*, which consists in using the resulting refined parameters from the preceding pattern as the starting parameters for the next [31].

In Fullprof, it is advisable to refine parameters in the following sequence:

1. Scale factor.

2. Zero point ($2\theta_0$) of detector, 1st (constant) background parameter and lattice constants. In case of a non-constant background, it may be wise to refine at least two (polynomial) background parameters, or fix the background using a linear (cubic spline) interpolation between a set of fixed points provided by user.

3. Refinement of atomic positions and (eventually) an overall Debye-Waller factor[10], especially for high temperature data.

4. Peak shape and asymmetry parameters.

5. Atom occupancies (if vacancies of mixed occupancies are considered).

6. Turn the overall temperature factor into individual isotropic thermal parameters.

7. Additional background parameters (if background is refined).

8. Individual anisotropic thermal parameters - if the quality of the data is good enough.

9. In case of constant wavelength neutron data, the parameters *Sycos* and/or *Sysin* to correct for instrumental or physical aberrations with a cosine or sinus angular dependence, i.e., a real – or virtual – displacement of the sample parallel or perpendicular to the incident beam (in the case of Debye-Scherrer geometry or a 2-axis neutron diffractometer).

10. Microstructural parameters: coherently scattering domain size and microstrain effects.

---

[10] The Debye-Waller factor describes the attenuation of x-ray scattering or coherent neutron scattering caused by thermal motion. It has also been called the B factor or the temperature factor.

The pseudo-Voigt function is normally used to fit the observed peak shapes. In contrast to the mathematically more meaningful Voigt function, a true correlation of Gaussian (G) and Lorentzian (L) function, is a linear combination of a Lorentzian (L) and a Gaussian (G) function, which is far easier to evaluate in a computer program, and is described as:

$$\eta L + (1-\eta)G \qquad\qquad \text{Eq. 2.29}$$

η is the mixing parameter refinable as a linear function of 2θ. The Gaussian (G) and Lorentzian (L) components of the peak are represented by the equations 2.30 and 2.31:

$$G = \frac{(4\ln 2)^{1/2}}{H_k \sqrt{\pi}} \exp(\frac{-4\ln 2(2\theta_i - 2\theta_k)^2}{H_k^2}) \qquad\qquad \text{Eq. 2.30}$$

$$L = \frac{2}{\pi H_k} 1 \left/ \left[1 + 4\frac{(2\theta_i - 2\theta_k)^2}{H_k^2} \right]\right. \qquad\qquad \text{Eq. 2.31}$$

In both Eq. 2.30 and 2.31, $2\theta_k$ is the calculated position for the kth Bragg peak corrected for the zero-point and H_k is the full-width-at-half-maximum (FWHM) of the kth Bragg reflection. H_k varies with the scattering angle $2\theta_k$ and is modelled as:

$$H_k^2 = U \tan^2\theta + V \tan\theta + W \qquad\qquad \text{Eq. 2.32}$$

Eq. 2.32 is known as Caglioti formula [32]. U, V and W are refinable parameters and depend mostly on the instrument, which rules the Gaussian components of the peak shape, the dominant contribution for medium resolution instruments, i.e. neutron diffractometers, where the instrumental contribution to half width outweights the Lorenzian contribution mostly

due to sample imperfection. One of the Lorenzian peak broadening effects, the ones caused by small particle sizes in the sample, can be quantified through the Scherrer formula.

In order to understand if the refinement is proceeding satisfactorily and/or has reached completion, reliability factors (R-factors) are reported at the end of each least squares iteration. These indices expressed in Eq. 2.33-2.36:

$$R_{profile} = R_p = 100 \left[\frac{\sum_i \left| y_i^{obs} - y_i^{calc} \right|}{\sum_i y_i^{obs}} \right]$$

Eq. 2.33

$$R_{expected} = R_{exp} = 100 \left[\frac{N - P + C}{\sum_i \omega_i (y_i^{obs})^2} \right]^{\frac{1}{2}}$$

Eq. 2.34

In Eq. 2.34, R_{exp} is defined from the statistics of the refinement, where N is the number of observations, P the number of refinable parameters, C the number of constraints and ω_i is a weighting factor. From a mathematical point of view, R$_{weighted\ profile}$ (R$_{wp}$) is the most meaningful of the R-factors because the numerator is the residual being minimized (see Eq. 2.26), making R$_{wp}$ the most appropriate to reflect the progress of the refinement:

$$R_{wp} = 100 \left[\frac{\sum_i \omega_i \left(y_i^{obs} - y_i^{obs} \right)^2}{\sum_i \omega_i \left(y_i^{obs} \right)^2} \right]^{\frac{1}{2}}$$

Eq. 2.35

Another useful indicator is the R_{Bragg} factor: it measures the agreement between the intensities calculated from the model (I_j^{calc}) and those

103

measured experimentally (I_j^{obs}) over all Bragg reflections (summation index j). Unlike $R_{profile}$, it depends only on the fit of the structural parameters (and not on the profile parameters):

$$R_{Bragg} = R_B = \frac{\sum_j \left| I_j^{obs} - I_j^{calc} \right|}{\sum_j I_j^{obs}}$$

Eq. 2.36

The final measure of the whole fit, minimised during the refinement, is the goodness of fit or chi-squared parameter and is defined as:

$$\chi^2 = \left[\frac{R_{weightedprofile}}{R_{exp}} \right]^2$$

Eq. 2.37

Therefore, for a good fit, the $R_{weighted\ profile}$ should approach the statistically expected R factor (R_{exp}). χ^2 should approach one from above but never become smaller than one, which would mean a refinement of a model to the point to fit the counting errors. If this happens it could mean that the counting error bars are overestimated.

2.3.5 Raman Spectroscopy

Raman spectroscopy is a vibrational spectroscopic technique used to observe vibrational and rotational modes in a system (*i.e.*, atom or molecule). It is non-destructive, easy to use and precise [33]. Typically, a sample is illuminated with a laser beam and when light is scattered from the sample, most photons are elastically scattered (Rayleigh scattering), which means that the scattered photons have the same energy as the

104

incident photons. Raman scattering is generally very weak and it occurs when light impinges upon a sample and polarizes the electric distribution around the nuclei, deforming the electron cloud with respect to the vibrational coordinate. This creates an unstable state called a "virtual state", a very short lived distortion of the electron cloud and the photon is quickly re-radiated. When the system relaxes, it returns to a different vibrational state. The difference in energy between the original state (E_0) and this new state (E_1) leads to a shift in the emitted photon's frequency away from the excitation wavelength. This is a different phenomenon from absorption, where the molecule is excited to a discrete energy level (for example, see IR absorption in Fig. 2.27).

If the final vibrational state of the molecule is more energetic than the initial state ($E_1 - E_0 > 0$), then the emitted photon will be shifted to a lower frequency (Stokes shift). If the final vibrational state is less energetic than the initial state ($E_1 - E_0 < 0$), the emitted photon will be shifted to a higher frequency (anti-Stokes shift). Since the virtual states are not discrete states, but are created when the laser beam causes polarization in the system analysed, the energy of these states is determined by the frequency of the light source used. Another important thing to consider is that Raman scattering does not require matching of the incident radiation to the energy difference between the ground and excited states (as it happens in IR spectroscopy).
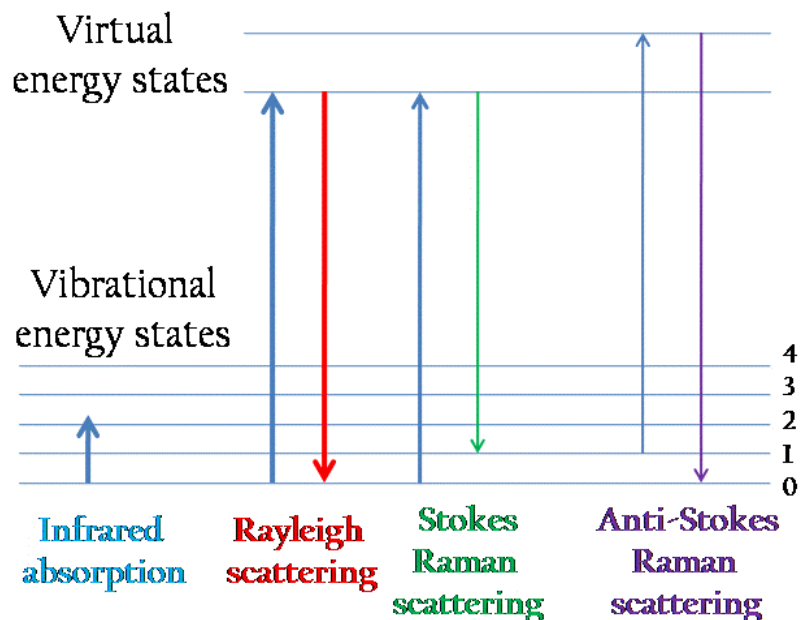
Figure 2.28 Spectroscopic transitions underlying several types of vibrational spectroscopy. The arrow line thickness is about proportional to the signal strength from the different transitions.

The population of each state can be determined using the Boltzmann equation. In the simple case at room temperature, the number of molecules expected in a vibrational state other than the ground state will be small, which means that anti-Stokes scattering will be weak if compared to Stokes scattering. Conversely, anti-Stokes scattering will increase relative to Stokes scattering as the temperature increases. Therefore, Stokes and anti-Stokes Raman peaks are symmetrically positioned about the Rayleigh peak, but their intensities are very different depending on the population of the various states of the system. The Rayleigh process does not involve any energy change and will be the most intense process, while – as said - Raman scattering is a weak process. However, modern Raman

spectrometers permit very high power densities to be delivered to very small samples.

In Raman spectroscopy, the interest is focused on the interaction between radiation (usually characterized by its wavelength (λ)) and the states of the molecule being examined. The units are expressed in wavenumbers, k, which have units of inverse length ($\Delta k = \left(\dfrac{1}{\lambda_0} - \dfrac{1}{\lambda_1} \right)$, where λ_0 is the excitation wavelength and λ_1 is the Raman spectrum wavelength) as these values vary linearly with energy (Eqs. 2.38-2.40):

$$\lambda = {c}/{\nu} \qquad\qquad \text{Eq. 2.38}$$

$$\nu = {\Delta E}/{h} \qquad\qquad \text{Eq. 2.39}$$

$$k = {\nu}/{c} = {1}/{\lambda} \qquad\qquad \text{Eq. 2.40}$$

A Raman spectrum consists of scattered intensity plotted against energy. After the sample is illuminated with a laser beam, light from the illuminated spot is collected with a lens and sent through a monochromator. Wavelengths close to the laser line, due to elastic Rayleigh scattering, are filtered out while the rest of the collected light is dispersed onto a detector. Given that spontaneous Raman scattering is typically very weak compared to the intense Rayleigh scattered laser light, instrumentation almost universally employs notch or edge filters for laser rejection. On many modern Raman spectrometers, the sample is simply presented to a microscope which is an integral part of the spectrometer.

Microscopes can be employed when using laser sources emitting in the visible region of the spectrum. This means that the scattered Raman radiation can pass efficiently through and be focussed by the glass lenses. The use of microscope has many advantages. For example, it is possible to look at extremely small samples and therefore, overcoming the fact that Raman scattering is weak, to detect very small amounts of material. When using a microscope on small samples, the beam diameter reduces very significantly and is often much smaller than the total size of the sample. The focal point will then determine which part of the sample is being analysed. This means that to have a reliable analysis of the sample, a number of measurements should be taken of different parts of the sample. Furthermore, using a microscope can discriminate against fluorescence from a sample matrix since only the chosen microscopic feature in the sample is irradiated at high power, particularly when the microscope is set up confocally. The advantages are that coupling visible laser sources to the microscope optics makes the detection system at the sensing points extremely efficient [34].

In the confocal arrangement, the laser is focussed through a pinhole, which enables only light focussed on the plane containing the sample to be collected efficiently. A plasma filter is also employed to remove any other radiation apart from the main exciting line in the laser. The radiation is then arranged to hit a notch filter. These interference filters work well when the beam is perpendicular to the plane of the filter. When coming

into contact with the filter, the laser radiation is entirely reflected into the microscope, while the scattered radiation gets transmitted, because it is at the ideal angle for the filter. Once transmitted, the scattered radiation then passes into the monochromator and onto the CCD detector.

Raman spectroscopy requires few steps for the preparation of the sample. For the analysis of samples described in this thesis, a small amount of ground powders from reacted pellets were compacted inside a small O-ring (0.5 cm in diameter) and sealed on to a glass slide. The glass slide (which did not interfere with the measurement as it scatters weakly in Raman spectroscopy) was then put under the microscope lens in the Raman spectrometer and powders were examined directly by Raman spectroscopy at room temperature. A Horiba LabRAM HR confocal microscope system with a 532 nm green laser (Laser Quantum Ventus 532, 150mW) was used. A hole aperture of 50 μm, 600 gr mm^{-1} grating and a Synapse CCD detector were used for the experiment.

Raman spectroscopy is commonly used in materials chemistry, since it provides a fingerprint to indentify the sample. Raman-active modes in fact can be found for crystals that show symmetry by using the appropriate character table for that symmetry group.

When radiation interacts with the material, it induces vibrations through the whole lattice and these can form along the direction of propagation of the radiation (longitudinal or L modes) or at right angles to it (transverse

or T modes). These bands are called *lattice modes* and can be used in Raman spectroscopy for a vast range of studies.

In the case of this thesis, only few processed pellets of MW-formed TiC were analysed by Raman spectroscopy. Stoichiometric TiC has no Raman-active vibrational modes and neither does Ti. Carbon graphite gives signals at 1320 and 1590 cm^{-1}, which are assigned to A_{1g} and E_{2g} vibrational modes, respectively [35]. In commercially available TiC, there are also 3 peaks at 260, 420 and 605 cm^{-1} (comparable with previous publications, [35, 36]). The 420 and 605 peaks are showed in Fig. 2.28(b), which are the product of two separate overlapping peaks [35]. The presence of these peaks indicates unreacted carbon in commercially available TiC.
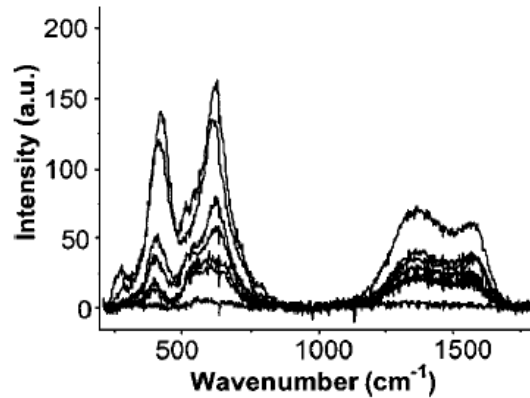
Figure 2.29 Raman spectra of commercially available TiC (as in ref:[35]).

110

2.3.6 Scanning Electron Microscopy (SEM)

Scanning electron microscopy (SEM) is a technique capable of extracting information such as composition, particle size, crystal morphology and surface defects. It makes use of an electron beam focused on the sample, which produces several types of signals:

- secondary electrons. Their emission is used to give a map of the surface topography and they come from a volume near the beam's impact area;

- backscattered electrons (BSE). Their signal is related to the atomic number Z of the elements in the sample and are capable of providing information about the distribution of different elements;

- Auger electrons (and characteristic X-rays). When an inner shell electron from an element contained in a sample is removed by the electron beam, a higher energy electron (Auger electron) fills the vacancy and gives energy in the form of characteristic X-ray radiation. This is used to give both qualitative identification and quantitative compositional information and the technique associated with this process is known as energy dispersive spectroscopy (EDS) or energy dispersive analysis of X-rays (EDAX or EDX).

- photons with various energies.

The basic components of a SEM are shown in Fig. 2.29 and comprise a lens system, an electron gun, an electron collector and visual and recording cathode ray tubes.
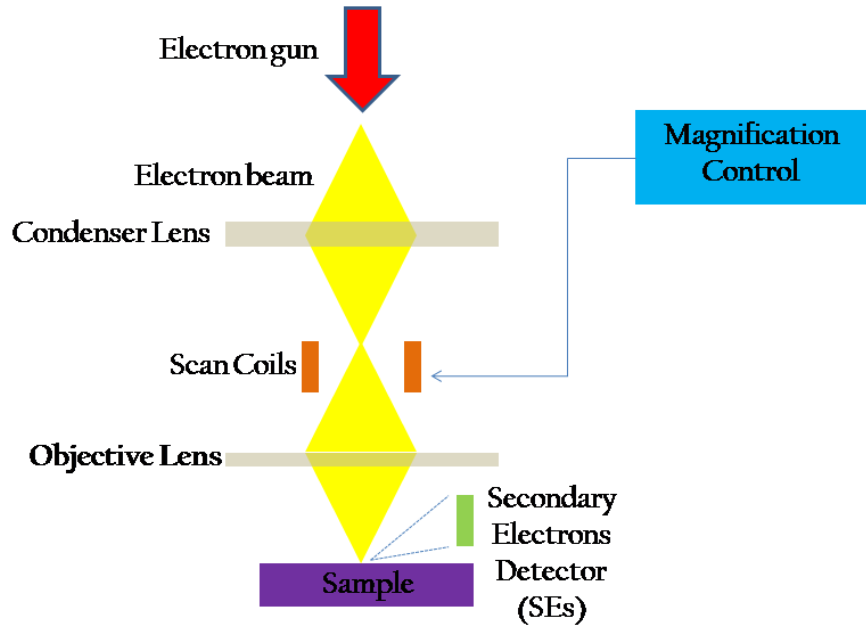
Figure 2.30 General set-up of a SEM microscope.

The electron column consists of an electron gun and two or more electron lenses, all under vacuum, where the electron gun provides a large, stable current in a small electron beam (with energy range of 1 - 40 keV) [4]. Since the beam diameter produced directly by the conventional electron gun is too large to generate a sharp image at high magnification, electron lenses are used to reduce the diameter of the electron beam and focus the beam on the specimen (magnification control).

Different detectors can be found on a SEM, depending on which signal is analysed:

- the secondary electrons, SEs, are collected by an electron detector consisting of a scintillator, a light pipe, and a photomultiplier tube, located to the side of the specimen, with the specimen usually tilted towards it (Fig. 2.29).

- Backscattered electrons (BSEs) are most efficiently and selectively collected with a detector positioned on top of the sample, which is either a semiconductor or a scintillator-photomultiplier detector.

The three major electron beam parameters define sharpness, contrast and depth of field in SEM images [4]:

• the spot size d_p, defined as the diameter of the final beam at the specimen (electron probe). This should be as small as possible to achieve the highest resolution image;

• electron-probe current i_p, defined as the current in the final probe which impinges upon the specimen and generates the various imaging signals. This should be as large as possible for the best image quality (and for X-ray microanalysis);

• the electron-probe convergence angle α_p, defined as the half-angle that the cone of electrons at the specimen makes with the centreline of the beam. It should be as small as possible in order to have a large range of heights (on the specimen) in focus at the same time.

The actual formation of a contrast image requires a scanning system to construct the image point by point across the sample surface. Two pairs of electromagnetic deflection coils (scan coils) are used to generate and control a rectangular raster of the beam on both the specimen and the viewing screen.

The electron gun is the most fundamental part of the SEM microscope. Two types of electron source are generally possible: thermionic and field

emission, which vary in the amount and stability of the emitted current, the size and the lifetime of the source. When the emitter material (the source of electrons) is heated to a high temperature, the small fraction of electrons in the highest energy state, the Fermi level, acquires enough energy to overcome the work-function energy barrier, E_w, of the material and escape into the vacuum. The cathode current density obtained from the filament in the thermionic emission is strongly affected by the temperature and the work function, E_w. Materials of low E_w are used, since it is desirable to operate the electron gun at the lowest possible temperature to reduce evaporation of the filament. The triode electron gun is the most common electron gun. It consists of a tungsten filament serving as the cathode, the grid cap, and the anode. The typical tungsten filament is a bent hairpin wire maintained at a high negative potential that is heated resistively. At the operating temperature, the tungsten wire emits electrons in all directions that are accelerated by the anode potential and a grid cap is used to focus electrons inside the gun and control the amount of electron emission. A hole in the anode allows a fraction of these electrons to continue down the column towards the lenses. Tungsten filaments, although characterized by low brightness, are commonly employed as cathodes in electron microscopy (SEM and TEM) because of advantages such as reliability, well understood properties and relative low cost. In particular for SEM applications, where high brightness is not necessary at low magnifications or where stable high currents are required, as in EDX,

the thermionic tungsten filament represents the best choice [4]. When it is essential to improve image resolution and therefore reduce the electron-probe size without causing a loss of current in the probe, increasing the electron gun brightness is required.

For the characterisation of some of the samples in this work, a Philips XL30 ESEM, working in high vacuum mode was used. An accelerating voltage of 25 kV was applied. The working distance for imaging was set at 5 mm.

References

1. Bergese, P., *Specific heat, polarization and heat conduction in microwave heating systems: A nonequilibrium thermodynamic point of view.* Acta Materalia, 2006. **54**: p. 1843-1849.
2. Gabriel, C., et al., *Dielectric parameters relevant to microwave dielectric heating.* Chemical Society Reviews, 1998. **27**: p. 213-223.
3. Clark, D.E., I. Ahmad, and R.C. Dalton, *Microwave ignition and combustion synthesis of composites.* Journal of Materials Science and Engineering A, 1991. **144**: p. 91-97.
4. Goldstein, J., et al., *Special Topics in Scanning Electron Microscopy*, in *Scanning Electron Microscopy and X-ray Microanalysis.* 2003, Springer US. p. 195-270.
5. Immirzi, A., *La diffrazione dei cristalli*, ed. L. Editore. 2002, Napoli.
6. Rao, K.J., et al., *Synthesis of Inorganic Solids Using Microwaves.* Chemical Materials, 1999. **11**: p. 882-895.
7. Thostenson, E.T. and T.-W. Chou, *Microwave processing: fundamentals and applications.* Composites: Part A, 1999. **30**: p. 1055-1071.
8. Andersson, S., et al., *Phase Analysis Studies on the Titanium-Oxygen System.* Acta Chemica Scandinavica, 1957. **11**: p. 1641-1652.
9. *"Glass". World Book Encyclopedia*, I. Chicago, Editor. 2000, World Book Inc.

10.   Meredith, R.J., *Engineers' handbook of industrial microwave heating*. 1998, London: The Institution of Electrical Engegneers.

11.   Bandyopadhyay, S., H. Dutta, and S.K. Pradhan, *XRD and HRTEM characterization of mechanosynthesized $Ti_{0.9}W_{0.1}C$ cermet.* Journal of Alloys and Compounds, 2013. **581**(0): p. 710-716.

12.   Vallance, S.R., S. Kingman, and D.H. Gregory, *Ultra-rapid processing of refractory carbides; 20 s synthesis of molybdenum carrbide, Mo_2C.* Journal of Chemical Communications, 2007: p. 742-744.

13.   Vallance, S.R., et al., *Ultrarapid Microwave Synthesis of Superconducting Refractory Carbides.* Advanced Materials, 2009. **21**: p. 4502-4504.

14.   Vallance, S.R., S. Kingman, and D.H. Gregory, *Ultrarapid materials processing: Synthesis of Tungsten Carbide on Subminute Timescale.* Advanced Materials, 2007. **19**: p. 138-142.

15.   Fukushima, H., *Rapid Heating by Single-Mode Cavity Controlled at 6GHz.* Novel Materials Processing (MAPEES'04), 2005.

16.   Vallance, S.R., *Microwave Synthesis and Mechanistic Examination of the Transition Metal Carbides*, in *School of Chemistry*. 2008, University of Nottingham.

17.   Winkler, B., et al., *In situ observation in the formation of TiC from the elements by neutron diffraction.* Journal of Alloys and Compounds, 2007. **441**: p. 374-380.

18.   Nihira, T. and T. Iwata, *Temperature Dependance of Lattice Vibrations and Analysis of the Specific Heat of Graphite.* Physical Review B, 2003. **68**: p. 134305-16.

19.   Squires, G.L., *Introduction to the theory of thermal neutron scattering*, ed. C.U. Press. 2012, Cambridge.

20.   Hansen, T.C., et al., *The D20 instrument at the ILL: a versatile high-intensity two-axis neutron diffractometer.* Journal of Measurements Science and Technology, 2008. **19**: p. 034001 (6 pp).

21.   Kisi, E.H. and D.P. Riley, *Diffraction thermometry and differential thermal analysis.* Journal of Applied Crystallography, 2002. **35**: p. 664-668.

22.   Kisi, E.H., D.P. Riley, and C.C. Curfs, *Ultra-high speed neutron diffraction studies of combustion synthesis* Physica B, 2006. **385-386**: p. 487-492.

23.   Riley, D.P. and E.H. Kisi, *The Design of Crystalline Precursors for the Synthesis of $M_{n-1}AX_n$ Phases and Their Application to Ti_3AlC_2.* Journal of American Ceramic Society, 2007. **90**(7): p. 2231-2235.

24.   Riley, D.P. and E.H. Kisi, *Self-Propagating High-Temperature Synthesis of Ti_3SiC_2: I, Ultra-High-Speed Neutron Diffraction*

Study of the Reaction Mechanism. Journal of American Ceramic Society, 2002. **85**(10): p. 2417-2424.

25. Riley, D.P., C.P. Oliver, and E.H. Kisi, *In situ neutron diffraction of titanium silicide, Ti₅Si₃, during self-propagating high-temperature synthesis (SHS).* Intermetallics, 2006. **14**: p. 33-38.

26. Rietveld, H.M., *A Profile Refinement Method for Nuclear and Magnetic Structures.* Journal of Applied Crystallography, 1969. **2**: p. 65-71.

27. Rietveld, H.M., *Line profiles of neutron powder-diffraction peaks for structure refinement.* Acta Crystallographica, 1967. **22**: p. 151-152.

28. Young, R.A., *The Rietveld Method.* 1995: Oxford University Press.

29. McCusker, L.B., et al., *Rietveld Refinement Guidelines.* Journal of Applied Crystallography, 1999. **32**: p. 36-50.

30. Rodriguez-Carvajal, J., *Recent advances in magnetic structure determination by neutron powder diffraction.* Physica B, 1993. **192**: p. 55-69.

31. Bedoya, C., et al., *Ferrolectric-paraelectric Phase Transition in PbHf02Ti0.8O3 studied by Neutron Powder Diffration.* Journal of Physics: Condensed Matter, 2001. **13**: p. 6453-6470.

32. Caglioti, G., A. Paoletti, and F.P. Ricci, *Choice of collimators for a crystal spectrometer for neutron diffraction.* Nuclear Instruments, 1958. **3**(4): p. 223-228.

33. Krishnan, R.S. and R.K. Shankar, *Raman effect: History of the discovery.* Journal of Raman Spectroscopy, 1981. **10**(1): p. 1-8.

34. Lyon, L.A., et al., *Raman Spectroscopy.* Analytical Chemistry, 1998. **70**(12): p. 341-362.

35. Lohse, B.H., A. Calka, and D. Wexler, *Raman spectroscopy as a tool to study TiC formation during controlled ball milling.* Journal of Applied Physics, 2005. **97**: p. 114912-7.

36. Klein, M.V., J.A. Holy, and W.S. Williams, *Raman scattering induced by carbon vacancies in TiCx.* Physical Review B, 1978. **17**(4): p. 1546-1556.

Chapter 3

Design and Implementation of the *in situ* Reactor.

3.1 Introduction

In this chapter, the design and implement of a novel instrumentation that permits *in situ* probing of MW-induced solid-state reactions *via* time-resolved PND techniques is described. Even though MW synthesis has been observed to reduce reaction times by several orders of magnitude compared to traditional high temperature routes [1-9], until now, limitations of *in situ* measurement techniques have meant that it has been difficult to reveal the reaction pathways and understand the mechanism of activation [10].

This part of the project - which represents the main goal of the present thesis - took about two years to be realised.

The project primarily focused on the synthesis of TiC in the bespoke reactor, extending the methodology to other binary and ternary transition metal carbides systems – namely those of the group IV, V and VI transition metals (as presented in the following Chapter 4)

The construction of the reactor consisted of two major steps:

  1) design and development of the MW reactor (Section 3.2);

2) optimisation of the remote control system for *in situ* experimentation (Section 3.3).

3.2 *Step one.* Design of MW set-up and reactor on D20.

The single mode MW reactor system used in the experiments conducted in this thesis is composed of a *Sairem* GMP20K MW generator, with a 2 kW magnetron operating at 2.45 GHz; an isolator; a quartz window; a manual variable 3-stub tuner and a power supply; a MW survey meter is added to the system to warn the operator in case of MW leakage.

The MWs are transmitted to the sample *via* the cylindrical applicator – sometimes also referred to as a reactor itself - where the sample is located and the interaction between the sample and the MWs occurs (Section 3.2.1).

A detailed description on each of these parts of the MW set-up have been extensively given in Chapter 2, paragraph 2.1.1.

For the purpose of this project, commercially available applicators suitable for MW-induced reactions showed three major disadvantages: 1) they are not implemented for D20 beam line, which has precise geometry constraints (*i.e.*, the position of the neutron beam is fixed, as well as the detector); 2) their component construction materials could give problems in terms of neutron activation (*i.e.*, brass, copper, ...)[11]; 3) their shape,

---

[11] The decay life-time, τ, of Al is ≈ 2.5 min (therefore, after about 6 τ (=15 min) the risk of contamination is below the threshold. The τ of brass and copper is significantly longer (larger than few days) which makes these materials dangerous for beam line users.

mostly rectangular, could lead to very complex diffraction patterns. In order to respond to these points, an aluminum (Al, 4 mm thickness) applicator has been designed and built *in house*. Al is, in fact, a good compromise in terms of costs and problems of neutron activation on exposure to the beam (addressing both point 1 and 2 above). Moreover, 1 mm of Al gives an attenuation of neutron beam intensity of only *ca.* 1% [11] (by comparison, 1 m of air gives the same attenuation percentage) which is acceptable for the purposes of the present experiments.[12]

Point 3 has been overcome by using a cylindrical applicator geometry, which does not contribute significantly to a neutron diffraction background, thus reducing complications in data reduction (Fig. 3.1).
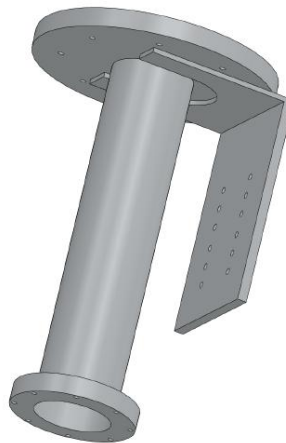
Figure 3.1. Final shape of the applicator (AutoCAD drawing): 80 mm diameter and 352 mm length. It responds to multiple problems, such as avoiding interference with both the sample and the neutron beam, fitting D20 geometry constraints and does not exhibit permanent neutron activation on exposure to the beam.

---

[12] Other possibilities could have been: TiZr, which, while does not absorb neutrons - as it is composed of two elements whose averaged scattering length (b) is ≈ 0 - on the other side it is an expensive choice; vanadium - again it does not absorb neutrons, as it is composed of two isotopes whose averaged b≈ 0, however, when heated, it oxides soon; and steel, which could be a good choice in terms of ease of manufacturing, but it includes cobalt and activated cobalt is a problem.

The choice of the length of the applicator (352 mm) was given by the fact that originally this applicator was intended to be used in vacuum as well as in air. In the vacuum case, it needed to be adapted to a vacuum vessel already in use on D20 beam line.

Regarding the applicator, simulations for predicting the evolution of the electromagnetic field inside the reactor have been performed, prior the final design of the set-up.[13]

Fig. 3.2(a) shows a simulated 3D image of the section of the system that emerges from the MW generator, isolator and tuner. Only the inner dimensions of the system are shown since the MW field does not penetrate the walls of the waveguide, so there is no need to include the thickness of the walls in the model (similarly, flanges are not explicitly shown). The incident MW radiation enters from the left hand side of the system as shown in Fig. 3.2(a) (the blue rectangular section) and propagates into the vertical section of the waveguide. A choke is also included for additional *in-situ* monitoring, such as optical pyrometry (even if in the present case a crystallographic thermometer - as explained in Section 2.1.2 - was chosen for temperature measurements, a choke was included in the simulation anyway, in case the pyrometry had to be used for quick check during optimisation of the experimental set-up).

---

[13] Those simulations have been performed at the School of Engineering, University of Glasgow, by Dr. Timothy Drysdale.

A standing wave is formed in the applicator - because it is terminated with a short circuit, *i.e.*, a metallic plate which closes the applicator at the bottom. The first electric field maximum is found ~70.3 mm above the short circuit, which is a quarter of the wavelength, (λ=281 mm, when running at 2.45 GHz frequency).

(a)

(b)
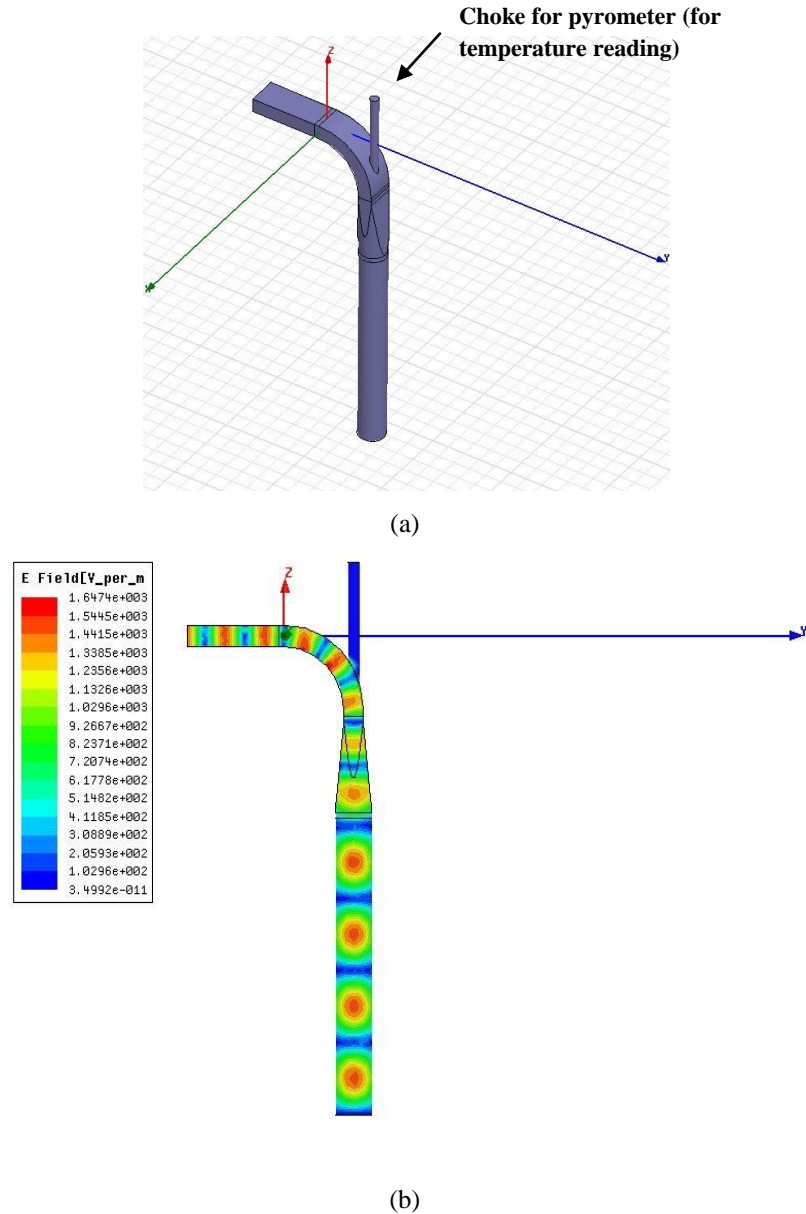
Figure 3.2 (a) 3D image of the applicator (and 90° bend waveguide); (b) Plot of the electric field magnitude. Red spots indicate the position of the maxima of the electromagnetic field inside the cylindrical reactor. These are also the positions where the maximum MW/sample coupling can be found.

122

Being a standing wave, other maxima will be periodically found in the applicator (red spots in Fig. 3.2(b)). This presents the possibility of displacing the sample within the cavity to locate another point of maximum coupling.

The guided wavelength (λ_g) for this applicator is calculated in Eq. 3.1 (assuming the lowest cutoff mode, which is TE_{11}[14], with a cutoff wavelength, $\lambda_c = 3.41 \times$(radius of the applicator)):

$$\lambda_g = \frac{\lambda_0}{\sqrt{1-\left(\frac{\lambda_0}{\lambda_c}\right)^2}} \qquad \text{Eq. 3.1}$$

where λ_0 is freespace wavelength ($\lambda_0 = c/\nu = 122$ mm – in this case).

As the radius of the applicator is 40 mm, giving $\lambda_g = 277$ mm, it would be predicted to find the first electric field maximum approximately 70 mm from the short circuit with further maxima being found periodically.

Simulations shown in Fig 3.2 were used as a starting point for the MW apparatus to be build on D20. Two trials (which are shown in Fig. 3.3 (a) and (b)) - tested during several beam times, over two years - were made before finding the working geometry (shown in Fig. 3.4).

The first attempt started from a bend configuration (Fig. 3.3(a)), in which the MWs were immediately turned horizontally through a 90° *H* bend into the isolator and the three-stub tuner and then turned again vertically through a 90° *E* bend into the rectangular-to-cylindrical transition

---

[14] As explained in Chapter 2, section 2.1, paragraph 2.1.1

waveguide. This allowed a vertical position for the cylindrical applicator, crucial to enabling easy charging the sample from the bottom of the cavity (Fig. 3.4). Moreover, such configuration facilitates the vertical motion of the sample so as to maximise the MW coupling position. In this regard, the positions of the maxima of the electromagnetic field are perturbed when a sample is placed into the applicator, depending on the dielectric properties of the sample itself. Therefore, once the reaction tube is placed into the applicator, it is possible that some MW parameters would need to be tuned and optimised until the best working conditions are satisfactorily achieved (*e.g.*, maximising forward power transferred into the sample and hence maximizing the heating).

This first configuration did not lead to the expected results, possibly due to the presence of the bend waveguides, which complicated the shape of the MW field. Therefore, the set-up has been simplified and in a second attempt (Fig. 3.3(b)), by removing the H bend waveguide and retaining the E bend (in order to leave the applicator in a vertical position).

However, again this second set-up has lead to less intense E-field strength at the sample position. In fact, no reactions were observed.

(a)
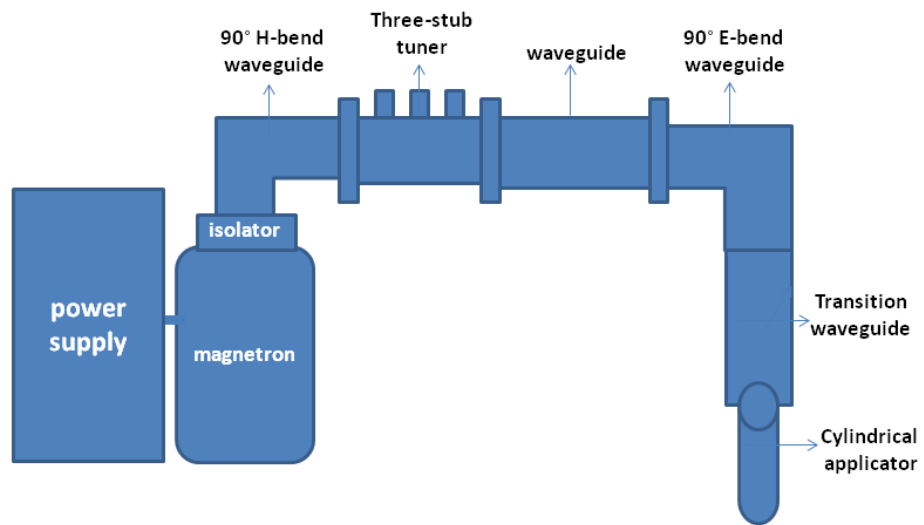
(b)
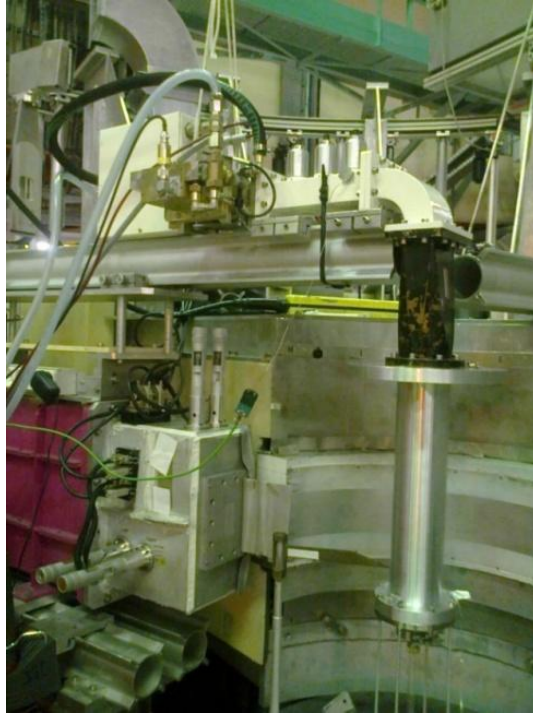
(c)

Figure 3.3. (a) First MW set-up used on D20. It shows two bend waveguides (after the isolator and before the transition waveguide). (b) Diagram of the first MW set-up. (c) Second configuration of the set-up, on D20. The first bend waveguide (after the isolator) has been removed. Both solutions were unable to transfer the necessary power into the applicator and at the sample position.

A new, straight configuration was then investigated which following

testing the final working geometry adopted (Fig 3.4).

(a)
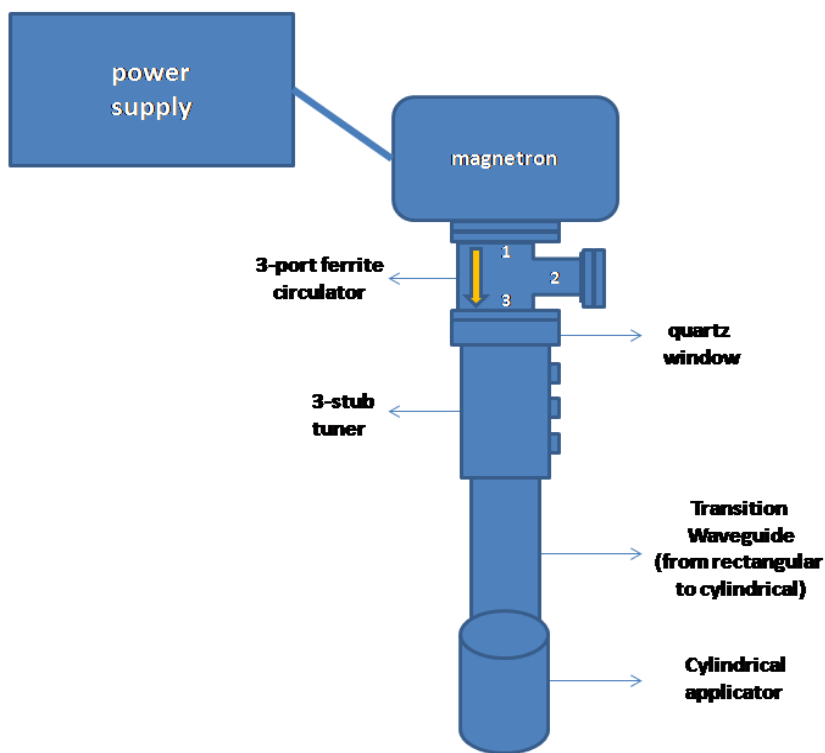
(b)

Figure 3.4. (a) Working MW set-up, mounted on D20: (1) MW generator and magnetron; (2) isolator (3-port ferrite circulator); (3) quartz window; (4) 3-stub tuner; (5) transition waveguide; (6) cylindrical applicator; (7) power supply; (8) MW survey meter. (b) Schematic of MW set-up.

All the components of the MW reactor system apart from the applicator are connected through a type WR340 waveguide with inner cross sectional dimensions of 86 × 43 mm. The cylindrical aluminum applicator (80 mm inner diameter) is connected to the other components *via* a rectangular-to-cylindrical transition waveguide. The latter component makes possible to easily adapt the rectangular shape of the MW set-up - as commercially available - to the *in house* applicator.

It is possible to easily charge the reaction tube (quartz tube+sample) from the bottom of the applicator (Fig. 3.5).
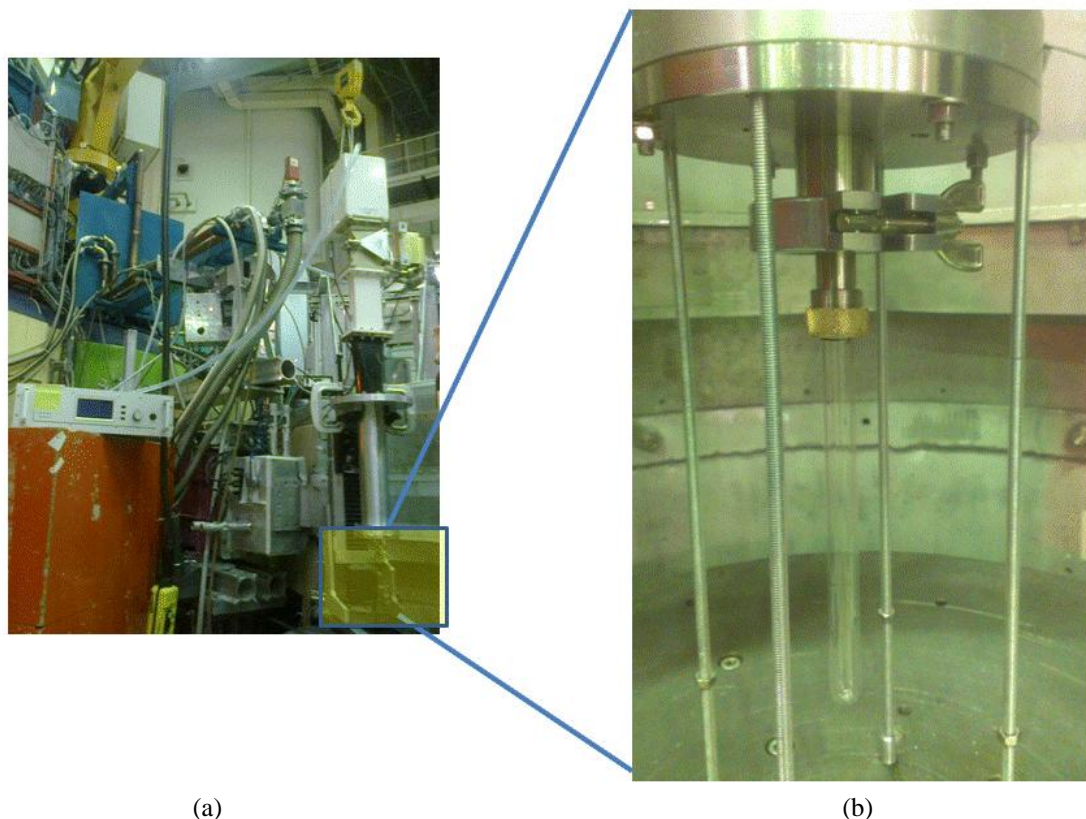
(a)   (b)

Figure 3.5. (a) MW-SMC set up mounted on the D20 beam line and a zoom of the reaction tube (highlighted in yellow); (b) reaction tube loaded into the applicator. This configuration allows manual adjustment of the position of the sample in the cavity, thus achieving the best MW/sample coupling position (namely, where the difference between FP and RP takes its maximum value).

The sample (1 g, 8 mm diameter pellet and *ca.* 1 cm thick, embedded in graphite powder susceptor) is supported by a small amount of quartz wool placed in a quartz reaction tube (12 mm diameter) which is open at the top and sealed at the bottom (Fig. 3.6). The position of the reaction tube in the applicator can be manually adjusted by the operator, by shifting the tube until the desired coupling position is found. The latter can be easily read on the display of the power generator; the best MW/sample coupling

129

position, in fact, is found when the difference between the forward (FP) and the reflected (RP) power is at its highest value – which corresponds to the maximum amount of energy absorbed by the sample, and hence maximum heating achieved at the sample position. Both FP and RP are shown in the display. By varying the nature of the sample, the first electric field maximum can shift from the theoretical value of 70 mm (deriving from Eq. 3.1).

After 1) maximizing the power absorbed by the sample, by using the 3-stub tuner until the RP is found at its minimum value and 2) centering the sample in the beam, the reaction can start. Step 2 is possible by using a microcontroller table (Fig. 3.7).
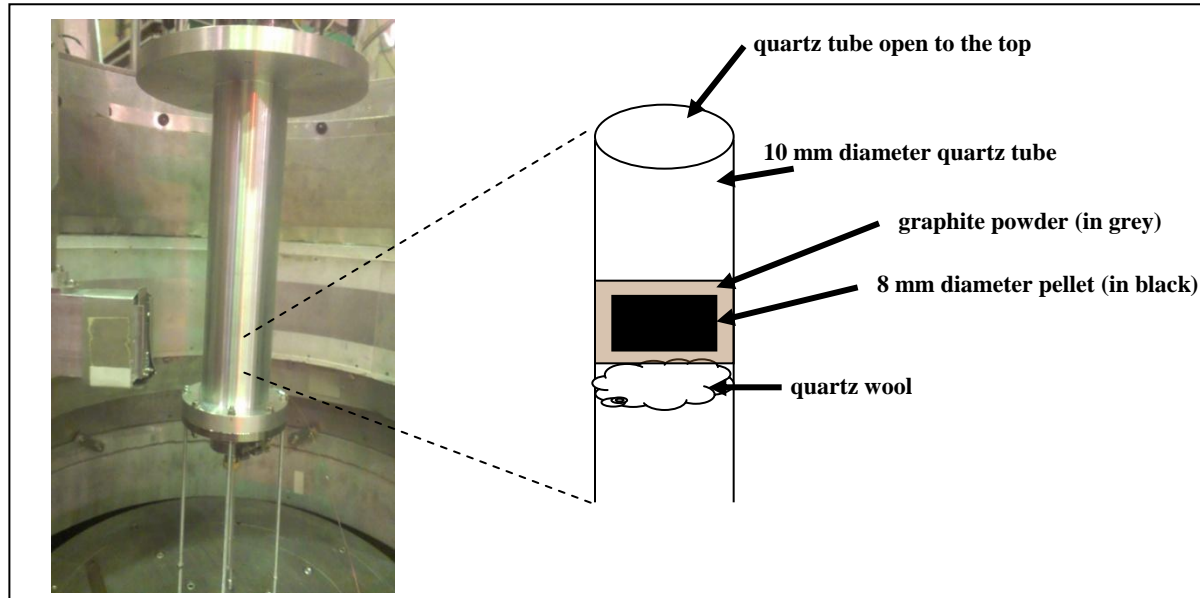
Figure 3.6. Schematic of the reaction tube (right), inside the applicator. The quartz wool is needed for supporting the pellet in the quartz tube. Quartz wool is inert for both neutrons and sample, it does not contribute significantly to the diffraction pattern and it does not burn at the temperature reached in the experiments.

Figure 3.7. (a) The microcontroller table moves the MW set-up vertically (*y*-axis – maximum run 30 cm), horizontally (*x*-axis – maximum run 30 cm) and on the detector plane (ω angle – 180° degrees), in order to allow the best centering position of the sample in the neutron beam, after the best coupling position MW/sample has been found; (b) Example of microcontroller table shifted on the ω plane by 45° in respect to the position in figure 3.7(a).

4.3 *Step two*. Remote control.

MW-promoted reactions are very fast, and over the course of a few seconds the product is already formed - as shown in Chapter 4 for the Ti-C system. In fact, once all the instrumental parameters have been optimised, it was observed that TiC appears in only 60 seconds, while intermediate phases, such as β-Ti emerge in even shorter times (40 s, *cf. sample 4* in Chapter 4). This gives the operator only a few seconds after manually setting up the MW power supply on the beam line and switching on the neutron beam to access the PC workstation outside the beam line area and starting acquisition. Therefore, it is possible that the reaction is already complete when the operator is finally ready to log data at the computer.

131

To overcome these difficulties, the function of the MW power supply was implemented so that it could be controlled remotely *via* software for use with the NOMAD server (the instrument control software used on D20). The MW power can be set up easily *via* the NOMAD interface and FP and RP can be controlled at any time. The powder neutron diffraction data collection can start even before MWs are switched on. The capabilities of the D20 detector permit diffractogram collection over the order of a few seconds, thus enabling the user to perform *in situ* heating routines (and therefore chemical reactions in the neutron beam).

References

1. Bykov, Y.V. and V.E. Semenov, *High-temperature microwave processing of materials.* Journal of Physics D: Applied Physics, 2001. **34**: p. R55-R75.
2. Cheng, J., et al., *Microwave reactive sintering to fully transparent aluminum oxynitride (ALON) ceramics.* Journal of Materials Science Letters, 2001. **20**: p. 77-79.
3. Fang, Y., et al., *Enhancing densification of zirconia-containing ceramic-matrix composites by microwave processing.* Journal of Material Science, 1997. **32**: p. 4925-4930.
4. Katz, J.D., *Microwave Sintering of Ceramics.* Annual Review of Material Science, 1992. **22**: p. 153-170.
5. Schiffman, R.F., *Commercializing Microwave Systems: Paths to success or Failure.* Ceramic Transactions, 1995. **59**: p. 7-17.
6. Agrawal, D., et al., *Microwave Processing of Ceramics, Composites and Metallic Materials*, in *Microwave Solutions for Ceramic Engineers*, D.E. Clark, et al., Editors. 2006, The American Ceramic Society: Westerville, Ohio.
7. Rao, K.J., et al., *Synthesis of Inorganic Solids Using Microwaves.* Chemical Materials, 1999. **11**: p. 882-895.
8. Menéndez, J.A., et al., *Microwave heating processes involving carbon materials.* Fuel Processing Technology, 2010. **91**: p. 1-8.
9. Michael, D., D.M.P. Mingos, and D.R. Baghurst, *Microwaves in Chemical Synthesis*, in *The New Chemistry*. 2000, Cambridge University Press.

10.   Vallance, S.R., *Microwave Synthesis and Mechanistic Examination of the Transition Metal Carbides*, in *School of Chemistry*. 2008, University of Nottingham.

11.   Pynn, R., *Neutron Scattering - A Non-desctructive Microscope for Seeing Inside Matter*, in *Neutron Scattering Applications and Techniques*.

Chapter 4

Microwave Studies in the Ti-C System

4.1 Single and Multi Mode Cavity Synthesis in the Ti-C system

Traditional syntheses as well as alternative routes for TiC production were reviewed in Chapter 1 (Section 1.4.1). Methods for producing TiC include:

- reaction of liquid magnesium and vaporized $TiCl_4+C_xCl_4$ (x=1,2) solution [1];

- combined sol-gel and MW carbothermal reduction methods [2];

- gas phase reaction of $TiCl_4$ with gaseous hydrocarbons [1];

- synthesis by thermal plasma technique [3].

TiC has also been recently produced by means of the solid state reaction from its component elementals (Ti, powder, average grain size < 43 µm and C, graphite powder, average grain size <16 µm) after 4 h at 1073 K, by Winkler and co-workers [4]. Their experience represents one of the best results obtained for TiC production *via* conventional furnace and for this reason it has been taken as a comparison for the *in situ* MW experiments performed in this thesis. It is, in fact, the first reaction of this kind probed by means of *in situ* PND, and, further, the product was obtained in relatively short time and low temperature, if compared with

previous reactions performed in conventional furnaces (*ca.* 12-24 h and 1900-2300 K).

Attempts towards MW-promoted synthesis of TiC were originally made by Ahmad *et al.* in 1991, when they processed a stoichiometric mixture of Ti and C *via* "microwave ignition and controlled combustion", MICROCOM (ignition and combustion assisted by MWs). In that experience, they used a high power industrial MMC oven (*Raytheon* 6.4 kW maximum, 2.45 GHz) used at 2.4 kW power and collected TiC after *ca.* 12 minutes [5].

Another attempt to prepare TiC using MWs was made in 1995 by Hassine *et al* [6]. This process involved the MW synthesis of TiC *via* the carbothermal reduction of TiO_2. In this case, the reaction produced $Ti(O_{0.2}C_{0.8})$ and TiC itself was not observed, which was possibly due to the quality of the Argon atmosphere in the reaction vessel.

All of these previous MW syntheses were performed without *in situ* mode characterization and therefore, very little information regarding the MW-induced reaction pathways to TiC exist in the literature.

The experimental set-up (for both MMC and SMC reactors) used in this thesis for the synthesis of Ti-C system, starting from elemental powders (Ti + C), are described in the following section (4.1.1). MMC reactions have been performed at Glasgow University (GU) noting that *state of the art* domestic MW ovens make it impossible to work directly under an X-

135

ray (or neutron) beam. SMC experiments have been performed in the laboratory (at GU) and *in situ* on the neutron beam line (D20 at the ILL). Section 4.2 (paragraph 4.2.2.3) reports the results of Rietveld refinements for *ex situ* PXD and *in situ* PND data collected for Ti-C pellets. Further characterisation of the samples by means of Raman spectroscopy and SEM is reported.

4.1.1. MW synthesis in the Ti-C system and experimental details.

Ti-C is a challenging system for MW processing. While carbon is a relatively good MW absorber ($\tan \delta$ = 0.35-0.83 [7]) able to heat up at 1000 °C in less than 2 minutes in a typical domestic microwave oven [8], titanium, on the other hand, is expected to behave as a low absorber with a $\tan \delta$ around 0.01 (Chapter 1, section 1.3).

In this thesis project, syntheses have been performed in both an MMC reactor (at GU, as described in Chapter 2, section 2.2.1), and SMC reactors (both at the GU and at the ILL – Chapter 2, section 2.2.2). An SMC reactor offers many advantages compared to a MMC. For example, while the first permits a good control of the input power - up to 1000 W for experiments in this thesis - the latter gives only fixed values of power pulsed for certain durations, as defined by the manufacturers (800 W in this thesis - see Chapter 2, section 2.1.1).

In all the cases, graphite was used as a MW susceptor.

The majority of the present work focused on the synthesis of the carbide starting from the elemental powders. All reactions were performed combining a stoichiometric amount of Ti with graphite and, in all cases, powders were pressed into cylindrical pellets (the next best geometry after a sphere, in terms of heating performance [9]) without using any binder.

In the MMC case, the pellets - mixture of titanium (-100 mesh (~149 μm) particle size, Aldrich 99.7 %) and graphite (<45 μm particle size, Aldrich 99%) in 1:1 molar ratios and typical sample total mass 1 g - were ground in a agate mortar and then cold pressed uniaxially in an 10 mm pellet die (*Specac*, 5 Tons, 5 min). The pressed pellets were embedded in the susceptor in an open, 12 mm silica tube which was surrounded with low dielectric loss silica flour (Aldrich, 99.6 %), as described in Chapter 2, section 2.2.1 (see also Fig. 2.15). This system was always positioned in the same location within the cavity to keep the experimental parameters as constant as possible. No impedance matching device was employed due to the very small sample to cavity volume ratio. All preparations were performed in air.

Ex situ phase analysis from PXD revealed the formation of the expected product, TiC (*sample 1*, Section 4.2, paragraph 4.2.1.1).

In the case of the SMC studies performed at GU, the reactor used was a *Gaerling Applied Engineering* magnetron head, 1 kW maximum power, 2.45 GHz frequency, connected through a WR430 waveguide to an E-H tuner for impedance matching purposes, while a *Sairem*® GMP20K MW

generator, 2 kW maximum power, 2.45 GHz frequency, connected through a WR340 waveguide to a manual three stub tuner was used at ILL (Chapter 2, section 2.2.2).

In the SMC, the reaction tube (quartz tube plus sample) was positioned into the cavity where the difference between the forward (FP) and the reflected (RP) power was found at its highest value – which corresponds to the maximum amount of energy absorbed by the sample, and hence maximum heating achieved at the sample position.

As in the above MMC case, elemental powders of Ti (-100 mesh particle size, Aldrich 99.7 %) and graphite (<45 μm particle size, Aldrich 99%) in 1:1 molar ratios and typical sample total mass 1 g were ground together and pressed into 8 mm diameter pellets which were set in powdered susceptor in an open, 10 mm diameter quartz tube.

Characterisation of MMC and SMC experiments performed at GU (*sample 1* and *sample 2*, respectively) have been conducted *via* PXD, Raman and SEM, while SMC experiments performed at the ILL (*sample 3* and *sample 4*) have been characterised, for the first time, by means of *in situ* PND. Further analyses on *sample 3* and *sample 4* have been carried out by means of *ex situ* Raman and SEM.

In situ PND analysis was conducted on the D20 beam line at the ILL. In our measurement configuration, the monochromator take-off angle was set to $2\theta = 90°$, providing a wavelength, λ, of 1.36 or 1.54 Å, with a flux at the sample position of about 10^8 s^{-1} cm^{-2} (Chapter 2, section 2.3.2). 10 s runs

were used, which was a good compromise in terms of diffraction resolution and our ability to identify intermediate phases over the course of the reaction.

The PXD measurements were performed using an X'Pert PRO MPD diffractometer, configured with Cu K_{α} radiation X-ray source and the X'Celerator solid-state detector. Two types of scan were run, a standard 1 h phase identification scan or a 12 h overnight scan to have better data that could be used for structural refinement (details in Chapter 2, section 2.3.3).

Raman spectroscopy was used to determine whether any amorphous phase fraction (*e.g.* of carbon) was present (Chapter 2, section 2.3.3). Raman spectra were collected at room temperature using a Horiba LabRAM HR confocal microscope system with a 532 nm green laser (Laser Quantum Ventus 532, 150 mW). A hole aperture of 50 μm, a 600 gr mm^{-1} grating and a Synapse CCD detector were used for the analyses.

The morphology and elemental composition of samples were determined by SEM. Samples for SEM of sufficient thickness were prepared by depositing powder onto a carbon tab (Chapter 2, section 2.3.4).

Gaerling set-up (GU). The reaction tube was placed directly into the cylindrical TE10n single mode cavity (Fig. 4.1). Such a cavity allows the sample to be placed in the point of highest electric field, which is not possible in a traditional MMC. The field pattern is created by the

superposition of incident and reflected waves and is achieved through careful adjustment of a short circuit beyond the applicator. Impedance matching, required to minimize reflected power was performed using a *Sairem*® automatic E-H tuner.

The cavity was excited using a *Gaerling Applied Engineering* magnetron head, operating at 2.45 GHz adjusted to produce and 1 kW of MW power, over the duration of the treatments.
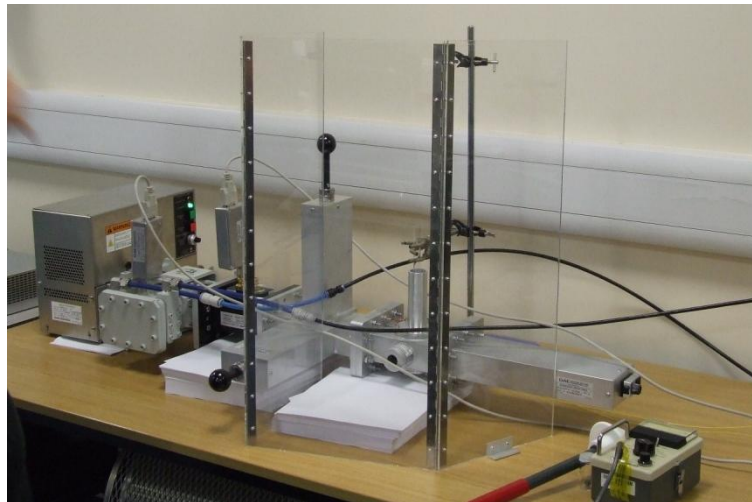
(a)
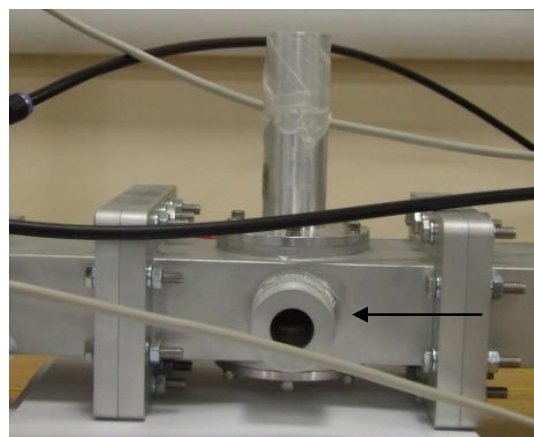
(b)
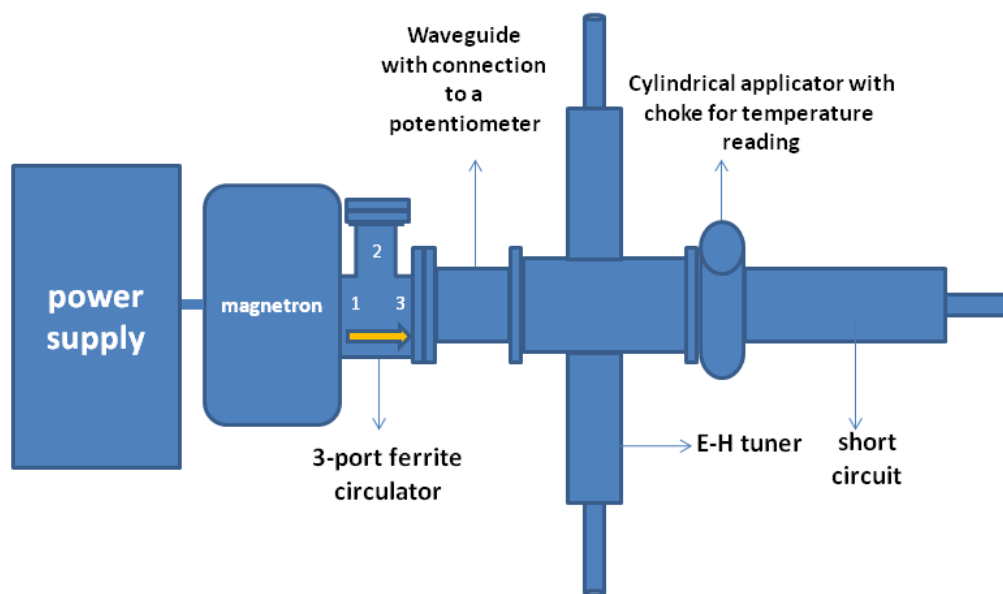
(c)

Figure 4.1 (a) *Gaerling* set-up, as used in GU for Ti-C system synthesis experiments. (b) Cylindrical TE10n SMC in the *Gaerling* set-up. The reaction tube is placed vertically in this cavity, from the (open) top. The choke (indicated by a black arrow) is used for temperature readings (*via* pyrometer). (c) Schematic of *Gaerling* set-up.

Sairem® set-up (ILL). The reaction tube was placed into a metallic plate (tube holder) and then placed into the cylindrical TE10n single mode cavity (as reported in Chapter 3, see Fig. 3.5). Impedance matching was performed using a *Sairem®* manual three stub tuner. *In-situ* temperature measurements were taken by exploiting the thermal expansion of graphite, as explained in section 4.2.2.4.

4.2 Results

Multiple reactions were tested during this thesis project. A large fraction of them led to inconclusive results. Indeed, the investigated processes

ended up to be very challenging, especially because of their short reaction time.

In the following sections, we will only describe the cases which clearly lead to the formation of the expected product, TiC, while, for the sake of conciseness, unsuccessful attempts are omitted.

Reactions 1, 2 and 4 are reproducible in both domestic and single mode MW set-up. Sample 3 was instead only partially successful (β-Ti phase was present at the end of the reaction together with the expected product TiC). This was possibly due to the position of the sample in the cavity. We nevertheless include a description of this reaction in order to show how the sample position can affect this type of reactions.

Table 4.1 summarise the experimental conditions for samples 1-4.

Sample No.	*Sample 1*	*Sample 2*	*Sample 3*	*Sample 4*
MW Instrument	Domestic MW oven (Glasgow)	Gaerling Set-up (single mode - Glasgow)	Sairem set-up (ILL, Grenoble)	Sairem set-up (ILL, Grenoble)
Size of the pellet	10 mm	10 mm	8 mm	8 mm
Mass of the pellets	1 g (Ti = 0.800 g; C = 0.200 g)	1 g (Ti = 0.800 g; C = 0.200 g)	1 g (Ti = 0.800 g; C = 0.200 g)	1 g (Ti = 0.800 g; C = 0.200 g)
MW power	0.800 kW (multi mode oven)	1 kW (single mode; Gaerling set-up)	0.500 kW (single mode; Sairem set-up)	0.500 kW(single mode; Sairem set-up)
Time of formation of TiC	10 min (*ex situ*)	10 min (*ex situ*)	100 s (*in situ*)	50 s (*in situ*)

Table 4.1 Summary of the experimental conditions for samples 1-4.

4.2.1 MMC microwave studies of Ti-C system.

4.2.1.1 *Sample 1*. **Synthesis of TiC starting from Ti + C.**

MMC synthesis of TiC was analysed by means of *ex situ* PXD and further characterised by means of Raman and SEM. Data for *sample 1* show that single phase TiC can be synthesised in air, in a domestic MW oven, after only 10 minutes.

The PXD pattern for *sample 1* is dominated by five peaks that match with the reflections from the (111), (200), (220), (311) and (222) planes of the cubic structure of titanium carbide (Fig. 4.2).
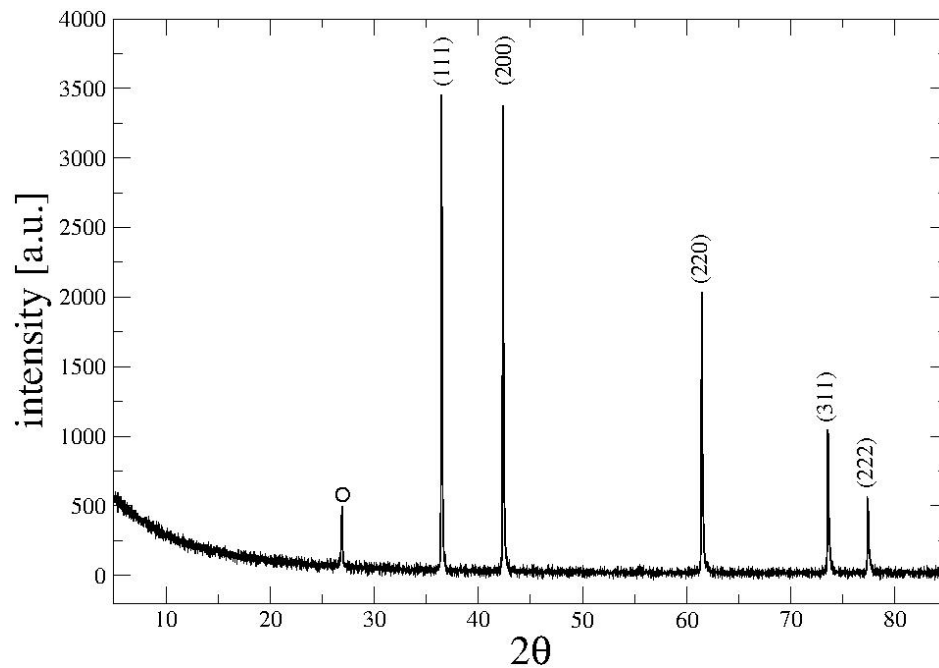
Figure 4.2 *Sample 1*. Single phase TiC after 10 min of MW irradiation in an MMC, in air. The graphite (002) peak is also indicated (○).

4.2.2 SMC microwave studies of the TiC system.

4.2.2.1 *Sample 2*. SMC synthesis using the *Gaerling* reactor.

Again in this case, the PXD pattern for *sample 2* is dominated by five peaks that match with the reflections from the (111), (200), (220), (311) and (222) planes of the cubic structure of titanium carbide (Fig. 4.3).
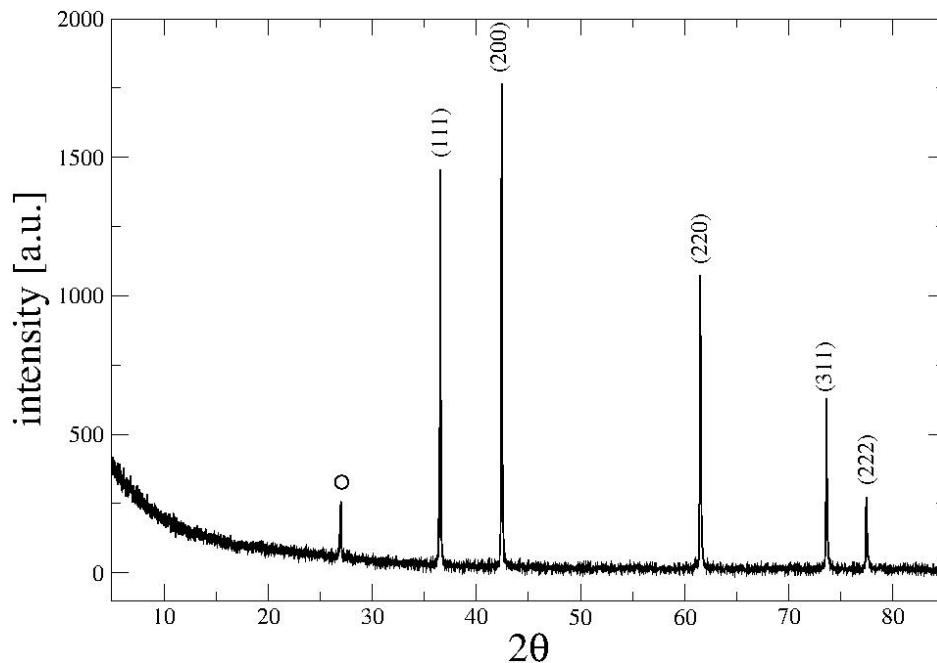
Figure 4.3 *Sample 2*. Single phase TiC after 10 min of MW irradiation in Gaerling SMC reactor, in air. The graphite (002) peak is also indicated (○).

4.2.2.2 *In situ* synthesis in *Sairem*® reactor. Two cases.

Sample 3.

Figs. 4.4 and 4.5 show the first MW synthesis performed *in situ*, on the D20 beam line. In particular, Fig. 4.4 depicts the whole reaction pattern for *sample 3*. Fig. 4.5 shows selected diffractograms collected at different times during the same reaction.

At the beginning of reaction (t = 0), only reactants (α-Ti and graphite) are present. After 10 s of MW irradiation, the temperature starts to increase and a shift of C peaks to lower 2θ angles is observed. When t = 60 s, β-Ti peaks (plus α-Ti) are detectable. TiC starts to be visible after *ca.* 100 s of reaction and α-Ti and β-Ti are still present at this point. At t = 120 s, both TiC (phase fraction: 73(6) wt%) and β-Ti (phase fraction: 27(7) wt%) are present.
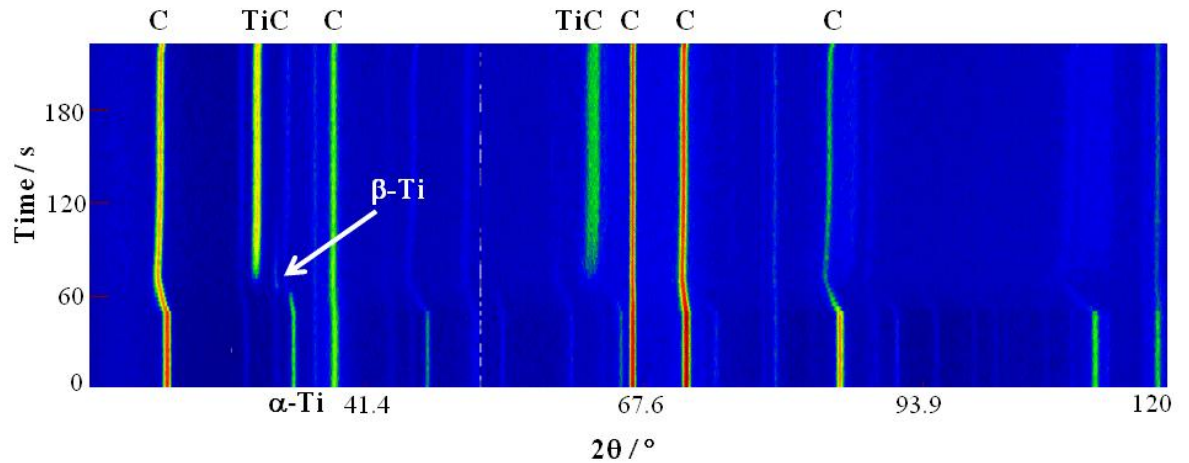
Figure 4.4 Full reaction diffraction profile for *sample 3*. The shift of the carbon peaks to lower 2θ angles (at *ca.* 50 s) is a good indicator of a rapid temperature increase. The formation of TiC (around 100 s) is revealed by new peaks appearing at *ca.* 31° and 63° 2θ. In this reaction, TiC is not formed as a pure phase, as β-Ti is always detectable and present until the end of reaction.

Fig. 4.5 shows selected diffractograms collected *in situ* on D20 (500 W MW; patterns collected every 10 s, 90° take off angle, λ = 1.36 Å), for *sample 3*. At t = 10 s, C peak shift to lower 2θ indicates increasing temperature. At t = 60 s, β-Ti (*) appears (and it co-exists with α-Ti (□)). At t = 100 s, TiC (♦) appears, together with α-Ti (5.3 wt%) and β-Ti (88.7 wt%). At t = 120 s, TiC and β-Ti are the major phases present.

145

Figure 4.5 *Sample 3.* For clarity, the diffractograms have been normalized at 0, 10, 60, 100, and 120 s by shifting their intensity and adding a constant of, respectively, 0, 500, 1000, 1500, 2000.

Sample 4.

The same experimental conditions as for the previous *sample 3* (500 W, α-Ti and graphite as starting reactants) were applied to *sample 4, except for the position of the sample inside the cavity, which was changed* (namely, the reaction tube was shifted into the cavity, achieving another position where the difference between FP and RP was found at its maximum value). The wavelength was also changed from 1.36 Å to 1.54 Å, while the take off angle remained at 90 °. The result is shown in Figs. 4.6 and 4.7.
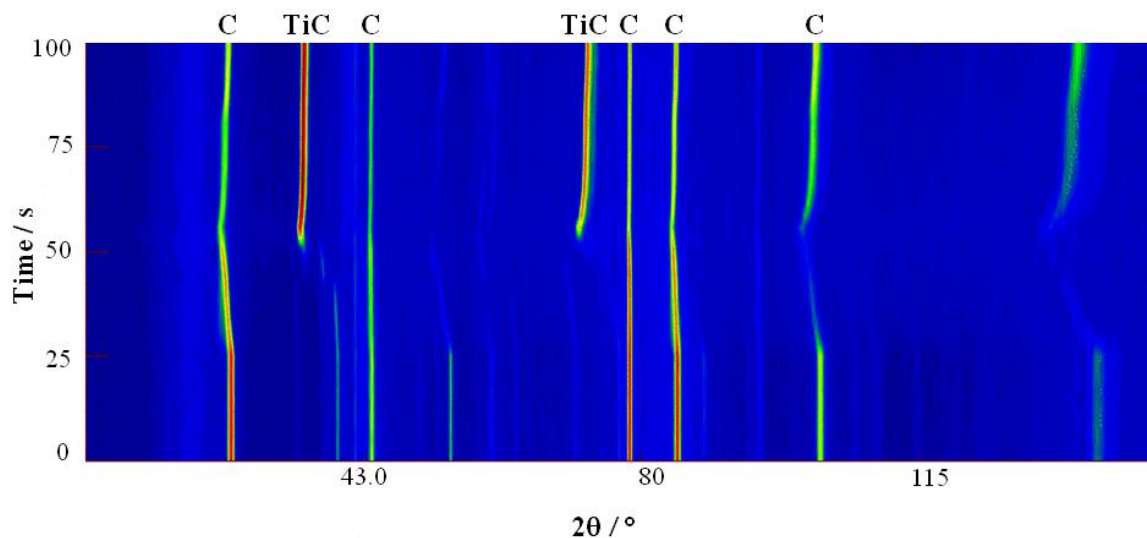
Figure 4.6. Full reaction diffraction profile for *sample 4*. The formation of TiC (~ 50 s) is indicated by new peaks appearing at *ca.* 36 ° and 72 ° 2θ.

Fig. 4.7 shows the crucial steps for *sample 4* reaction (diffractograms collected *in situ* on D20 (500 W MW; patterns collected every 10 s, 90° take off angle, $\lambda = 1.54$ Å)). At t=10 s, peak shifts due to thermal expansion (to lower 2θ) are observed; no new phases appear at this step. At t = 20 s, β-Ti (*) appears, while at t = 50 s TiC (♦) and C (○) are present. At t = 90 s, the reaction is complete, the system cools and the lattice returns to its initial dimensions (as is observed by the peaks migrating back to their original 2θ values).

In *sample 4, TiC appears in 50 s.* By 90 s the reaction is complete (TiC = 100(3) wt%). Further, from 90 s onwards, temperature starts to decrease - even with MWs still irradiating the sample (*cf.* Fig. 4.13).[15]

---

[15] Time scales for *sample 3* and *4* are different (in Figs. 4.4 and 4.6, respectively). This is merely due to the acquisition time used during experiment on the beam line. However, in both cases, reactions are over and no changes can be observed by 120 and 90 s, respectively.

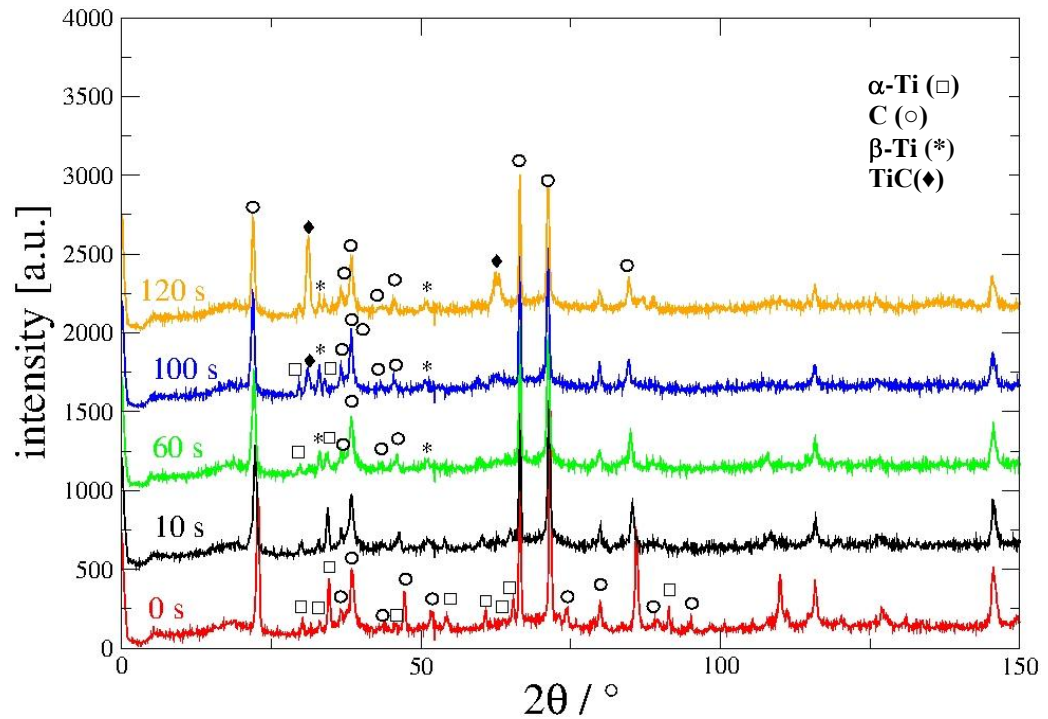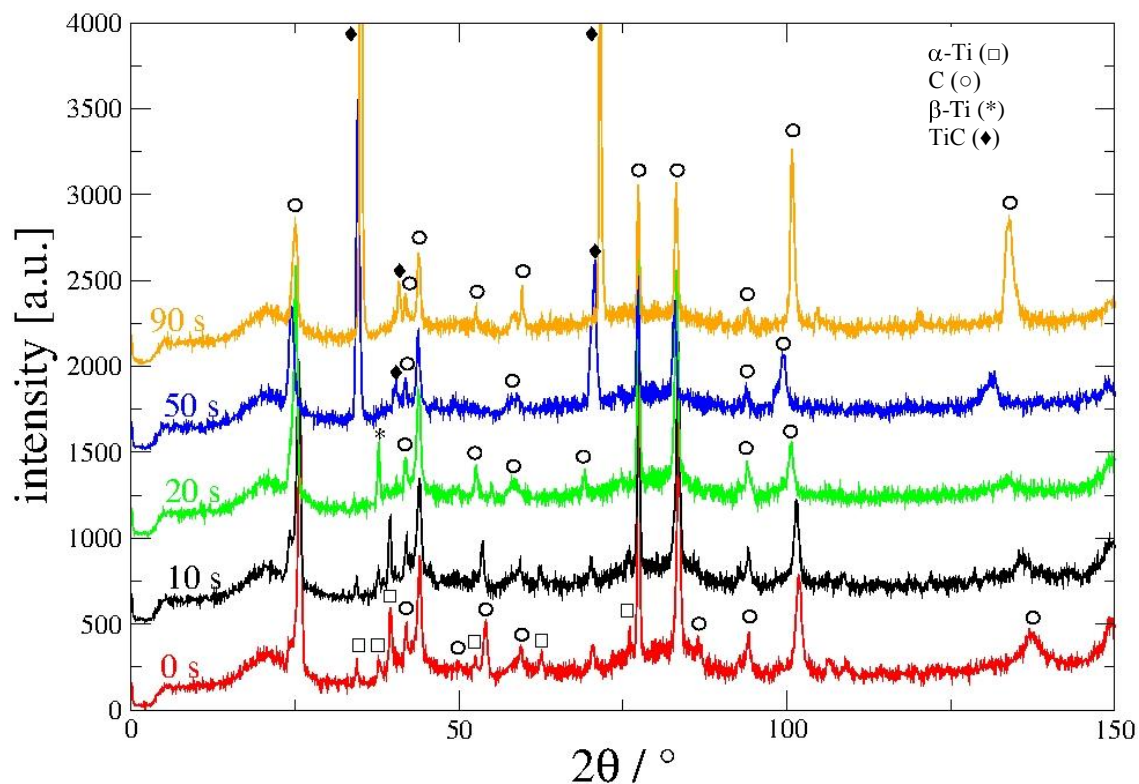**Figure 4.7** *Sample 4*. As in Fig. 4.7, for clarity, diffractograms have been normalised at 0, 10, 20, 50, and 90 s by shifting their intensity and adding a constant of, respectively, 0, 500, 1000, 1500, 2000. Reflections from α-Ti (□), C (○), β-Ti (*), and TiC (♦) are indicated.

4.2.2.3 Rietveld refinement.

Rietveld refinement has been performed for *samples 1-4*. In all the cases, starting models for refinement were taken from the ICSD data-base (ICSD reference for: α-Ti [10]; C [11]; β-Ti: [12]; and TiC [13]). In *sample 1* and *2,* apart from remaining C susceptor, only TiC was present at the end of reaction. In both cases, the background was modelled using a polynomial of 6th degree (Nba=0, in Fullprof). Scale factor, zero point and cell parameters were treated as variables and subsequently refined until convergence was achieved. Peak widths and profile coefficients (peak

shape was modelled using the Thompson-Cox-Hastings pseudo Voigt[16] function, in both cases) were also subsequently refined, until convergence.

In both *sample 3* and *4*, at the beginning of the reaction, α-Ti and graphite were included as starting reactants. In *sample 3*, the background was modelled using a linear interpolation function (four coefficients linear interpolation, Nba=4 in Fullprof). Scale factor, zero point and cell parameters were treated as variables and subsequently refined all along the reaction path. Peak widths and profile coefficients (peak shape was modelled using the Thompson-Cox-Hastings pseudo Voigt function) were also subsequently refined.

In *sample 4*, the background was refined by manually creating a list of all the points (Nba=132), while scale factor, zero point, cell parameters and peak widths and profile coefficient were treated as for *sample 3*.

β-Ti and TiC phases were subsequently added in later datasets and refined (as for α-Ti).

Crystallographic data from Rietveld refinements performed for the four samples are presented in table 4.1. Due to the preferred orientation and anisotropic peak broadening of graphite, Rietveld refinement for TiC (both against PXD and PND) is very challenging. Indeed, some previous works only present a qualitative analysis (*e.g.*, [4]). Nevertheless, an attempt to make the Rietveld refinement working in order to perform a quantitative

---

[16] Thompson, P., D. E. Cox, et al. *Rietveld refinement of Debye-Scherrer synchrotron X-ray data from Al$_2$O$_3$*, Journal of Applied Crystallography, 1987. **20**(2): 79-83.

analysis was made and reported hereafter. However, this has to be taken with a grain of salt. Indeed, the uncertainties on the estimated parameters remain large, as shown in Table 4.2, which suggests that the refinement was not completely successful.

Sample No.	*Sample 1*	*Sample 2*	*Sample 3*	*Sample 4*
Instrument, radiation wavelength	X-ray, Cu $K_{\alpha 1}$	X-ray, Cu $K_{\alpha 1}$	Neutron, $\lambda=1.36\text{Å}$	Neutron, $\lambda=1.54\text{Å}$
Phases present (at the end of reaction)	TiC (+C)	TiC (+C)	β-Ti TiC (+C)	TiC (+C)
Crystal system – Space group	F $m\,\bar{3}\,m$	F $m\,\bar{3}\,m$	I $m\,\bar{3}\,m$ (25(7) wt% F $m\,\bar{3}\,m$ (73(6) wt%) P $6_3/\,m\,m\,c$	F $m\,\bar{3}\,m$ P6_3/$m\,m\,c$
TiC a-parameter [Å] unit cell volume [Å^3]	4.26643(1) 77.66(4)	4.26865(3) 77.78(1)	4.28642(6) 78.76(2)	4.30077 (1) 79.550(4)
Calculated density [g/cm^3]	5.124	5.140	5.031	5.003
R_p	40.7	44.6	38.3	52.8
R_{wp}	47	54.4	32.7	47.0
χ^2	22.9	19.1	2.02	9.96

Table 4.2 Crystallographic data from Rietveld refinement for *samples 1, 2, 3* and *4*.

Figs 4.8 - 4.11 show selected refinement profile plots for *samples 1-4*. In all cases, the red line shows the experimental data, the upper black line shows the calculated profile, the blue line is the difference between the

observed and calculated profiles, while (+) symbols show the position of

Bragg peaks.
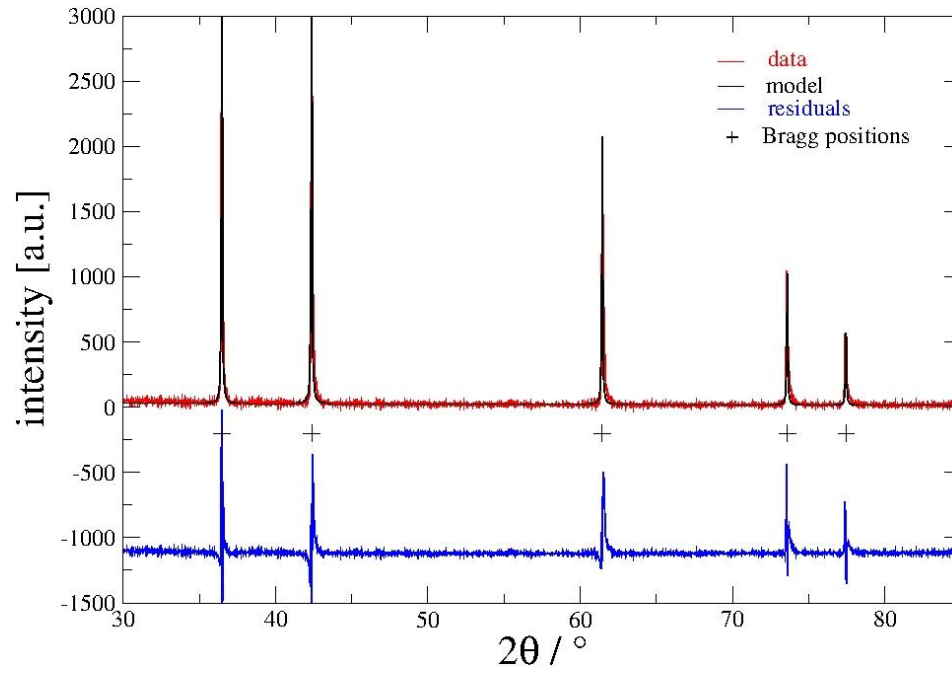
Figure 4.8 Profile plot for Rietveld refinement against PXD data, for *sample 1* (MMC, 10 min, 800 W). The pattern is dominated by five peaks that match with the reflections from the (111), (200), (220), (311) and (222) planes of the cubic structure of TiC.
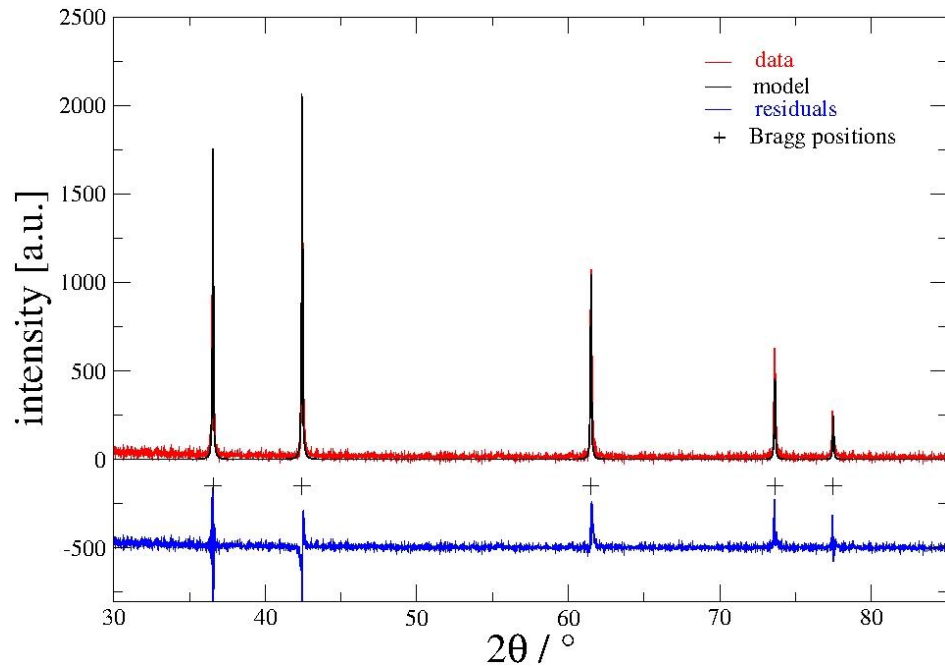
Figure 4.9 Profile plot for Rietveld refinement against PXD data, for *sample 2* (SMC, Gaerling set up, 10 min, 1 kW). As for Fig. 4.8, the pattern is dominated by five peaks that match with the reflections from the (111), (200), (220), (311) and (222) planes of the cubic structure of titanium carbide.

(a)

(b)

(c)

153
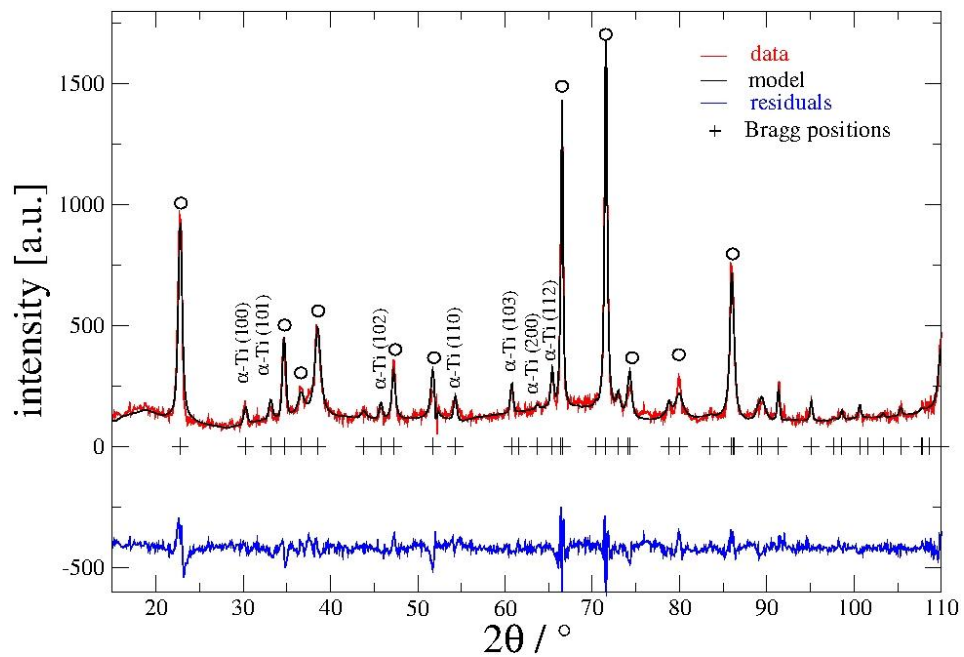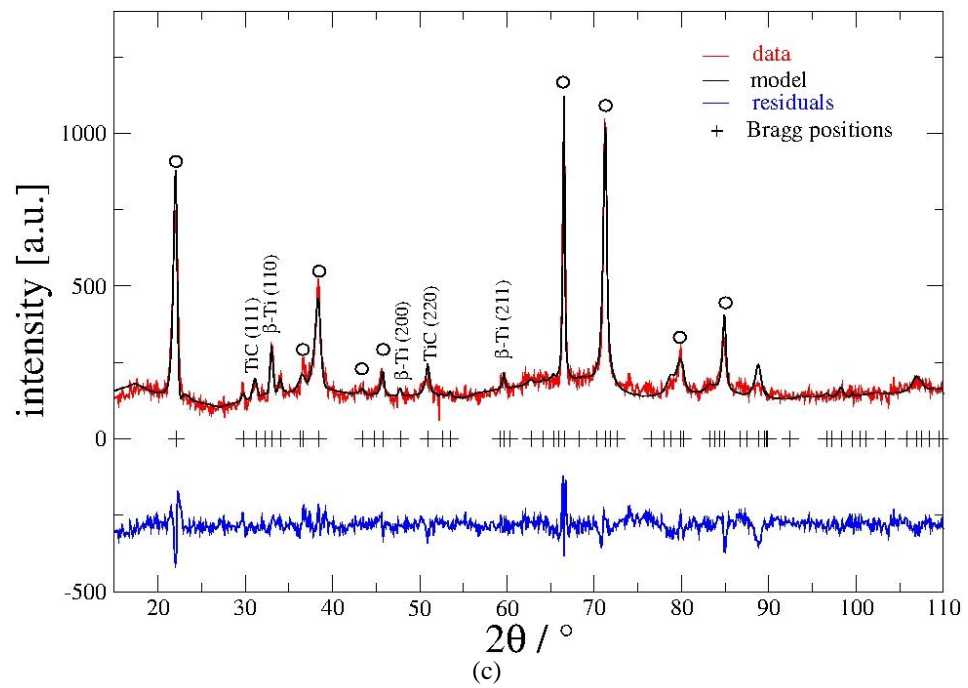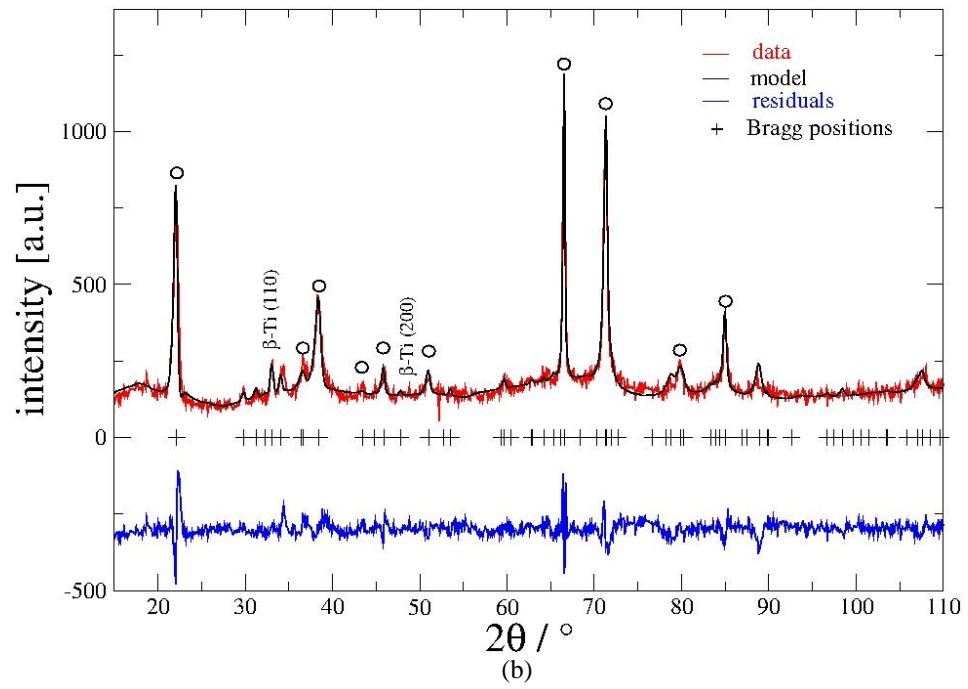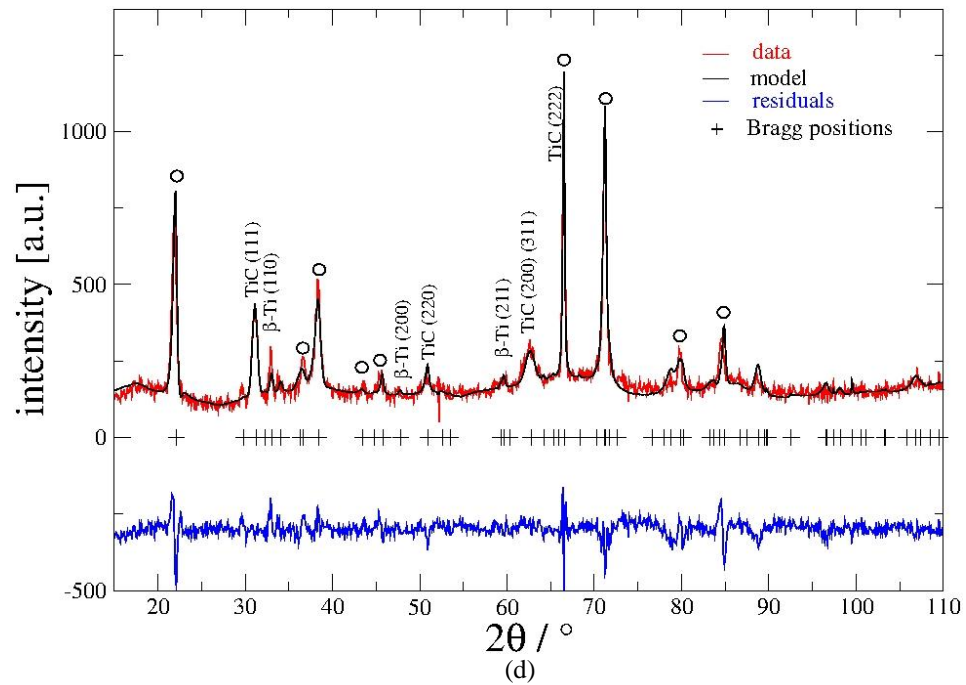
Figure 4.10 (a) Profile plots for Rietveld refinement against neutron data for *sample 3*, (a) at t = 0; (b) at t = 60 s; (c) at t = 100 s; (d) at t = 120 s. Reflections from C (○) are indicated.

(a)
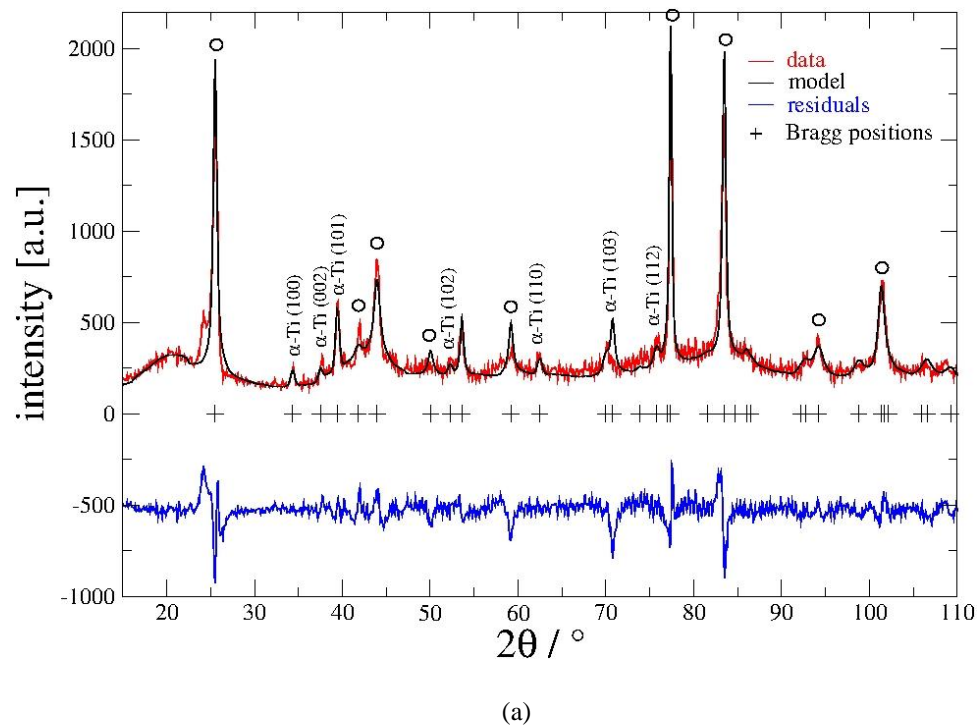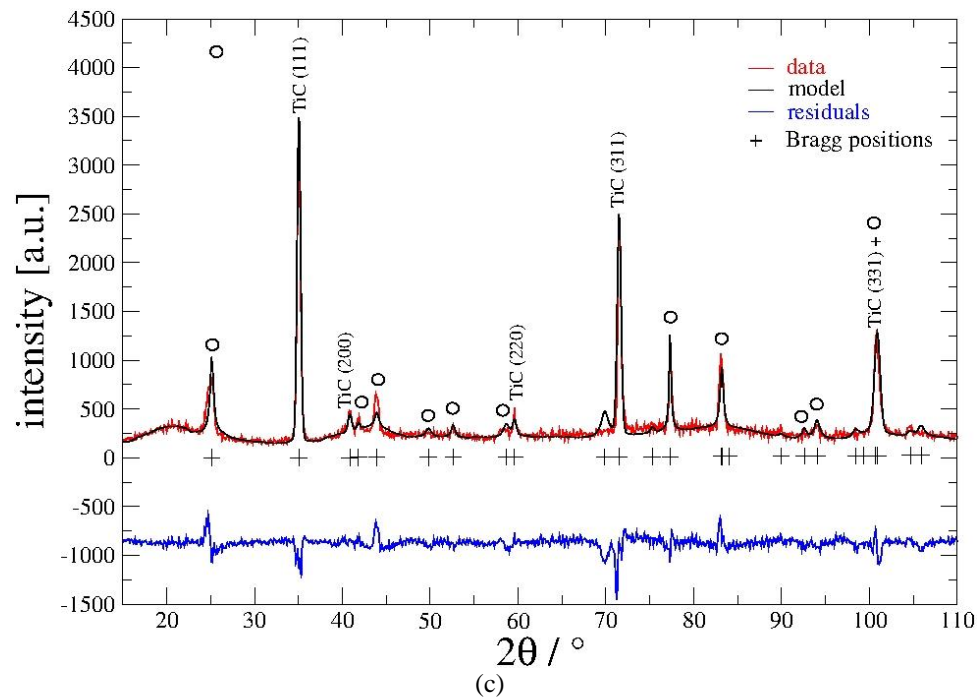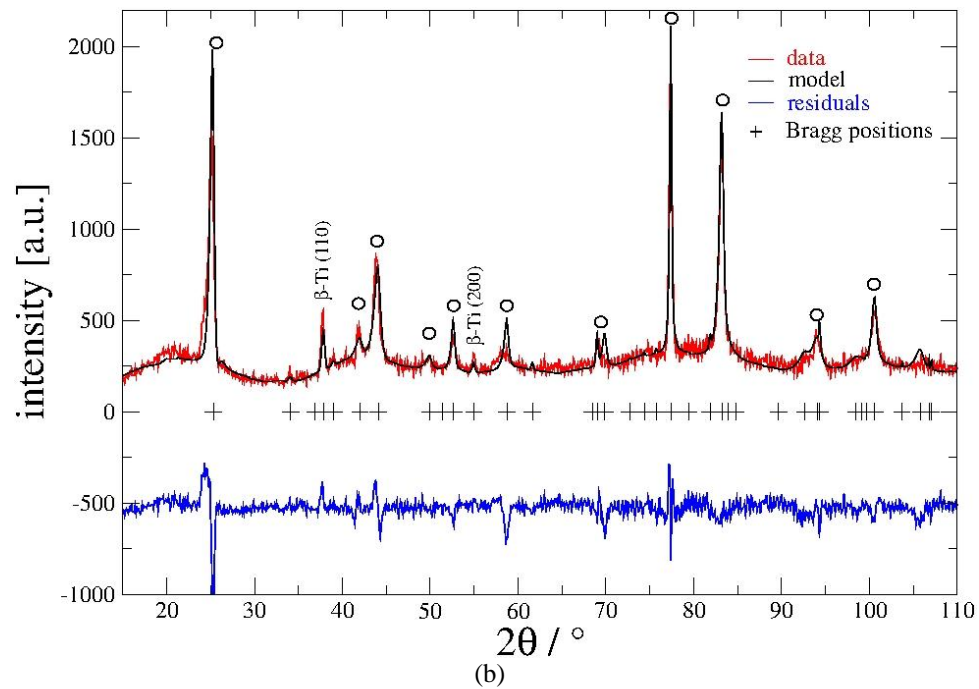
Figure 4.11 (a) Profile plots for Rietveld refinement against neutron data for *sample 4*, (a) at t = 0. (b) at t = 20 s. (c) at t = 90 s (end of reaction).

4.2.2.4 Temperature measurement

As reported in Chapter 1, Section 1.3.1, temperature measurement in MW reactions is not a trivial process as, within the sample, inhomogeneous heating may occur at the millimeter – or sub-millimeter scale. Further, the two most common systems for temperature measurements, thermocouples and pyrometers, are unreliable as the first may cause perturbation of the MW field and the second only gives surface temperature - which will be the coolest part of the sample, due to the nature of inverse temperature profile found in MW heating mechanism [14, 15].

In this project, to overcome these difficulties and avoiding misleading temperature measurements, an *in situ* "crystallographic thermometer" was employed. Taking advantage of both the presence of graphite in all samples and that the linear thermal expansion of graphite is well known with high accuracy over a wide temperature range – from 293 to 1473 K – the thermal expansion coefficient and hence temperature using the refined graphite lattice parameters [4, 16] were calculated.

The *c*-parameter at a given temperature T is given by Eq. 4.1:

$$c(T) = c_{Tr} + \alpha \, c_{Tr} \, (T\text{-}Tr) \qquad \text{Eq. 4.1}$$

where α is the linear thermal expansion coefficient $(27.7(\pm 0.6) \times 10^{-6} \text{ K}^{-1})$ [16], *c(T)* and c_{Tr} (=6.7079 Å, at 298 K [4]) are the *c*-parameter values at the unknown (*T*) and at the reference temperature (*T$_r$*) respectively. *c(T)* is calculated at each temperature by performing sequential Rietveld

156

refinements against the PND data collected *in situ*. Knowing all the variables, the unknown temperature T can be then determined by rearranging Eq. 4.1 as following:

$$T = T_r + \frac{c(T) - c_{Tr}}{\alpha}$$ Eq. 4.2

The error on T is given by the root mean square deviation (RMSD) method. If $\overline{T} = T - T_r$ and $\overline{c} = c(T) - c_{Tr}$, then Eq. 4.2 can be rewritten as:

$$\overline{T} = \frac{\overline{c}}{\alpha}$$ Eq. 4.3

and the error on $\overline{T}$ is given by the propagation of errors on c and α :

$$\frac{1}{\overline{T}}\sqrt{\left(\frac{\delta\overline{T}}{\delta\overline{c}}\delta\overline{c}\right)^2 + \left(\frac{\delta\overline{T}}{\delta\alpha}\delta\overline{\alpha}\right)^2} = \frac{\delta\overline{T}}{\overline{T}} = \sqrt{\left(\frac{\delta\overline{c}}{\overline{c}}\right)^2 + \left(\frac{\delta\alpha}{\alpha}\right)^2}$$ Eq. 4.4

The above computation was used to produce Figs. 4.12 and 4.13, which show temperature *vs* time (both against PND data) for *sample 3* and *4*, respectively. Tables 4.2 and 4.3 report temperature (with its uncertainty), related to Figs. 4.12 and 4.13, respectively.
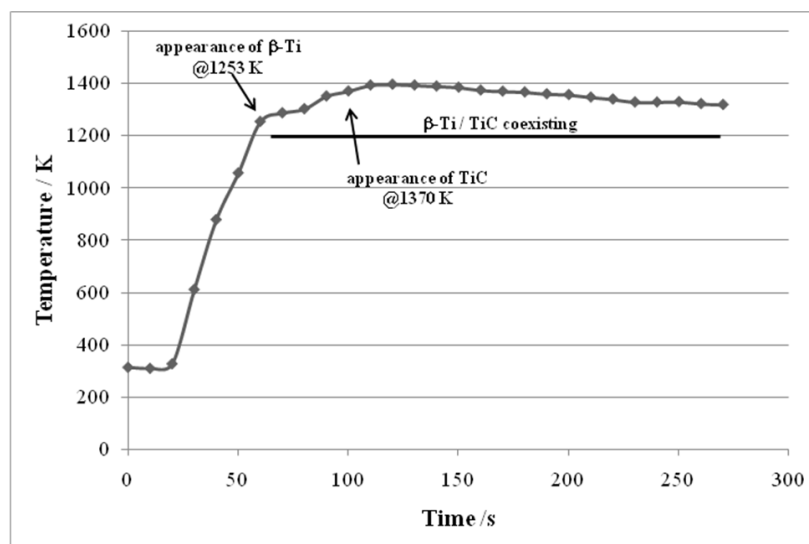
Figure 4.12 Reaction temperature *vs* reaction time for *sample 3*. β-Ti appears at higher temperature than conventional furnace case (1253 K and 1156 K [4], respectively). The experimental T at which the presence of TiC phase is firstly observed in the diffraction pattern is 1370 K. After the appearance of TiC, the temperature increases to a maximum of 1396 K after *ca.* 120 s of MW irradiation, and begins to slowly decrease beyond this time.

Time (s)	Temperature (K)	Temperature (°C)	δT (°C)
0	312.4	39.3	0.8503
10	308.5	35.4	0.7659
20	325.9	52.8	1.144
30	610.3	337	7.304
40	878.1	605	13.10
50	1057	784	16.97
60	1253	980	21.23
70	1317	1044	22.62
80	1337	1064	23.05
90	1351	1078	23.34
100	1370	1097	23.76
110	1393	1119	24.26
120	1396	1123	24.32
130	1393	1119	24.26
140	1389	1115	24.17

158

150	1385	1112	24.08
160	1374	1100	23.85
170	1370	1097	23.75
180	1367	1094	23.69
190	1360	1087	23.53
200	1357	1083	23.47
210	1347	1073	23.26
220	1339	1065	23.09
230	1328	1054	22.85
240	1328	1054	22.85
250	1330	1056	22.89
260	1322	1049	22.72
270	1319	1045	22.64

Table 4.3 Data for Fig. 4.12 (where reaction temperature *vs* reaction time is plotted, for *sample 3*).
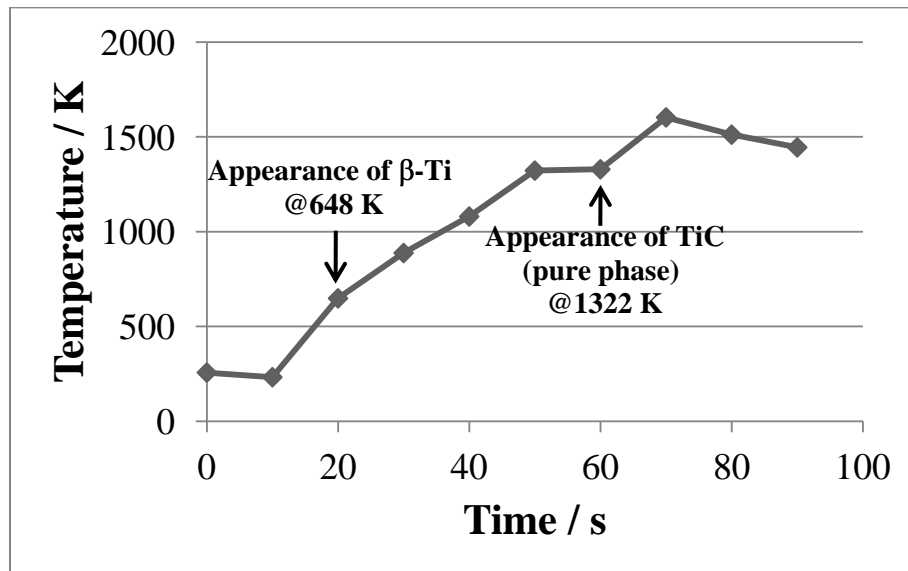
Figure 4.13 Reaction temperature *vs* reaction time for *sample 4*.The α→β phase transition occurs after ~20 s, at a much lower temperature (648 K) than both *sample 3* and conventional furnace. The experimental T at which the presence of TiC phase is firstly observed in the diffraction pattern is 1322 K. After the appearance of TiC, the temperature increases up to a maximum of 1603 K (after *ca.* ~70 s of MW irradiation), and slowly decreases thereafter.

159

Time (s)	Temperature (K)	Temperature (°C)	error on T
0	257	--	0.355
10	233	--	0.880
20	648	375	8.13
30	888	615	13.3
40	1080	807	17.5
50	1322	1049	22.7
60	1329	1056	22.9
70	1603	1329	28.8
80	1512	1239	26.8
90	1445	1172	25.4
100	1348	1075	23.3

Table 4.4 Data for Fig. 4.13 (reaction temperature *vs* reaction time for *sample 4*).

4.2.2.5 SEM

Although *sample 2*, *3* and *4* have been all processed in a high power MW set-up (*Gaerling* and *Sairem*® set-up, respectively) and all have been synthesised starting from dry pellets of α-Ti and C graphite in 1:1 stoichiometric ratio, they show differences in SEM pictures.

Sample 2 (1 kW) shows irregular particles with sizes of up to a few microns (Fig. 4.14 (a)). *Sample 3* (500 W) shows spherical crystallites of 10-50 μm (Fig. 4.14 (b)). *Sample 3* has very different particles shape compared to *sample 2* - possibly due to only partial conversion of the reactants (α-Ti+C) into TiC.

Sample 3 and *sample 4* (Fig. 4.14 (c)) looks similar. The latter also shows well-formed spheres.
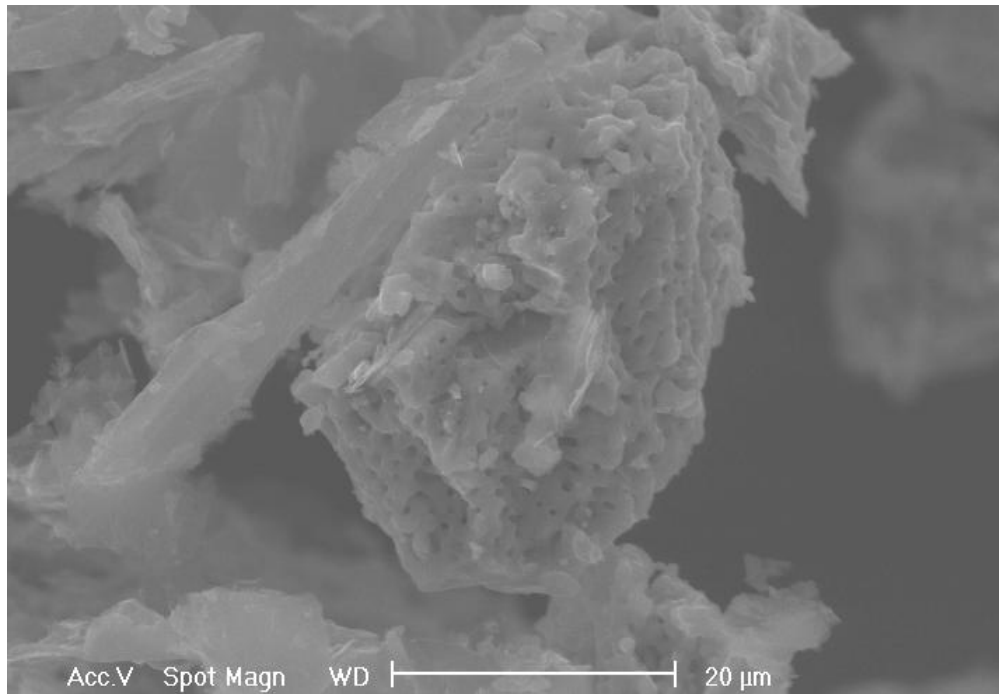
(a)
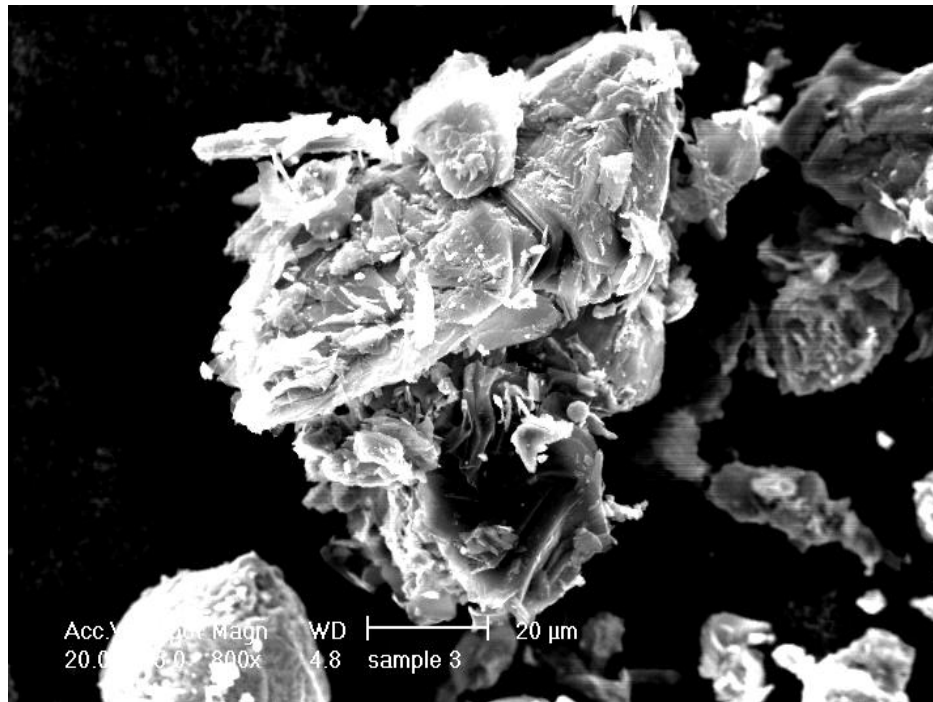
(b)
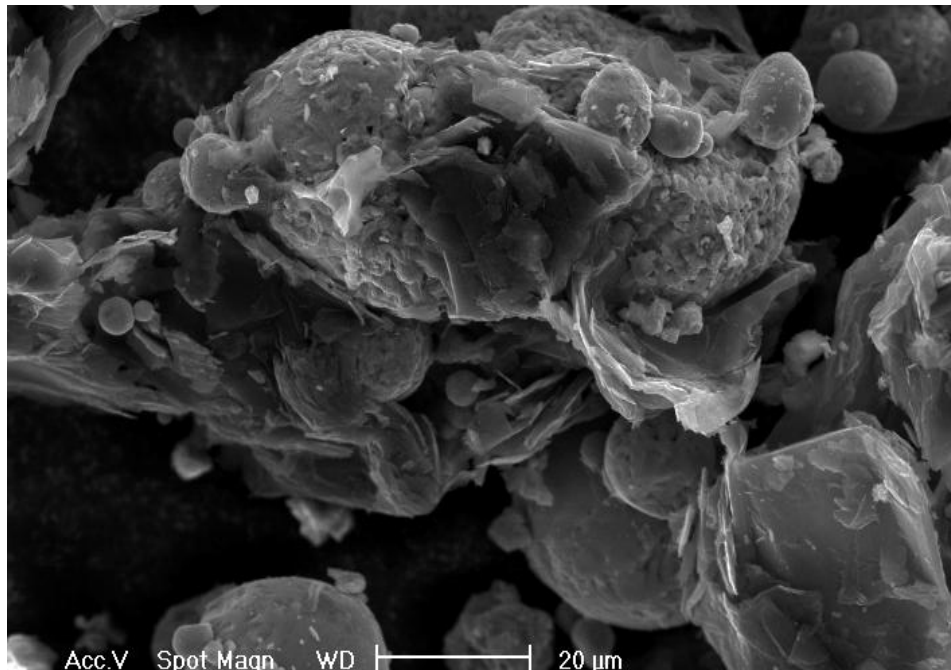
(c)

Figure 4.14 (a) SEM picture (20μm resolution) for *sample 2* (SMC, *Gaerling* set-up, 1 kW, 10 min process); (b) SEM picture (20μm) for *sample 3* (Sairem set-up, 0.500 kW); (c) SEM picture (20μm) for *sample 4* (Sairem set-up, 0.500 kW).

Fig. 4.15 shows a SEM picture (20μm) for *sample 1* (MMC, 0.800 kW). It

shows irregular particles with sizes of up to a few microns
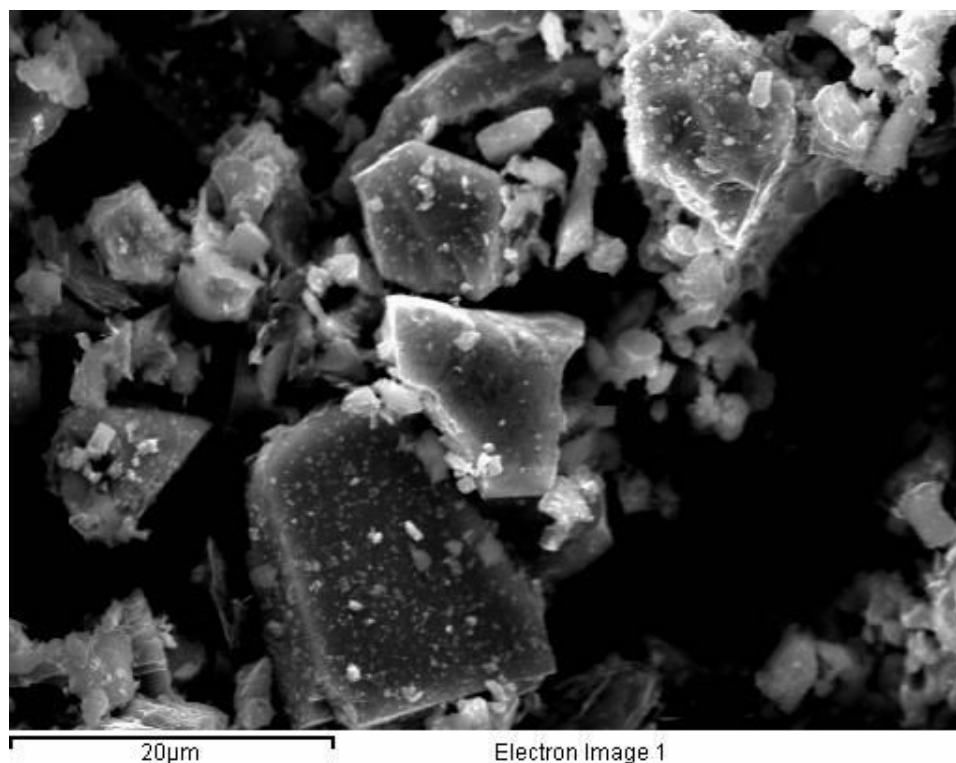
Figure 4.15 SEM images of *sample 1* (MMC, 800 W).

4.2.2.6 Raman spectroscopy

Selected samples (*sample 1*, *3* and *4*) were analysed by Raman spectroscopy, in order to determine if any amorphous phases were present at the end of the reaction.

Neither stoichiometric TiC nor Ti have Raman-active vibrational modes. The spectrum of graphitic carbon, instead, contains bands signals at 260, 420, 605, 1320 and 1590 cm^{-1}; the last two bands are assigned to A_{1g} and E_{2g} vibrational modes, respectively [17, 18]. The Raman spectra of commercially available graphite and TiC (from literature data) are shown in Fig. 4.18 (a) and (b), respectively. TiC exhibits all the bands of

graphite, suggesting that unreacted carbon is present in the TiC powder [17]. A possible explanation for the low peak intensities in commercially available TiC is that the bulk of the material may be stoichiometric TiC, which has no Raman-active vibrational modes.
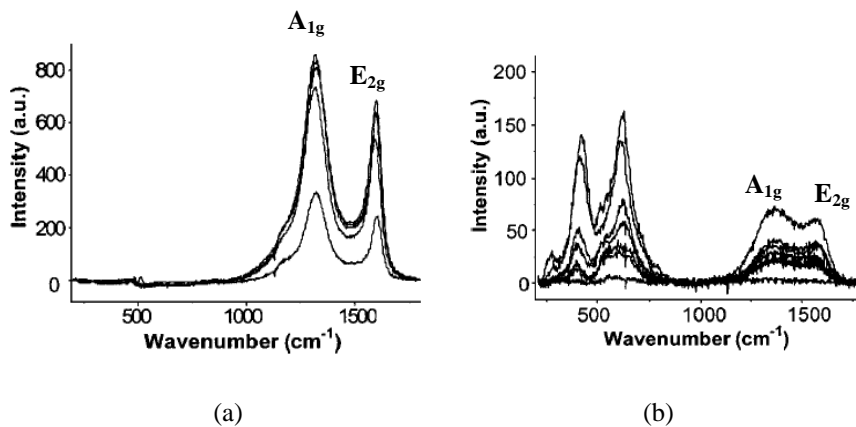
Figure 4.16 (a) Raman spectra (literature data) taken from different particles of commercially available graphite [17]. (b) Raman spectra (literature data) of commercially available TiC powder (*Aldrich,* purity of 98%) [17], taken from seven different particles.

Figs. 4.17, 4.18, and 4.19 show Raman spectra for *samples 1, 3* and *4*, respectively. In all cases, two broad peaks are visible around 260, 420, 605, 1320 and 1590 cm^{-1}, which indicates the presence of unreacted carbon in the sample, attributed to the graphite used as susceptor.
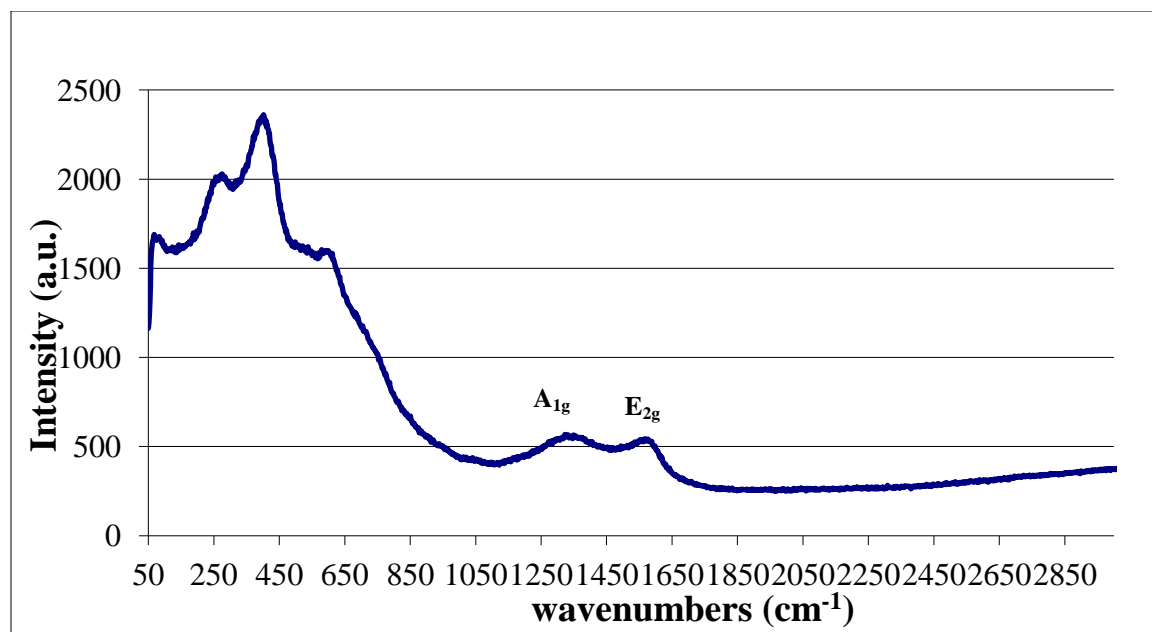
Figure 4.17 Raman spectrum for *sample 1* (MMC, 800 W).
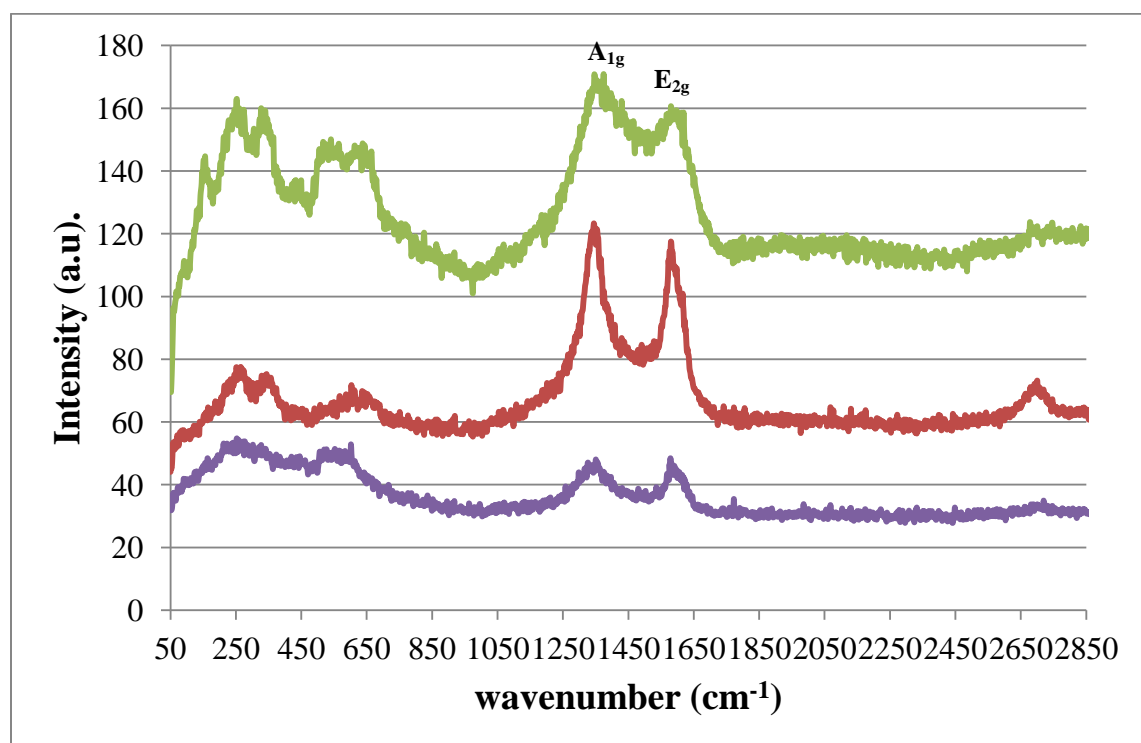
Figure 4.18 Multiplot of Raman spectra for *sample 3,* collected from different region of the same sample (SMC, 500 W).

165
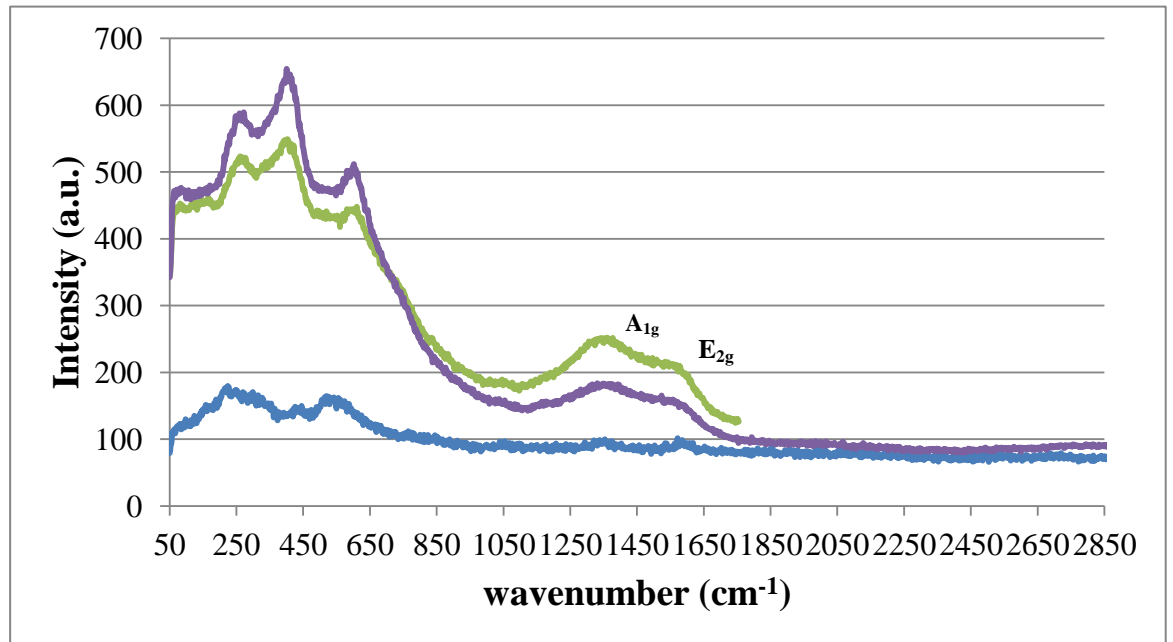
Figure 4.19 Multiplot of Raman spectra for *sample 4,* collected from different regions of the same sample (SMC, 500 W).

4.3 Discussion and Conclusion

Results from syntheses performed in both MMC and SMC reactors demonstrated that it is possible to produce TiC, in air, by using α-Ti and graphite as a source of carbon, in a time range of minutes (MMC, *sample 1*) or even seconds (SMC, *sample 3* and *4*).

Primarily focusing on *sample 3* and *sample 4* (*in situ* SMC reactions), some considerations can be drawn.

First, in *sample 3,* the $\alpha \rightarrow \beta$ transition phase, (occurring at 1156 K in conventional furnace [4]) was observed at 1253±21 K in the diffraction pattern, while in *sample 4*, it was observed at *648 K* (*cf*. Figs. 4.12 and 4.13 and related Tables 4.2 and 4.3)*.* Nonetheless, in both *samples 3* and *4*,

the experimental T at which the presence of TiC phase is firstly observed in the diffraction patterns is similar: 1370 ± 23.7 K and 1322 ± 22.7 K, respectively (and both higher than the conventional case: T~1073 K [4]), but the time of formation of TiC is ~100 s in *sample 3* and ~50 s in *sample 4*.

This suggests that, in the case of MW induced formation of Ti-C from Ti + C, the $\alpha\rightarrow\beta$ transition acts as a trigger mechanism for this reaction, and the lower the temperature for this transition, the quicker the formation of TiC. This phase transition occurs at a lower temperature than in the conventional case, *ca.* 1200 K [4], and the reaction is several orders of magnitude faster.

Second, by comparing the temperature at which TiC appears in the diffraction pattern in *sample 4* (1322 K) - with the conventional furnace case (~1073K [4], Fig. 4.22) the former is higher than the latter by ~300K. In the MW case, the temperature was calculated by using graphite as an "internal thermometer", (thus basically obtaining the *bulk temperature*), while in the case of conventional furnace, Winkler *et al.* registered the temperature by means of a thermocouple mounted on the sample. Consequently, the difference between the two cases could be possibly ascribed also to temperature measurement methods (and related errors).
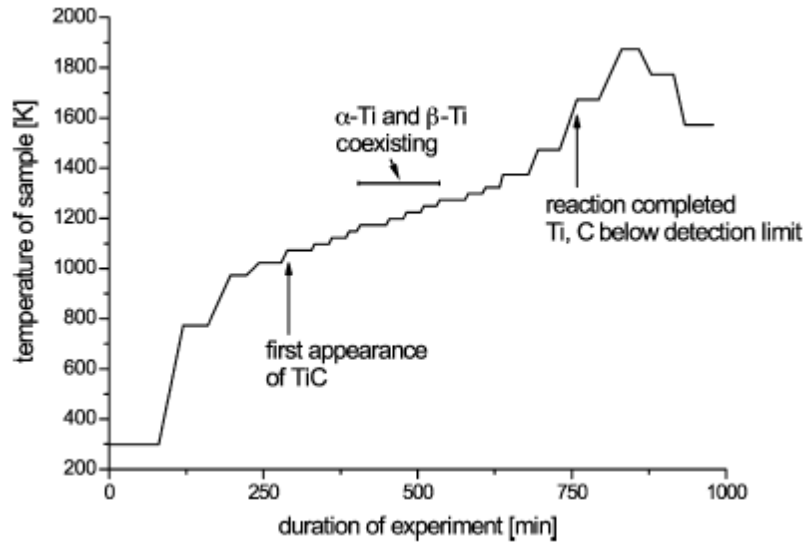
Figure 4.20 Time-temperature plot for the conventional solid state reaction of Ti + C, as reported by Winkler *et al.* [4].

Third, in *sample 3*, α-Ti and graphite are the initial reactants, β-Ti is visible after 60 s of reaction (at T = 1253±21.23 K), while TiC peaks appear after 100 s (T=1370±23.7 K) – compared with 250 min and T~1073 K in a conventional furnace [4]. Moreover, even if the β-Ti concentration slowly decreases (Fig. 4.21), it is always present in the reaction mixture, concomitantly with TiC.

In *sample 4*, β-Ti peaks can be detected in 20 s and the temperature continuously increases (Fig. 4.13). The β-Ti concentration also increases (red line, in Fig. 4.22), while α-Ti concentration decreases (blue line, in Fig. 4.24). TiC appears in 50 s, when T=1322±22.7 K (green line, in Fig. 4.22). As stated in Eq. 2.2, Chapter 2, in Section 2.1, the power dissipated in the material is proportional to the electric field strength inside the
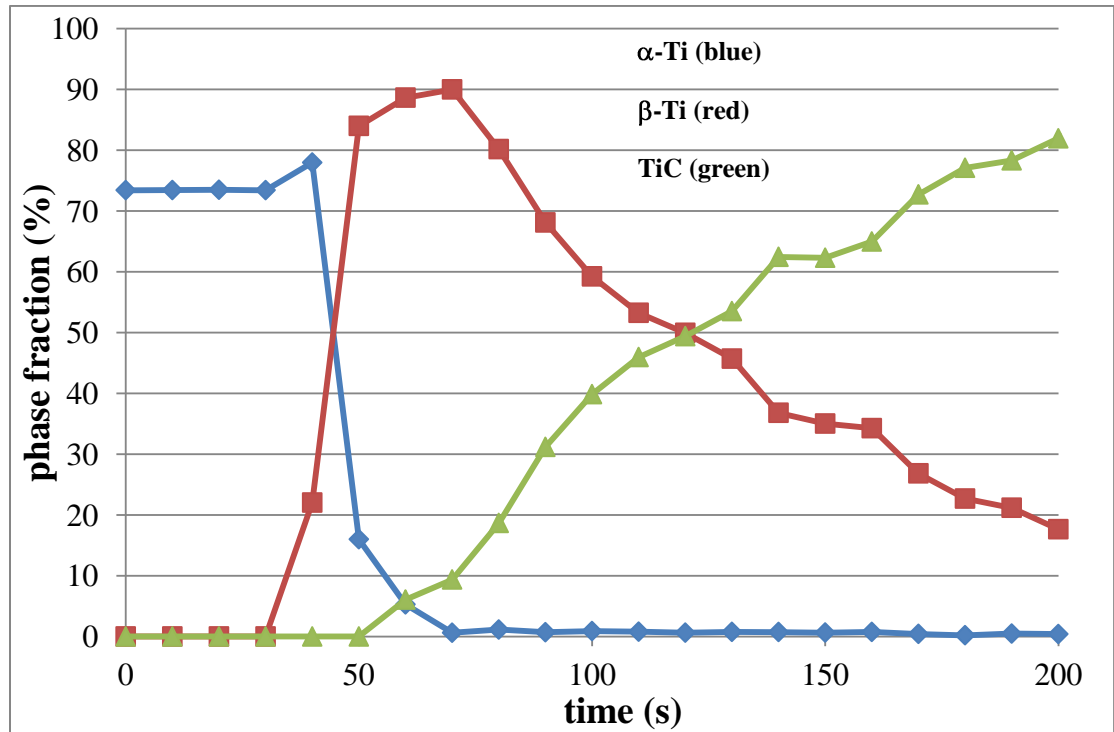
Figure 4.21 Phase fraction in *sample 3*. Although the β-Ti concentration slowly decreases, it never disappears and always coexists with TiC.

material squared, which in turn is a function of the cavity dimensions and design. In both the *sample 3* and *4* cases, the dimensions of the cavity and the design are exactly the same. However, as the difference between the two experiments relies in the position of the sample in the cavity, the higher speed of formation of β-Ti phase (and consequently of TiC) in *sample 4* could be ascribed to the creation of higher power density than in *sample 3*, thanks to a better position of the sample in the cavity. Although the ΔP (=FP-RP) on MW generator provided the same result in the cases (500 W), the difference in MW power absorbed might have been small and below the sensitivity of the instrument. Consequently, as the position of the sample in the cavity has been shown to be a crucial initial step in the

success of the reaction, this aspect requires further investigation and future studies.
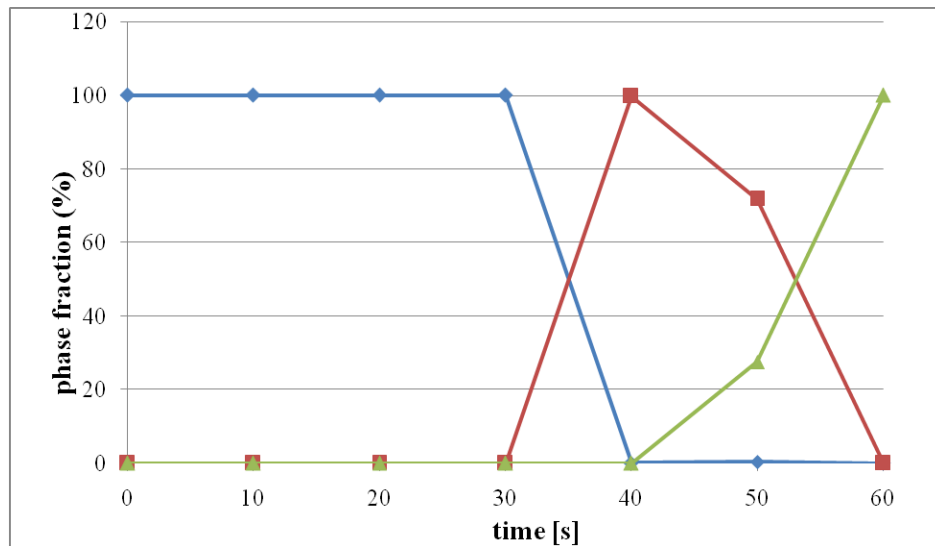
Figure 4.22 Phase fraction vs reaction time for α-Ti (blue), β-Ti (red) and TiC (green), in the SMC synthesis of *sample 4*.

Further, by comparing *sample 2* (*Gaerling* SMC) and *sample 3* and *4* (*Sairem®* SMC), it is interesting to observe that different amount of MW power (1000 W and 500 W, respectively) and different irradiation times (*ca.* 10 min and few seconds, respectively) lead to different particle shape of the products. Only in *sample 3* and *4* spherical particle formation is observed, while sample 1 and 2 show mostly irregular particle size.

4.4 Preliminary Results on Other Binary and Ternary Systems and Future Studies.

This last part of the thesis is devoted to the process of different chemical systems in the SMC-MW reactor, by using the same experimental conditions and the same set-up (Sairem) already used for TiC. Tantalum (Ta) and tungsten (W) - and their related oxides, Ta_2O_5 and WO_2 respectively - were mixed with Ti and graphite, in different stoichiometric ratios (see Table 4.5).

As said in Chapter 1, the majority of these compounds are classified as "*cermets*". In particular, in the case of Ti-containing carbide cermets with Ni, Fe, Mo, Al, Co, Cu, and W, self propagating high temperature synthesis (SHS), combustion synthesis (CS), and mechanical alloying of powder mixtures at room temperature are the most common alternatives to traditional high temperature ceramic synthesis routes [19-24]. The latter still require a huge instrumentation regarding melting the metal and graphite under vacuum at a very high temperature.

MW could represent a time-saving, cost-effective and "green" way of producing such materials. Preliminary results of the fast MW synthesis probed by means of *in situ* PND of selected TiC-based cermets is reported hereafter.

4.4.1 Experimental details

The chemical systems listed below were prepared by grinding the respective elemental or oxide powders in appropriate stoichiometric ratios in an agate mortar. Each powder sample was cold pressed uniaxially in an 8 mm pellet die (Specac, 5 Tons, 5 min). The pressed pellets were embedded in the susceptor (graphite) in an open, 10 mm quartz tube. The *Sairem* MW set-up used has been extensively described in the previous Chapters 3.

A list of all the chemical 30 ternary systems processed in situ on D20 - in the Sairem SMC set-up, at ILL - is reported in Table 4.5.

System number	Chemical systems and specification of reactants	Stoichiometric Ratio
	Ti-Ta-C *(samples 1-9).* ***Ta*** = average particle size −325 mesh, Aldrich 99.9% ***Ti*** = average particle size -100 mesh Aldrich 99.7 % ***C*** = average particle size <45 μm, Aldrich 99%	
1)	**Ti – Ta – C**	**(0.1:0.9:2)**
2)	**Ti – Ta – C**	**(0.2:0.8:2)**
3)	**Ti – Ta – C**	**(0.3:0.7:2)**
4)	**Ti – Ta – C**	**(0.4:0.6:2)**
5)	**Ti – Ta – C**	**(0.5:0.5:2)**
6)	**Ti – Ta – C**	**(0.6:0.4:2)**
7)	**Ti – Ta – C**	**(0.7:0.3:2)**
8)	**Ti – Ta – C**	**(0.8:0.2:2)**

9)	**Ti – Ta – C**	**(0.9:0.1:2)**
	Ti-W-C** (samples 10-19).* ***W = average particle size 12 μm, Aldrich 99.9% ***Ti*** = average particle size -100 mesh Aldrich 99.7 % ***C*** = average particle size <45 μm, Aldrich 99%	
10)	**Ti – W – C**	**(1:1:1)**
11)	**Ti – W – C**	**(0.1:0.9:1)**
12)	**Ti – W – C**	**(0.2:0.8:1)**
13)	**Ti – W – C**	**(0.3:0.7:1)**
14)	**Ti – W – C**	**(0.4:0.6:1)**
15)	**Ti – W – C**	**(0.5:0.5:1)**
16)	**Ti – W – C**	**(0.6:0.4:1)**
17)	**Ti – W – C**	**(0.7:0.3:1)**
18)	**Ti – W - C**	**(0.8:0.2:1)**
19)	**Ti - W - C**	**(0.9:0.1:1)**
	Ti-WO$_2$-C** (samples 20-26).* ***WO$_2$ = average particle size -100 mesh, Aldrich 99.9% ***Ti*** = average particle size -100 mesh Aldrich 99.7 % ***C*** = average particle size <45 μm, Aldrich 99%	
20)	**Ti –WO$_2$ – C**	**(0.3:0.7:1)**
21)	**Ti –WO$_2$ – C**	**(0.4:0.6:1)**
22)	**Ti –WO$_2$ – C**	**(0.5:0.5:1)**
23)	**Ti –WO$_2$ – C**	**(0.6:0.4:1)**
24)	**Ti –WO$_2$ – C**	**(0.7:0.3:1)**
25)	**Ti –WO$_2$ – C**	**(0.8:0.2:1)**

26)	**Ti –WO$_2$ – C**	**(0.9:0.1:1)**
	_Ti-Ta$_2$O$_5$-C (samples 27-30)._ **_Ta$_2$O$_5$_** = average particle size <20 μm, Aldrich 99.9% **_Ti_** = average particle size -100 mesh Aldrich 99.7 % **_C_** = average particle size <45 μm, Aldrich 99%	
27)	**Ti –Ta$_2$O$_5$ – C**	**(0.6:0.4:2)**
28)	**Ti –Ta$_2$O$_5$ – C**	**(0.7:0.3:2)**
29)	**Ti –Ta$_2$O$_5$ – C**	**(0.8:0.2:2)**
30)	**Ti –Ta$_2$O$_5$ – C**	**(0.9:0.1:2)**

Table 4.5. All the systems processed by means of _in situ_ MWs, in _Sairem_ set-up, at ILL. Stoichiometric ratios were chosen in order to observe the role (i.e., on the speed and the nature of product formation) of different concentration of Ti in the mixture.

4.4.2 Preliminary Results and Discussion

4.4.2.1 Ti–Ta–C system.

Diffractograms for all the $Ti_{(1-x)}Ta_xC_y$ compositions are shown in Fig. 4.23. Each pattern was collected on D20 with a 5 min acquisition time, 90° take off angle and wavelength of 1.54 Å. For each stoichiometric mixture, only the product of the reaction is reported (and not the entire pathway), in order to easily compare all the systems.
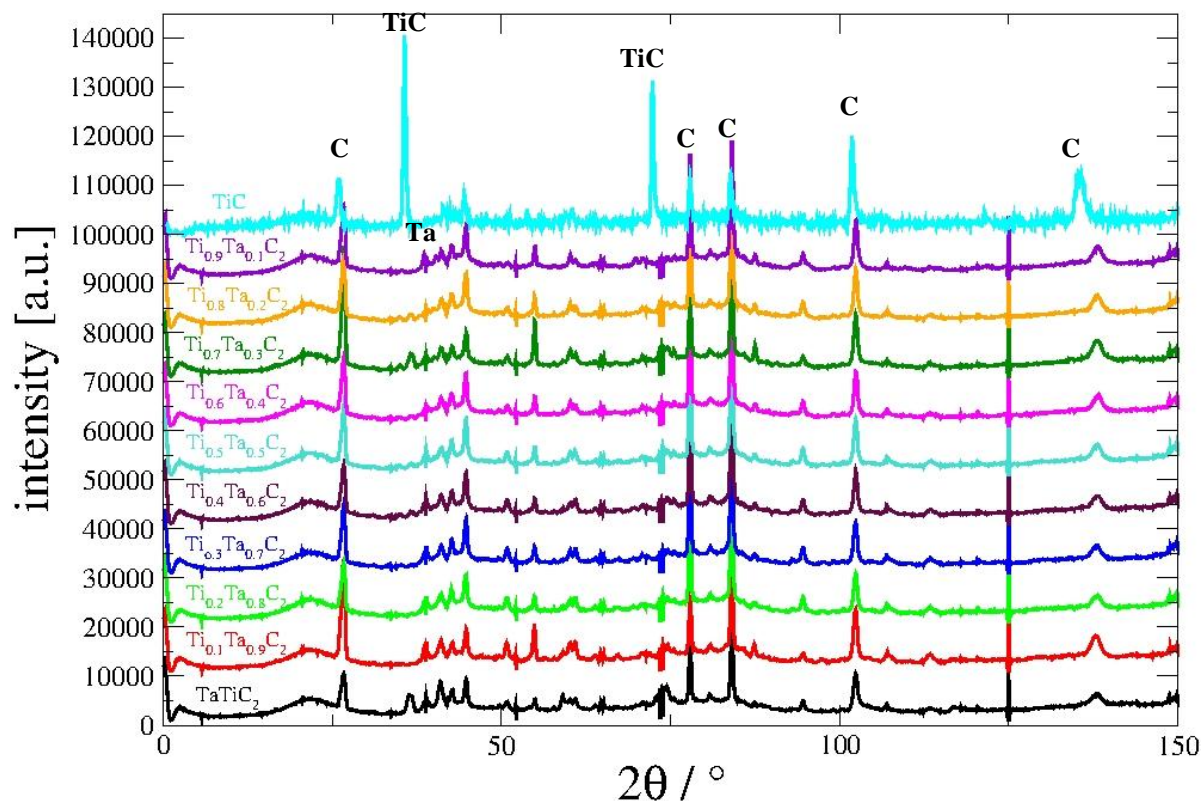
Figure 4.23. Diffractograms for $Ti_{(1-x)}Ta_xC_y$ system (x=0.1-0.9, $\Delta x = 0.1$ and y=2). From the bottom, in black, TaTiC (1:1:2 ratio); in red, $Ti_{0.1}Ta_{0.9}C_2$; in green, $Ti_{0.2}Ta_{0.8}C_2$; in blue, $Ti_{0.3}Ta_{0.7}C_2$; in yellow, $Ti_{0.4}Ta_{0.6}C_2$; in turquoise $Ti_{0.5}Ta_{0.5}C_2$; in pink, $Ti_{0.6}Ta_{0.4}C_2$; in dark green, $Ti_{0.7}Ta_{0.3}C_2$; in orange, $Ti_{0.8}Ta_{0.2}C_2$; and in violet $Ti_{0.9}Ta_{0.1}C_2$. For comparison, MW-processed TiC (in cyan) has been reported (*sample 4*, as described in Chapter 4). For clarity, diffractograms have been normalized at 0, 10000, 20000, 30000, 40000, 50000, 60000, 70000, …, 100000 by shifting their intensity and adding a constant of, respectively, 0, 10000, 20000, 30000, 40000, 50000, 60000, 70000, …, 100000.

By irradiating $TiTaC_2$ pellet by means of MWs (500 W), two new peaks at *ca.* 36 ° and 72 ° 2θ (Fig. 4.23 (black line)) appear in the diffractogram.

In all the cases, with increasing temperature, a shift of C peaks to lower 2θ angles is observed (which return to the original position when the system cools down, *i.e.,* when the MWs are switched off).

4.4.2.2 Ti-W-C system.

Fig. 4.24 shows the product of the *in situ* reaction for each stoichiometric ratio, for Ti-W-C system. For comparison, the cyan diffractogram shows TiC, as obtained in the same MW reactor (*cf.* sample 4).

As in Ti-Ta-C system, also for Ti-W-C mixtures, and, in particular, for the nominal $Ti_{0.5}W_{0.5}C$, $Ti_{0.6}W_{0.4}C$, $Ti_{0.7}W_{0.3}C$, $Ti_{0.8}W_{0.2}C$, and $Ti_{0.9}W_{0.1}C$ compounds, characteristic TiC peaks at 31 °2θ and 73 °2θ are clearly visible; however, with different reaction times (150, 100, 200, 200, 300 and 150 s, respectively). In all the cases, these peaks are broader than the reference TiC.
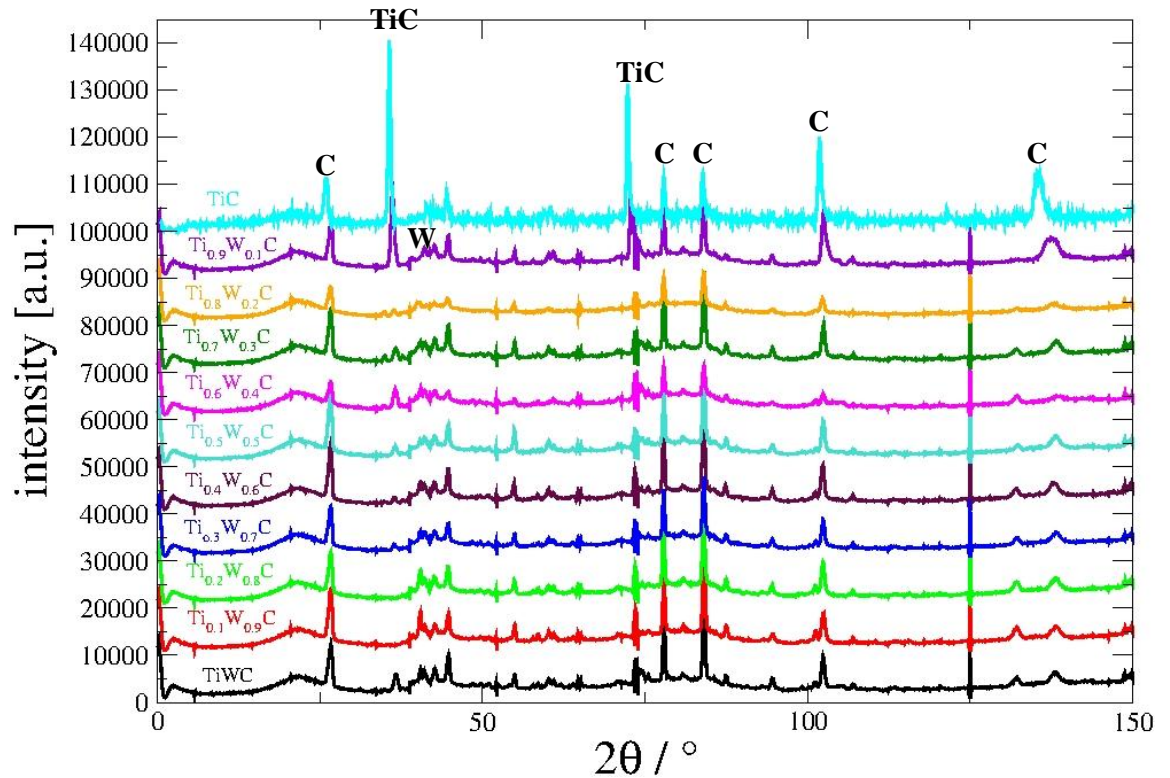
Figure 4.24 Diffractograms for each of the mixture in the $Ti_{(1-x)}W_xC_y$ system (x=0.1-0.9 $\Delta x = 0.1$ and y=1). Starting from the bottom, in black, TiWC (1:1:1 ratio). Going upwards, $Ti_{0.1}W_{0.9}C_1$ (in red), $Ti_{0.2}W_{0.8}C_1$ (in green), $Ti_{0.3}W_{0.7}C_1$ (in blue), $Ti_{0.4}W_{0.6}C_1$ (in maroon), $Ti_{0.5}W_{0.5}C_1$ (in turquoise), $Ti_{0.6}W_{0.4}C_1$ (in pink), $Ti_{0.7}W_{0.3}C_1$ (in dark green), $Ti_{0.8}W_{0.2}C_1$ (in orange), $Ti_{0.9}W_{0.1}C_1$ (in violet). Cyan line belongs to the MW-processed TiC (as described in Chapter 4, *sample 4*).

4.4.2.3 Ti-WO$_2$-C system

Fig. 4.25 shows the product of MW irradiation in the Ti-WO$_2$-C case. Again in the Ti-WO$_2$-C case, the characteristic peaks belonging to the formation of the carbide structure can be observed in samples having a higher concentration of Ti, namely Ti$_{0.9}$(WO$_2$)$_{0.1}$C$_1$, Ti$_{0.8}$(WO$_2$)$_{0.2}$C$_1$, Ti$_{0.7}$(WO$_2$)$_{0.3}$C$_1$, Ti$_{0.6}$(WO$_2$)$_{0.4}$C$_1$ shifted, in this case, to lower 2θ angles of 26 ° and 51 °2θ.
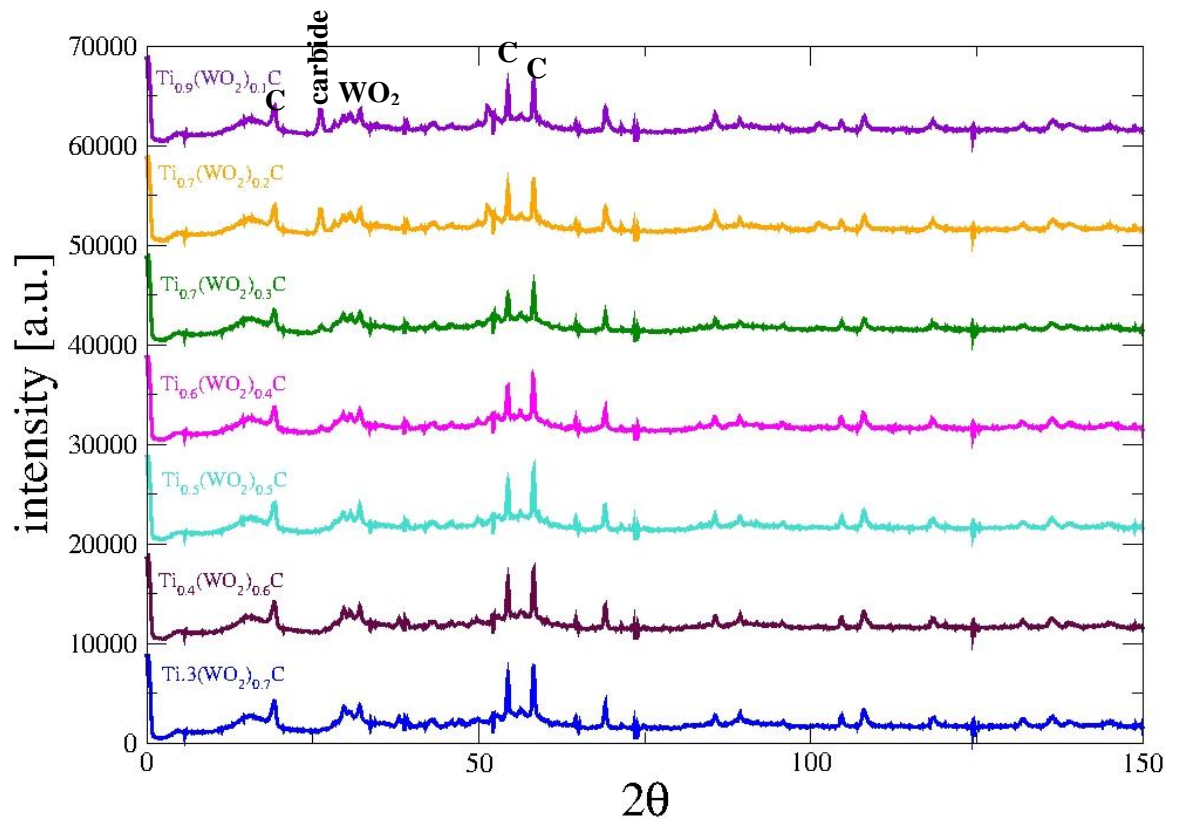
Figure 4.25. Ti$_{(1-x)}$(WO$_2$)$_x$C$_y$ with (x=0.3-0.9 Δx = 0.1) and (y=1). From the bottom, Ti$_{0.3}$(WO$_2$)$_{0.7}$C$_1$ (in blue), Ti$_{0.4}$(WO$_2$)$_{0.6}$C$_1$ (in maroon), Ti$_{0.5}$(WO$_2$)$_{0.5}$C$_1$ (in turquoise), Ti$_{0.6}$(WO$_2$)$_{0.4}$C$_1$ (in pink), Ti$_{0.7}$(WO$_2$)$_{0.3}$C$_1$ (in dark green), Ti$_{0.8}$(WO$_2$)$_{0.2}$C$_1$ (in orange), Ti$_{0.9}$(WO$_2$)$_{0.1}$C$_1$ (in violet).

4.4.2.4 Ti–Ta$_2$O$_5$-C system

More complex than the other systems presented above is the Ti-Ta$_2$O$_5$-C case, which did not respond to the presence of the MW electromagnetic field. In the four considered stoichiometric mixtures, in fact, no evidence of structural changes are visible either the modified TiC-like phases − formed in the above cases − are formed. This could be due to different issues which require further investigation, from both an instrumental and a chemical point of view. For example, it would be interesting repeating the same mixtures, in order to understand if the position of the sample in the reactor can be optimised and/or considering other stoichiometric ratios which could give a better and a faster response to the MW field.

Fig. 4.26 shows the product of reaction for each stoichiometric ratios studied.
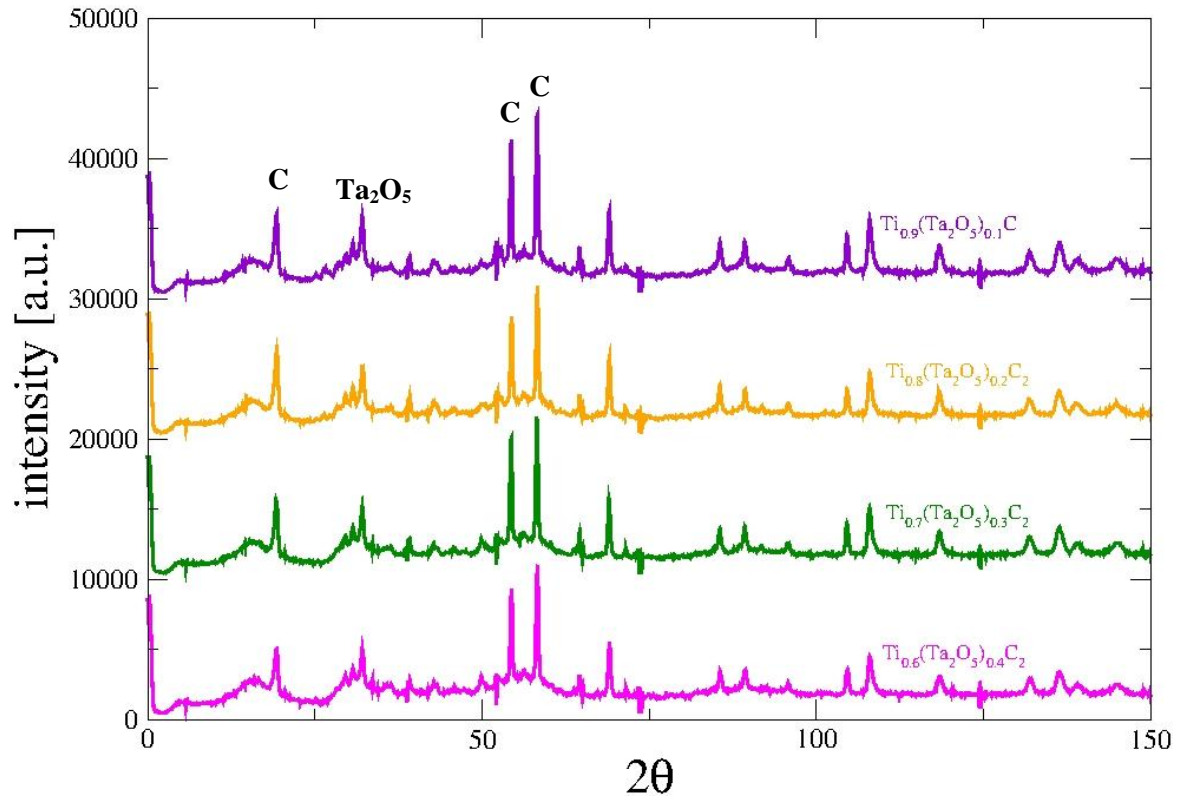
Figure 4.26. Diffractograms for $Ti_{(1-x)}(Ta_2O_5)_xC_y$ system (x=0.6-0.9 Δx = 0.1 and y=2). From the bottom, $Ti_{0.9}(Ta_2O_5)_{0.1}C_2$ (in pink), $Ti_{0.8}(Ta_2O_5)_{0.2}C_2$ (in green), $Ti_{0.7}(Ta_2O_5)_{0.3}C_2$ (in blue), $Ti_{0.6}(Ta_2O_5)_{0.4}C_1$ (in yellow), $Ti_{0.5}(Ta_2O_5)_{0.5}C_2$ (in turquoise), $Ti_{0.4}(Ta_2O_5)_{0.6}C_2$ (in pink), and $Ti_{0.3}(Ta_2O_5)_{0.7}C_2$ (in dark green).

4.4.3 Discussion and Conclusion

For all the systems described, except in the case of Ta_2O_5-TiC, it is observed that a higher concentration of Ti in the mixture lead to the TiC formation in a time range relatively low (around 2-3 minutes, on average). When the content of Ti in the mixture is decreased, no response to the MW field is observed.

This could be possible due to the fact that the metal – or also the oxide – addition in the TiC-based mixture mainly played a role of a catalyst for the reaction, thus making possible the TiC formation [20].

However, further physical-chemical investigations and characterisations of all the systems are required, in order to understand:

1) if the MW set-up plays a role in the systems formation and it is, therefore, possible to implement the instrumentation for processing systems prepared with a low content of Ti.

2) if these compounds could be classified as new cermets in terms of their observed properties;

3) if it is possible to implement the methodology for the Ta_2O_5-TiC system.

References

1. Lee, D.W., S. Alexandrovskii, and B.K. Kim, *Mg-thermal reduction of $TiCl_4+C_xCl_4$ solution for producing ultrafine titanium carbide.* Materials Chemistry and Physics, 2004. **88**(1): p. 23-26.
2. Zhang, H., et al., *Preparation of titanium carbide powders by sol-gel and microwave carbothermal reduction methods at low temperatures.* . Journal of Sol-Gel Science and Technology, 2008. **46**: p. 217-222.
3. Mohapatra, S., D.K. Mishra, and S.K. Singh, *Microscopic and Spectroscopic Analysis of TiC Powder Synthesized by Thermal Plasma Technique.* Powder Technology, 2013. **237**: p. 41-45.
4. Winkler, B., et al., *In situ observation in the formation of TiC from the elements by neutron diffraction.* Journal of Alloys and Compounds, 2007. **441**: p. 374-380.
5. Ahmad, I., R. Dalton, and D. Clark, *Unique Application of Microwave Energy to the Processing of Ceramic Materials.* Journal of Microwave Power and Electromagnetic Energy, 1991. **26**(3): p. 128-138.
6. Hassine, N.A., J.G.P. Binner, and T.E. Cross, *Synthesis of Refractory Metal Carbide Powders via Microwave Carbothermal Reduction.* International Journal of Refractory Metals & Hard Material, 1995. **13**: p. 353-358.

7. Menéndez, J.A., et al., *Microwave heating processes involving carbon materials.* Fuel Processing Technology, 2010. **91**: p. 1-8.

8. Rao, K.J., et al., *Synthesis of Inorganic Solids Using Microwaves.* Chemical Materials, 1999. **11**: p. 882-895.

9. Ohlsson, T. and P.O. Risman, *Temperature distribution of microwave heating - spheres and cylinders.* Journal of Microwave Power and Electromagnetic Energy, 1978. **13**(4): p. 303-309.

10. Wood, R.M., *The lattice constants of high purity alpha titanium.* Proceedings of the Physical Society, 1962. **80**: p. 783-786.

11. Hull, A.W., *Structure of graphite.* Physical Review, 1917. **10**: p. 661-696.

12. Burgers, W.G. and F.M. Jacobs, *Crystal structure of beta-titanium.* Zeitschrift für Kristallographie, Kristallgeometrie, Kristallphysik, Kristallchemie, 1936. **94**: p. 299-300.

13. Becker, K. and F. Ebert, *Die Kristallstruktur einiger binarer Carbide und Nitride.* Zeitschrift für Physik A Hadrons and Nuclei, 1925. **31**(1): p. 268-272.

14. Wang, J., et al., *Evidence for the Microwave Effect During Hybrid Sintering.* Journal of the American Ceramic Society, 2006. **89**(6): p. 1977-1984.

15. Harrison, A., et al., *In situ neutron diffraction studies of single crystals and powders during microwave irradiation.* Faraday discussions, 2002. **122**: p. 363-379.

16. Nihira, T. and T. Iwata, *Temperature Dependance of Lattice Vibrations and Analysis of the Specific Heat of Graphite.* Physical Review B, 2003. **68**: p. 134305-16.

17. Lohse, B.H., A. Calka, and D. Wexler, *Raman spectroscopy as a tool to study TiC formation during controlled ball milling.* Journal of Applied Physics, 2005. **97**: p. 114912-7.

18. Klein, M.V., J.A. Holy, and W.S. Williams, *Raman scattering induced by carbon vacancies in TiCx.* Physical Review B, 1978. **17**(4): p. 1546-1556.

19. Choi, Y., J.K. Lee, and M.E. Mullins, *Densification process of TiCx–Ni composites formed by self-propagating high-temperature synthesis reaction.* Journal of Materials Science, 1997. **32**(7): p. 1717-1724.

20. Fan, Q., H. Chai, and Z. Jin, *Role of iron addition in the combustion synthesis of TiC–Fe cermet.* Journal of Materials Science, 1997. **32**(16): p. 4319-4323.

21. Dunmead, S.D., et al., *Kinetics of Combustion Synthesis in the Ti-C and Ti-C-Ni Systems.* Journal of the American Ceramic Society, 1989. **72**(12): p. 2318-2324.

22. LaSalvia, J.C. and M.A. Meyers, *Combustion synthesis in the Ti-C-Ni-Mo system: Part II. Analysis.* Metallurgical and Materials Transactions A, 1995. **26**(11): p. 3011-3019.

23.   Brinkman, H.J., et al., *Production of Al–Ti–C grain refiner alloys by reactive synthesis of elemental powders: Part I. Reactive synthesis and characterization of alloys.* Journal of Materials Research, 2000. **15**(12): p. 2620-2627.

24.   Bandyopadhyay, S., H. Dutta, and S.K. Pradhan, *XRD and HRTEM characterization of mechanosynthesized $Ti_{0.9}W_{0.1}C$ cermet.* Journal of Alloys and Compounds, 2013. **581**(0): p. 710-716.

Chapter 5

Conclusions and Future Studies.

The work described in this thesis focuses on the MW synthesis of a ceramic material, TiC. In particular, the development of a general experimental procedure to afford the desired material and the study of its reaction pathway by means of *in situ* neutron diffraction are the major goals achieved. It has been demonstrated, in fact, that it is possible to produce TiC – traditionally synthesised *via* time demanding processes (24-48h) and high temperatures (1900-2300 K) – in second timescale, in a single mode MW reactor.

The final experimental procedure consisted of a 10 mm quartz tube (sealed at one end), containing the sample pellet (8 mm diameter, 1 g, 1 cm thickness) imbedded in graphite powder (acting as a susceptor), in the single mode cavity. The susceptor was required after initial investigation revealed no heating of the metal and carbon reaction mixture. Graphite, capable of absorbing the MW radiation and raising the reaction temperature, was used to help initiate carbide formation. However, careful use of the susceptor was required; too much would not allow sufficient MW energy to penetrate to the sample and too little would not provide adequate heat to raise the initial reaction temperature. The reaction was performed at ambient pressure.

The applied microwave power and the design of the set-up were also very important parameters which lead to the success of the reaction.

In the case of the Sairem cavity (described in Chapter 3) different geometries were tested prior the final (and working) configuration.

This single mode MW system is now available for users and fully operational on D20, at ILL. Further, it has been designed in such a way that it can easily fit the D20 beam line vessels, thus making possible reactions under vacuum, if needed.

TiC was also successfully obtained in a DMO, in 10 minutes, in air. However, as DMOs do not permit the control on several parameters (tuning of MW power, position of the sample in the cavity, possibility of *in situ* reactions), single mode MW cavity remains the best choice, despite of its higher costs and design difficulties.

It has been also demonstrated that this SMC-MW reactor is capable of processing different systems of higher complexity, such as ternary titanium-containing carbides ($Ti_xTa_{(1-x)}C$, $Ti_xW_{(1-x)}C$, $Ti_x(WO_2)_{(1-x)}C$, and $Ti_x(Ta_2O_5)_{(1-x)}C$). Preliminary results demonstrated that a higher amount of Ti in the mixture can lead to the formation of TiC in a relatively short time (2-3 minutes).

In conclusion, much of the work published in this thesis adds knowledge to MW apparatus design for solid state materials processes.

The contributions can be defined as follows:

- The development of a reproducible process for the successful MW synthesis of transition metal carbides in unprecedented timescales.

- Design and optimisation of a MW set-up capable of performing *in situ* reactions, thus giving insight in fast MW reactions, for the first time.

Future work could be focused on how incident power, reactor design, position of the sample in the cavity, and/or use of water as binder[17] can influence the process. Further, it would interesting to understand how these parameters might enhance the physical-chemical properties of products.

---

[17] In a precedent PhD project, it has been seen that an important factor in MW-promoted reactions is the use of water as binder – used in the pellet making process – which is believed to minimise the intergrain void space between particles and to act as a polar liquid MW susceptor (Carassiti L., *Synthesis of silicon carbide ceramics by novel microwave methods*, PhD thesis, University of Glasgow, 2011).